Characterisation of nanomaterials by X-ray diffraction profile analysis using the regularisation technique

Dissertation
zur Erlangung des Grades des Doktors der Naturwissenschaften
der Naturwissenschaftlich-Technischen Fakultät III
der Universität des Saarlandes
von

MSc in Radio-physics
Vladyslav Piskarov

Saarbrücken 2007

Abstract

For the deconvolution of the instrumental function in X-Ray diffraction profile analysis the implementation of an eigen function method with different regularisation techniques is investigated and a simple regularisation algorithm is proposed. A simulation of an instrumental-broadened profile superimposed with random noise and background signals is used to investigate the reliability and efficiency of the proposed deconvolution technique. For the simulation an experimentally defined instrument function based on an accurate mathematical model for Cu emission profile and the geometry of the diffractometer is used. The parameters for this instrumental function are obtained by least squares fitting of experimental data resulting from standard reference materials. The proposed method is successfully applied to the experimental X-ray diffraction data for nanostructured CeO_2, gold and gold alloys. Compared to established algorithms, it is faster and more reliable in terms of stability, especially in the case of large experimental noise.

Kurze Zusammenfassung

Zum Entfalten der instrumentellen Funktion in der Röntgenbeugungsprofil-Analyse wurde eine Eigenfunktion-Methode mit verschiedenen Regularisierungstechniken untersucht und ein einfacher Regularisierungsalgorithmus vorgeschlagen. Die Zuverlässigkeit und Effizienz der vorgeschlagenen Entfaltungsmethode wurde anhand der Simulation eines instrumentell verbreiterten Profils, das mit Zufallsrauschen und Hintergrundsignalen überlagert ist, untersucht. Für die Simulation wurde eine experimentell definierte Instrumentfunktion verwendet, die auf einem exakten mathematischen Modell für das Cu-Emissionsprofil und auf der Geometrie des Diffraktometers basiert. Die Parameter für diese instrumentelle Funktion wurden durch numerische Anpassung experimenteller Daten von Standardreferenzmaterialien mit der Methode der kleinsten Fehlersquadrate erhalten. Die vorgeschlagene Methode wurde erfolgreich auf experimentelle Röntgenbeugungsdaten von nanostrukturierten CeO_2, Gold und Goldlegierungen angewandt. Verglichen mit etablierten Algorithmen ist die Methode schneller und stabiler, besonders im Fall von starkem experimentellen Rauschen.

Summary

An experimental X-ray diffraction line profile is determined by sample broadening and instrumental aberration. This can be represented as the convolution of a physical line profile and an instrumental function. The approximation of the instrumental function influences the accuracy of the retrieved information on size and strain. The parameters of the commonly used empirical model for an instrumental function approximation based on split Voigt or Pearson VII functions can considerably vary depending on the type of the standard samples and the measurement conditions due to the lack of physical interpretation. Therefore, a new model for the instrument function based on an accurate mathematical model for Cu emission profile and the geometry of the diffractometer is proposed.

The proposed model is proved using different standard samples. It is shown that differences in the parameters for the instrumental function obtained by LaB_6 and Al_2O_3 do not exceed 10%. The deliberate changes made to the diffractometer set-up lead to changes of the corresponding values of defined parameters.

An important problem of powder diffractometry is the restoration of a physical line profile from experimental data by extracting it as a solution of a convolution integral equation. It is shown that commonly used Fourier based deconvolution methods cause a dramatical increase of noise in the deconvoluted profile and even starting from low instrumental noise this technique is absolutely not stable. The implementation of an eigen function method with a simple regularisation algorithm is proposed for the deconvolution of the instrumental function. The codes for the proposed deconvolution method are written in MATLAB.

A simulation of an instrumental-broadened profile superimposed with random noise and background signals is used to investigate the reliability and efficiency of the proposed algorithm. For the simulation an experimentally defined instrumental function based on the proposed above model is used. The parameters for this instrumental function are obtained by least squares fitting of experimental data sets resulting from the reference materials LaB_6 and Al_2O_3. The proposed regularisation

technique shows high stability, especially in the case of large non negligible experimental noise. Furthermore, the overestimation of the noise level leads only to a slight worsening of the restoration results. An additional advantage of the proposed regularisation technique is its independence on the concrete analytical form of the approximation of the instrumental function.

A diffraction pattern contains information about the strain through changes in the shapes of the Bragg peaks and also through peak shifts. Crystallite size effects also influence the peak shape. Therefore, it is possible, to extract descriptions of crystallite size and strain from the peak broadening of a diffraction pattern. The use of the Voigt function for size and strain analysis by fitting of diffraction data is popular because it favours the deconvolution procedures as well as the separation of size and strain effects in the analysis. This approach gives adequate information about size and strain values, however, it has three deficiencies: it uses the physically unjustified Lorentzian-size and Gaussian-strain assumptions, it does not take into account the size distribution information and it cannot deal with 'super-Lorentzian' profiles. These deficiencies are confirmed in this study by fitting simulated physically-derived size profiles with a Voigt function based model.

The convolution model, which uses a physically reasonable size profile and a Gaussian-strain profile for the line profile fitting and accommodates the size distribution and strain parameters has been successfully developed, validated and, finally, applied to the experimental diffraction data for CeO_2 and nanostructured gold, gold-silver and gold-palladium alloys. It is shown that the convolution model gives access to the size distribution and the strain information from the diffraction data. By this method, consistent crystallite sizes are obtained and a good agreement between strain values is achieved. The 'convolution' size distribution results satisfactorily agree with those obtained from transmission electron microscopy (TEM). The TEM-derived grain sizes, however, are larger than the 'convolution' crystallite sizes indicating that apparent grains contain clusters of crystallites or stacking faults in the case of fcc metals.

Zusammenfassung

Ein Röntgenbeugungslinienprofil wird durch probeninduzierte Verbreiterung und instrumentelle Verbreitung bestimmt. Dies kann als Faltung eines physikalischen Linienprofils und einer instrumentellen Funktion dargestellt werden. Die Näherung für die instrumentelle Funktion beeinflusst die Genauigkeit der erhaltenen Informationen über die Größe und die Verspannung. Die Parameter des konventionell verwendeten empirischen Modells für die instrumentelle Funktion, das auf Split- Voigt- oder Pearson VII-Funktionen basiert, können in Abhängigkeit von der Art der Standardproben und den Messbedingungen beträchtlich variieren, was auf die mangelnde physikalische Interpretation zurückzuführen ist. Deshalb wird ein neues Modell für die Instrumentfunktion vorgeschlagen, das auf einem exakten mathematischen Modell für das Cu-Emissionsprofil und der Geometrie des Diffraktometers basiert.

Das vorgeschlagene Modell wird durch die Verwendung verschiedener Standardproben überprüft. Es wird gezeigt, dass die Unterschiede in den Parametern für die instrumentelle Funktion, die für LaB_6 und Al_2O_3 erhalten wurden, 10% nicht überschreiten. Bewusst hegeführte Fehljustierungen des Diffraktometers führen zu Änderungen der entsprechenden Parameter.

Ein wichtiges Problem der Pulverdiffraktometrie ist die Berechnung eines physikalischen Linienprofils aus experimentellen Daten, das aus der Lösung einer Faltungsintegralgleichung extrahiert wird. Es wird gezeigt, dass konventionell verwendete Fourier-basierte Faltungsmethoden einen dramatischen Anstieg des Rauschens im entfalteten Profil verursachen. Sogar bei geringem instrumentellen Rauschen ist diese Technik unzuverlässig. Für die Entfaltung der instrumentellen Funktion wird die Implementierung einer Eigenfunktionmethode mit einem einfachem Regulierungsalgorithmus vorgeschlagen. Die Codes für die vorgeschlagene Entfaltungsmethode sind in MATLAB programmiert.

Die Zuverlässigkeit und Effizienz der vorgeschlagenen Entfaltungstechnik wurde mit der Simulation eines instrumentell verbreiterten Profils, das mit Zufallsrauschen und Hintergrundsignalen überlagert ist, untersucht. Für die Simulation wurde eine experimentell definierte instrumentelle Funktion, die auf obigem Modell basiert, verwendet. Die Parameter für diese instrumentelle Funktion wurden durch numerische Anpassung experimenteller Daten von Standardreferenzmaterialien mit der Methode

der kleinsten Fehlerquadrate erhalten. Die vorgeschlagene Regulierungstechnik zeigt eine hohe Stabilität, besonders im Falle von starkem, nicht vernachlässigbaren experimentellen Rauschen. Außerdem führt die Überschätzung des Rauschniveaus nur zu einer geringen Verschlechterung der extrahieren physikalischen Linienprofile. Ein zusätzlicher Vorteil der vorgeschlagenen Regulationstechnik ist ihre Unabhängigkeit von der konkreten analytischen Form der Annäherung der instrumentellen Funktion.

Ein Beugungsmuster enthält Informationen über Verspannungen in den Änderungen von Bragg-Peak-Formen und auch in den Peakverschiebungen. Kristallitgrößeneffekte beeinflussen ebenfalls die Peakform. Deshalb ist es möglich, aus der Peakverbreiterung eines Diffraktogramms simultan Informationen über die Kristallitgröße und die Verspannung zu erhalten. Die Anwendung der Voigt-Funktion für die Analyse von Größen und Verspannungen durch Anpassung von Beugungsdaten ist populär, weil es die Entfaltungsmethode genauso unterstützt wie die Trennung von Größen- und Verspannungseffekten in der Analyse. Diese Annäherungsmethode gibt adäquate Informationen über Größen- und Verspannungswerte, jedoch weist sie drei Mängel auf: Sie verwendet die physikalisch unbegründeten Lorentzsche Größen- und Gaußsche Verspannungsannäherungen, sie berücksichtigt nicht die Größenverteilung und ist für das Super-Lorentz-Profil ungeeignet. Diese Mängel wurden in dieser Studie bestätigt, indem simulierte Größenprofile, die von physikalischen Daten abgeleitet wurden, mit einem auf der Voigt-Funktion basierenden Modell angepasst wurden.

Das Faltungsmodell, das ein physikalisch sinnvolles Größenprofil und ein Gaußsches Verspannungsprofil für die Anpassung des Linienprofils benutzt und die modale Größe, Größenverteilung und Verspannungsparameter bestimmt, wurde erfolgreich entwickelt, validiert und schließlich auf die experimentellen Beugungsdaten von nanostrukturiertem CeO_2 und Gold, Gold-Silber- und Gold-Palladiumlegierungen angewandt. Es wurde gezeigt, dass das Faltungsmodell Zugang zu der Größenverteilung und der Verspannungsinformation aus Beugungsdaten erlaubt. Durch diese Methode werden konsistente Kristallitgrößen erhalten und eine gute Übereinstimmung zwischen Verspannungswerten erreicht. Die 'Faltungs-' Größenverteilungen stimmen hinreichend mit denen überein, die aus der Transmissionselektronenmikroskopie (TEM) erhalten wurden. Die aus der TEM abgeleiteten Korngrößen sind jedoch etwas größer als die 'Faltungs-' Kristallitgrößen: offensichtlich bestehen Körner aus mehrere Kristalliten konstituierender Cluster oder enthalten Stapelfehler im Fall von kubisch-flächenzentrierten Metallen.

Table of Contents

Chapter 1

Introduction

1.1 Diffraction line profile analysis

Crystallite (or grain) size and strain within a polycrystalline material may have a profound influence on its performance, e.g. on the fracture toughness, wear resistance and thermal shock behaviour. A diffraction pattern of the material conveys information about the strain through changes in the shapes of the Bragg peaks and also through peak shifts. Crystallite size effects may also distort the line shapes. Therefore, it is possible to extract descriptions of the size and strain effects from the peak broadening of a diffraction pattern.

Strategies applied to model size and strain effects from Bragg peak shape distortions mainly involve fitting mathematical functions to the measured line shapes, and then extracting strain and size descriptions according to theoretical models for which the mathematical functions are assumed to be physically correct for the material under study. This approach, however, may be inappropriate as the analytical functions used may not physically be acceptable and most of models mainly do not take into account the size distribution.

The broad concept underpinning this study is that the changes in Bragg peak shapes should be modelled with physically-appropriate functions which correctly reflect the microstructural environment under which size and strain develop.

A theory of size broadening was initially given by Scherrer [see Warren, 1969] shortly after the discovery of X-ray diffraction. Stokes and Wilson [1944] devised a method to study X-ray line broadening due to size and strain using Fourier transform

theory. In subsequent developments [e.g. Langford, 1978], line profile analysis was conducted by fitting mathematical functions to the diffraction data followed by the extraction of size and strain descriptions from the fitted functions.

Most research on line broadening analysis theory has focussed on metallic materials [Warren, 1969; Klug and Alexander, 1974; de Keijser et al., 1982; Langford et al., 1986]. Some work has been done more recently on ceramic powders [Langford et al., 1986; Auffredic et al., 1995; Balzar, 1999; Louer, 1999; Audebrand et al., 2000a,b; Louer et al., 2002] and polymeric materials [Somashekar and Somashekarappa, 1997].

Assessments of size and/or strain information from the analysis of single Bragg peaks is problematic because the shape of the peaks may provide reasonable results for either strain or size modelling, but proves to be more challenging where both effects are present. In the past, a single function was mainly used to separately represent the size and strain components, e.g. Gaussian, Lorentzian (or Cauchy), pseudo-Voigt and Voigt functions. However, both, theory and experiment showed that in many cases such approaches may not be appropriate. This is presumably due to the lack of physical basis for the use of particular functions for the material under study.

Klug and Alexander [1974] reviewed three classical methods which can be used for simultaneously extracting crystallite size and strain contributions from x-ray diffraction line broadening data:

1. Fourier transform method

2. Integral breadth method

3. Line profile variance method

In applying these methods for separating crystallite size and strain contributions, deconvolution of 'pure' specimen broadening must be carried out since an observed peak profile is a convolution of instrumental and pure specimen profiles (Fig. 1.1).

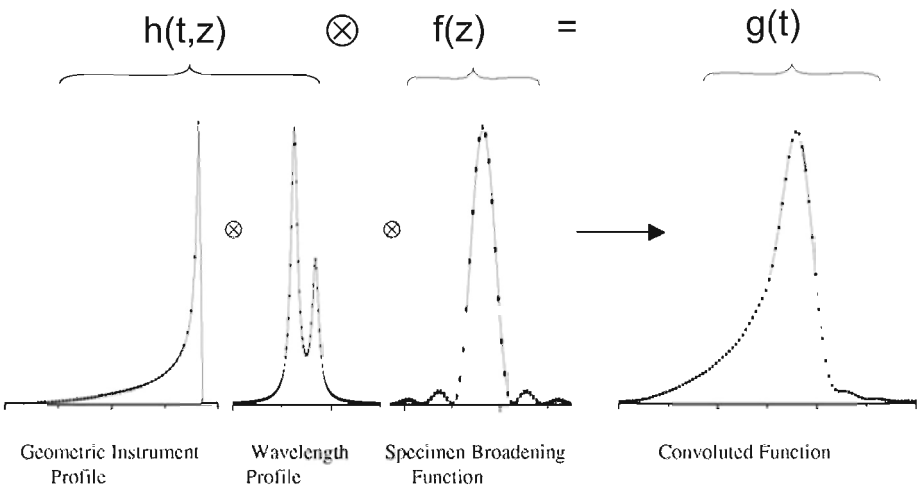

Figure 1.1: An observed diffraction peak $g(t)$ is a convolution between 'pure' specimen $f(z)$ and instrumental function $h(t-z)$.

The mathematical expression of the convolution is as follows:

$$g(t) = \int_{-\infty}^{\infty} h(t-z) * f(z) dz \tag{1.1}$$

or,

$$g = h \otimes f \tag{1.2}$$

where $g(x)$ is the observed profile, $h(t-z)$ is the instrumental profile, $f(z)$ is specimen profile. Here, f represents the combined strain and size contributions to the profile. A standard specimen, showing minimal strain- and size-related broadening, is required for measurement of the peak profiles, h, which describe aberrations associated with instrument optics and wavelength spread.

Procedures for deconvoluting of 'pure' specimen profiles f from observed profiles g require an approximation of the measured profiles with an analytical function. A split Pearson VII function has been used to model h for x-ray diffractometry [Howard and Snyder, 1989; Balzar, 1992]. Use of the pseudo-Voigt function has also been reported in x-ray and synchrotron radiation diffractometry [Thompson et al., 1987; Enzo et al., 1988].

The observed profile defined by the standard reference material can pretty well be fitted using a model based on split Pearson VII or Voigt functions. Otherwise, due to a big number of refinable parameters in this models and the interdependence between their parameters defined by different standard samples can considerably vary. Therefore, a model for the instrumental function which is based on physical properties of diffractometer is more preferable. In this work the development of such a model will be proposed.

A variety of methods have been proposed for the elimination of instrumental broadening [Rachinger, 1948; Stokes, 1948; Keating, 1959; Gangulee, 1970; Ladell et al., 1975]. However, none of these methods can be used to eliminate the instrumental aberrations from the entire observed diffraction pattern in a one-step operation. It is impossible to deconvolute all of the instrumental effects from an entire diffraction pattern by a standard Fourier method, because the profile of the instrumental function for powder diffractometry varies in a complex manner in dependence on the diffraction angle 2θ.

Ida and Toraya [2002] have proposed a Fourier based approach to deconvolute the instrumental aberration functions from experimental powder X-ray data. This method is based on the combination of scale transformation, interpolation of data and fast Fourier transformation. It is well-known, that the Fourier based deconvolution always exaggerates the noise in the source data. Therefore, for successfull application of Fourier based methods the real experimental data have to be first smoothed with some empirical functions (like split Pearson, split Voigt and etc.). However, this smoothing procedure will suppress or at least distort information about peak shape where the information about specimen properties like size and strain distributions is hidden.

Therefore development of new fast and in terms of stability more reliable deconvolution technique is required, especially in the case of large non neglectable experimental noise.

In these classical methods, microstructural information was directly deduced from experimental data for distorted metals [e.g. Guinier, 1963]. Consequently, the theory was developed based on the dislocation theory in metals [Warren and Averbach, 1950].

The recent intensification of interest in strain-size analysis is attributed to the dramatic improvement in computing power which has allowed profile fitting to be performed more effectively. However, these advances have been limited by the use of profile fitting functions which may not be physically appropriate for particular classes of materials. Single-line and multi-line methods can be used for the extraction of strain-size information by diffraction profile fitting. Recently, a pattern decomposition method has been accomplished, for the same purpose, by fitting analytical functions to whole diffraction patterns [Langford, 1992]. This achievement was followed by the introduction of the whole-powder pattern-fitting (WPPF) approach [Toraya, 1986; Scardi, 1999; Scardi and Leoni, 2001].

There are, in general, two approaches which are commonly used for obtaining crystallite strain and size values from diffraction line-broadening: the application of the integral breadth method and the Warren-Averbach Fourier transform method. Reviews of these methods have been given, for example, by Delhez et al. [1982]. The first approach involves diffraction data fitting with the symmetric Voigt (a convolution of Gaussian and Lorentzian profile functions) [Langford, 1978; de Keijser et al., 1982], pseudo-Voigt [Wertheim et al., 1974] or Pearson VII [Hall et al., 1977] functions which do not necessarily have a physical basis in terms of microstructural character. Also, these functions do not model the crystallite size distribution parameter [Klug and Alexander, 1974; Langford et al., 2000; Popa and Balzar, 2002]. The second approach

is more physically acceptable; however, it has two substantial limitations in that the broadening should be sufficiently large [Delhez and de Keijser E. J. Mittemeijer, 1980] and improper determination of the background introduces a severe 'hook' effect in the Fourier reciprocal space [Warren, 1969]. Moreover, this Fourier technique cannot readily deal with overlapping peaks and is very sensitive to experimental noise. As a result, this method tends to be restricted to materials with high crystallographic symmetry, giving rise to only few diffration peaks. Therefore, the line profile method performed in angular/crystal space is preferred, provided that the model for each effect is known and the overall function can be developed for the complete angular and Q-range.

Multi-line profile fitting methods should be inherently superior to single-line procedures for strain-size analysis as the angular dependence of the separate strain and size contributions to the specimen function f are markedly different. Two well-known multi-line methods which have widely been used in line broadening analysis are Warren-Averbach [1950; 1952] and Williamson-Hall[1953]. In the Warren-Averbach method, Fourier transforms are performed using diffraction data to give information about crystallite size and strain. However, again, the use of Fourier transform may cause some numerical problems in the analysis.

In the Williamson-Hall method [Williamson and Hall, 1953], the peak broadening β is extracted from

$$\beta cos\theta = \frac{\lambda}{D} + 4\epsilon sin\theta \tag{1.3}$$

where D is the apparent crystallite size, ϵ is the maximum (upper limit) microstrain and λ is the radiation wavelength. This method assumes that the Lorentzian function contributes to both, size and strain effects. This assumption may not be a good approximation for strain broadening since a strain profile tends to be Gaussian, particularly for low-strain materials.

Further development of line profile fitting of diffraction data with the Voigt function [Langford, 1978] led to the use of this function in the so called 'average size-strain' method [Langford, 1992]. The Williamson-Hall plot was used only for qualitative inspection in describing if the specimen integral breadth is d^*-dependent, where d^* is the interplanar spacing in reciprocal units. A plot of $\left(\frac{\beta_f^*}{d^*}\right)^2$ *vs.* $\frac{\beta_f^*}{(d^*)^2}$ was then examined to give the mean strain value from the intercept of the plot on the $\left(\frac{\beta_f^*}{d^*}\right)^2$ axis and the mean apparent size from its slope. It was assumed that strain contributes only to the Gaussian profile and size to the Lorentzian profile. Since the pseudo-Voigt and Pearson VII functions can approximate the Voigt function [de Keijser et al., 1983], the use of these functions for size and strain analysis is possible, however with some additional errors introduced from the approximation. It should be noted again that application of these functions in the analysis has no direct physical basis. Moreover, the crystallite size distribution is not taken into account in using the functions.

The extraction of microstructural information from powder diffraction data has greatly been enhanced by the discovery of the Rietveld method [Rietveld, 1967, 1969] which is an approach to fit a structural-based model to a whole powder pattern. Subsequently, it was shown that the method can also be used to extract information about crystallite size and strain [de Keijser et al., 1983; Delhez et al., 1993; Pratapa et al., 2002]. The procedure can be accomplished using the Voigt function. It should be emphasised that the application of this method with X-ray diffraction data may not be satisfactory since the assumed functions for the instrument and specimen effects may not be appropriate.

Further development in powder diffraction data analysis based on the whole powder pattern approach was achieved by developing models which do not need complete structural data [Toraya, 1986; Scardi, 1999; Scardi and Leoni, 2001]. Whole-pattern fitting based on Fourier coefficient calculations has also recently been introduced

[Ungar et al., 2001]. Whole Powder Pattern Fitting (WPPF) may be used at the initial stage of an ab initio structure determination as well as for extraction of microstructural features such as crystallite size and microstrain [Scardi, 1999]. It is of importance to note that the pattern fitting was performed by applying the analytical functions such as Pearson VII [Toraya, 1986] and pseudo-Voigt [Scardi, 1999; Scardi and Leoni, 2001]. The recent literature indicates a strong trend towards the use of whole-powder diffraction data for acquiring structural and microstructural information from materials.

Even though the results obtained by the approaches described above may be valid for some material types (notably metals), the mathematical assumptions may lead to incorrect results if the assumed size and dislocation models are inappropriate. In such cases, the information gained from the analysis may be unreliable or even meaningless, e.g. the negative values of size parameter calculated using the Williamson-Hall multi-line method for alumina whiskers data reported by Balasingh et al. [1991].

1.2 Research objectives

The principal objectives of this study are: the examination of existing Voigt based methods for strain-size evaluation; consideration whether Voigt-based models might be refined for application in modelling of size-strain characteristics; development of new physically-based modelling methods.

A new model has to be developed based on the theory given by Langford et al. [2000]; Popa and Balzar [2002]; Ida et al. [2003].

The codes for the proposed model are written in C++. The codes are compiled to produce executable software which can perform peak profile fitting in command line interface mode.

Model evaluation should be performed using X-ray diffraction (XRD)

The model for the instrumental function which is based on physical properties of diffractometer will be proposed and proofed by using standard reference materials like LaB_6, Al_2O_3 and SiO_2.

The development of a new fast and in terms of stability more reliable deconvolution technique will be presented, especially in the case of large non neglectable experimental noise.

The codes for the proposed deconvolution method are written in MATLAB.

Chapter 2

Analysis of the diffraction pattern

This chapter reviews the literature on crystallite size and strain evaluations from diffraction line broadening (the term 'line broadening' is used subsequently for simplification). First, the definitions of crystallite size and strain are considered with particular attention to the line broadening. A review of instrument contributions to the broadening is then presented to provide a description of correcting for instrument effects in size and strain analysis. The sources of the specimen-related line broadening are explored, followed by details of the methods for assessing size and strain, by means of the Fourier, whole-powder pattern-fitting and integral breadth methods. The Fourier method is not discussed in detail as the method is not of interest in the study.

Size broadening is due to the small size of a particular region which causes the radiation to be incoherently diffracted [Guinier, 1963]. In polycrystalline materials, a large number of grains with various relative positions and orientations causes variations in the phase differences between the wave scattered by one grain and waves scattered by others, which can take any values between 0 and 2π with equal probability. The total intensity scattered by all grains is the sum of individual intensities scattered by each grain; or, in other words, the grains diffract incoherently or independently. In terms of size and strain, therefore, diffraction peak broadening consists of a size broadening contribution which reflects the size of the grain (therefore called grain size) and a strain broadening component which represents the relative atomic displacements within the grain.

Berkum et al. [1999] argued that lattice defects which are parts of grains, called domains, can also be considered to diffract incoherently with each other. From this point of view, line broadening may consist of a size broadening of domains and a strain broadening from the same domains. The domain concept, however, does not have a clear technical basis since it cannot be confirmed using other characterisation techniques, while 'grain size' can be measured by microscopy.

The term 'crystallite size' is used by others [Louer, 1999; Langford et al., 2000] who have argued that it also represents grain size. The term 'crystallite size' is used in this thesis to define a finite size of region in a specimen where radiation is diffracted coherently (with respect to other regions).

Size distribution describes the dispersion of crystallite sizes in a material. It is now well known that size distribution influences diffraction peak shapes [Klug and Alexander, 1974; Langford et al., 2000]. Therefore, it is possible to extract a size distribution description from line broadening, provided that the appropriate model is used. Recently, there have been some efforts to acquire information about size distribution from line broadening by introducing an additional parameter into an analytical profile function such as the pseudo-Voigt function [Popa and Balzar, 2002].

From the classical theory of strain in deformed materials, it is assumed that elastic deformation will cause constant changes of lattice plane spacings from one grain to another [Cullity, 1978]. Such strained materials exhibit macroscopic uniform dimension changes from the original size. These changes, relative to the original dimensions, are called uniform macrostrains. If this kind of strain is observed on a microscopic scale (approximatly as large as a grain several microns in size), the material can be considered to exhibit a uniform microstrain. By contrast, it is known that plastic deformation will cause various changes of lattice plane spacings from one grain to another or one part to another. These lattice spacing changes, relative to the original,

are called non-uniform microstrains.

Macrostrain describes the line shift related information determined by the diffractometric residual stress method which is used routinely to characterise long-range, near-surface tensile and compressive strains [Noyan and Cohen, 1987]. This category of strain can occur, for example, when a material after anisotropic thermal expansion cools during processing. The cooling rate of the inner part is smaller than that of the outer part so that a compressive residual strain develops in the nearsurface of the material.

Microstrain refers to Bragg line shifts and shape distortions associated with grain-grain interactions such as those caused by differences in thermal expansion between grains in a multi-phase material. Uniform microstrain relates to changes in cell parameters caused by these grain-grain tensile or compressive effects, whereas non-uniform microstrain effects are associated with grain-grain shear effects which contribute to line broadening.

Therefore, the microstructural strain-size related items of information which can be extracted from the peak shapes of diffraction data are the non-uniform strain, crystallite size and crystallite size distribution.

The ideal peak shape for a diffraction line is a delta function. In reality, however, there are physical effects which may broaden the diffraction line. These effects can be classified into instrument and specimen broadening. This section describes possible sources of line broadening in detail. Definitions of peak width and peak-shape functions are compiled in Table 2.1.

There are two important measures in line profile analysis of powder diffraction, i.e. the peak position and the peak width (or broadening). The peak position is determined by [Klug and Alexander, 1974]

$$\langle 2\theta \rangle = \frac{\int 2\theta \cdot I(2\theta) d(2\theta)}{\int I(2\theta) d(2\theta)} \tag{2.1}$$

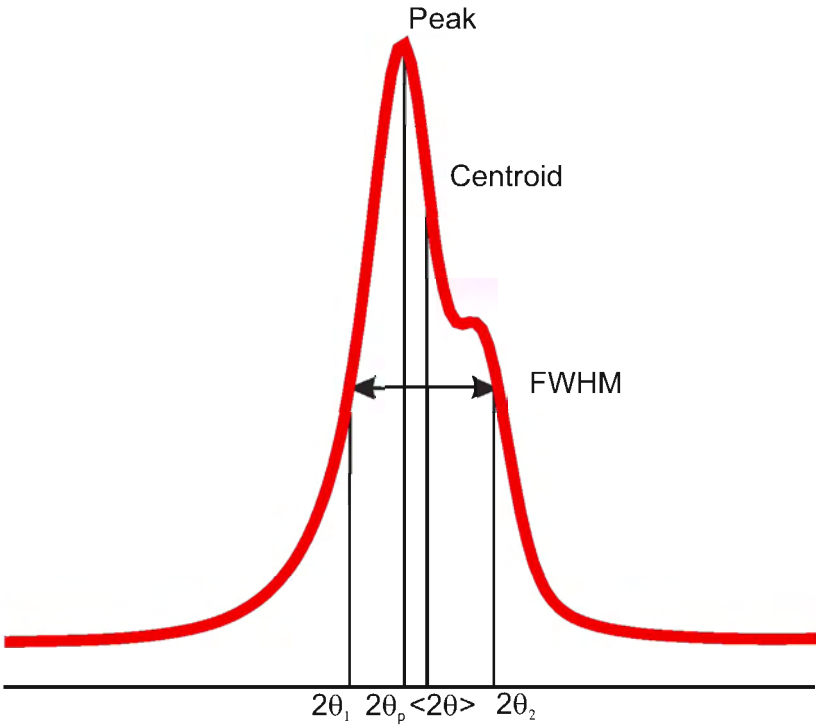

Figure 2.1: A diffraction line profile illustrating the definition of peak, centroid and full-width at half-maximum intensity (FWHM) [Klug and Alexander, 1974].

The peak width can be described by the following measures [Klug and Alexander, 1974]:

1. full-width at half-maximum (FWHM) - the overall width of the line profile at half-maximum intensity measured above the background (see Fig. 2.1).

$$FWHM = 2\theta_2 - 2\theta_1 \tag{2.2}$$

2. integral breadth (β) - the integrated intensity of the line profile above background divided by the peak height, I_p.

$$\beta = \frac{1}{I_P} \int I(2\theta) d(2\theta) \tag{2.3}$$

3. variance - squared standard deviation of the elements comprising the profile.

$$W = \langle (2\theta - \langle 2\theta \rangle)^2 \rangle = \frac{\int (2\theta - \langle 2\theta \rangle)^2 \cdot I(2\theta) d(2\theta)}{\int I(2\theta) d(2\theta)} \tag{2.4}$$

Table 2.1: List of basic analytical profile-shape functions (PSFs) cited in this study.

Profile-shape function (PSF)	Mathematical form
Gaussian [1]	$I_G(x) = I_0 e^{-4\ln 2 \frac{x^2}{w_G^2}}$
Lorentzian (Cauchy) [2]	$I_L(x) = \frac{I_0}{1 + 4\frac{x^2}{w_L^2}}$
Pearson VII [3]	$I_{PVII} = \frac{I_0}{1 + 4(2^{1/m} - 1)\frac{x^2}{w_{PVII}^2}}$
Voigt [4]	$I_V(x) = I_0 \frac{\beta}{\beta_L} Re\left[\text{erfi}\left(\frac{\pi^{1/2} x}{\beta_G} + ik\right)\right]$
Pseudo-Voigt	$I_{pV} = \varphi I_G(x) + (1 - \varphi) I_L(x)$

Subscripts $G, L, PVII, pV$ and V denote the Gaussian, Lorentzian, Pearson VII, pseudoVoigt and Voigt functions, respectively.

x	2θ position (in radian)
$I(0)$	peak intensity
w	full-width at half-maximum intensity (FWHM)
β	integral breadth (= area/maximum intensity)
m	Pearson VII index
φ	pseudo-Voigt mixing parameter
erfi	complex error function
Re	real part of a complex function

[1] $\beta_G = \frac{\pi w_G}{2}$

[2] $\beta_L = \sqrt{\frac{\pi}{\ln 2}} \frac{w_L}{2}$

[3] $\beta_{PVII} = \frac{\pi 2^{2(1-m)} \Gamma(2m-1)}{(2^{1/m} - 1)\left[\Gamma(m)\right]^2} \frac{w_{PVII}}{2}$ where Γ is the gamma function

[4] $\beta = \beta_G \exp(k^2)[1 - \text{erf}(k)]$ where erf is the error function or

[4] $\beta^2 \approx \beta_L \beta + \beta_G^2$

$$k = \frac{\beta_L}{\sqrt{\pi}\beta_G}$$

The Voigt shape factor φ is defined as

$$\varphi = \frac{w}{\beta}$$

$\phi_L = \frac{2}{\pi} = 0.6366$ and $\phi_G = 2\sqrt{\frac{\ln 2}{\pi}} = 0.9394$

Therefore,

$0.6366 \leq \phi_V \leq 0.9394$, where ϕ_v is the Voigt shape factor.

The Voigt peak shape factor can be approximated using

$$\phi \approx \frac{E(1 + Ak + Bk^2)}{1 + Ck + Dk^2)}$$

where $A = 0.9039645$, $B = 0.7699548$, $C = 1.364219$, $D = 1.136195$, $E = 2(\ln 2/\pi)^{1/2} = 0.9394372$. This approximation has a maximum difference from the exact value of 0.16% (at $k = 0.15$) [Langford, 1999].

2.1 Instrumental broadening

The instrument broadening contribution h (Eq. 1.1) in powder diffraction data originates from the non-ideal optical effects of the diffractometer and from the wavelength distribution of the radiation.

A diffraction profile measured from a structurally imperfect material (g profile) is considered as a convolution of the profile f due to crystallite imperfections (nonuniform microstrain and small crystallite size) and the h profile (Fig. 1.1). This relationship can be expressed as (Eq. 1.1). The h profile can be determined either mathematically [Wilson, 1963] or by measurement with a suitable standard material [Berkum et al., 1995] which is assumed to be free from specimen broadening effects.

The influence of instrument effects on line broadening was reviewed in considerable detail by Klug and Alexander [1974] who considered the effects of X-ray source, flat specimen surface, axial divergence, specimen transparency, receiving slits and instrument misalignment for a Bragg-Brentano diffractometer. The individual effects, which are analytically approximated, may be convoluted with each other. These effects have also numerically been modelled [Cheary and Coelho, 1992; Finger et al., 1994; Ida and Toraya, 2002]. An ab initio Monte Carlo approach has also been applied to determine the instrument function by taking into account all possible optical paths [Timmers et al., 1992]. Some of the instrument characteristics, however, cannot be determined directly with sufficient accuracy [Berkum et al., 1995]. Therefore, measuring h for correction of the instrument profile is more precise and reliable, provided that a suitable standard specimen is available. A standard specimen for instrument correction should meet the following criteria [Berkum et al., 1995; Leoni et al., 1998; Reefman, 1999]:

- does not exhibit measurable specimen broadening;

- (ideally) is developed from the same material as the specimen to be investigated;

- should not exhibit pronounced transparency effect;

- exhibits minimal errors from crystal statistics caused by surface roughness or large particles.

In cases where a standard material is developed from the same material under investigation, strain-size analysis gives the sample differences not the absolute values [Balzar, 1999; Reefman, 1999]. A specimen showing the least line width can be used as a reference and the relative microstructural information can be determined.

A standard reference material made from a material other than that under analysis can also be used. The primary advantage of using this strategy is that the profile is collected for a range of test materials provided there is no change in the instrument arrangement. Examples of such standards are BaF_2 as described by Louer and Langford [1988] and the NIST Standard Reference Material (SRM) 660a LaB_6 [Freiman and Trahey, 2000].

Procedures for convoluting h with a known or assumed f require an approximation of the measured profiles with an analytical function. The measured profiles are fitted with a selected profile function and the fit parameters are extracted. A variation of the parameters with 2θ can be obtained and then the profile for an arbitrary 2θ can be computed with the fit parameters. A split Pearson VII function has been used to model h for X-ray diffractometry [Howard and Snyder, 1989; Balzar, 1992]. Use of the pseudo-Voigt function has also been reported in X-ray and synchrotron radiation diffractometry [Thompson et al., 1987; Enzo et al., 1988].

2.1.1 Instrumental line profile

In this section the profile functions based on the Pearson VII function $P(2\theta)$ including peak asymmetry are described [Toraya, 1986]. A restriction that the function $P(2\theta)$ has a total area of unity gives the form

$$P(2\theta) = \begin{cases} \frac{Q}{W}\left[1 + \left(\frac{1+A}{A}\right)^2 \left(2^{1/R_L} - 1\right)\left(\frac{2\theta - T}{W}\right)^2\right]^{-R_L} & for \quad 2\theta \leq T \\ \frac{Q}{W}\left[1 + (1+A)^2 \left(2^{1/R_H} - 1\right)\left(\frac{2\theta - T}{W}\right)^2\right]^{-R_H} & for \quad 2\theta > T \end{cases} \tag{2.5}$$

$$Q = \frac{2(1+A)}{\sqrt{\pi}}\left[A\frac{\Gamma(R_L - \frac{1}{2})}{\sqrt{(2^{1/R_L} - 1)}\Gamma(R_L)} + \frac{\Gamma(R_H - \frac{1}{2})}{\sqrt{(2^{1/R_H} - 1)}\Gamma(R_H)}\right]^{-1} \tag{2.6}$$

where $\Gamma(R)$ is the gamma function, T the peak maximum position, W the full-width at half-maximum (FWHM), A the asymmetry parameter, R_L the decay rate in $2\theta \leq T$, and R_H that in $2\theta > T$. $P(2\theta)$ has a peak half-width of $WA/(1+A)$ at half-maximum height in $2\theta \leq T$ and $W/(1+A)$ in $2\theta > T$.

Profile intensity $y(2\theta_i)_{calc}$ at the ith step is calculated by

$$y(2\theta_i)_{calc} = B + \sum_j \sum_k I_{jk} P(2\theta_i)_{jk}, \tag{2.7}$$

where B is an adjustable background level and I_{jk} is an integrated intensity of the kth component of characteristic X-rays ($K\alpha_1$ or $K\alpha_2$) for the jth reflection. It is given by

$$I_{j1} = I_j/(1+K), \tag{2.8}$$

$$I_{j2} = I_j K/(1+K), \tag{2.9}$$

where K is an adjustable parameter representing the intensity ratio of the $K\alpha_2$ component to $K\alpha_1$ and I_j is the total integrated intensity of these two components.

The peak maximum position of only the $K\alpha_1$ peak, T_{j1}, is refinable, and that of $K\alpha_2$, T_{j2}, is calculated from T_{j1} as

$$T_{j2} = 2\sin^{-1}\left[\lambda_2/\lambda_1 \sin(T_{j1}/2)\right] + e, \tag{2.10}$$

where λ_1 and λ_2 are wavelengths for the $K\alpha_1$ and $K\alpha_2$ components, respectively, and e is an adjustable parameter to correct a peak separation of the α doublet.

The angular variations of parameters B, W_j, A_j, R_L and R_H can be approximate with the following analytical expressions [Toraya, 1986]

$$B(2\theta) = b_1 + b_2 2\theta + b_3 \sin\theta + b_4 \tan\theta, \tag{2.11}$$

$$W(2\theta) = (w_1 + w_2 \tan\theta + w_3 \tan^2\theta)^{1/2}, \tag{2.12}$$

$$A(2\theta) = a_1 + a_2/\sin\theta + a_3/\sin^2\theta, \tag{2.13}$$

$$R_L(2\theta) = r_{L1} + r_{L2}\sin\theta + r_{L3}/\sin\theta, \tag{2.14}$$

$$R_H(2\theta) = r_{H1} + r_{H2}\sin\theta + r_{H3}/\sin\theta, \tag{2.15}$$

where lower-case letters with subscripts on the righthand side of the equations are adjustable parameters.

Summarise, the list of adjustable parameter for instrumental profile fitting function is given in Tab. 2.2

The proposed above model can fit the instrumental function profile defined by some standard reference material pretty well. Otherwise, due to a big number of refinable parameters and the dependence between those parameters obtained from different standard samples can considerably vary. Therefore, the model for instrumental function which based on physical properties of diffractometer is more preferable. In chapter 4 the development of such model will be proposed.

Table 2.2: List of adjustable parameters in instrumental profile fitting

I_j	Integrated intensity of the jth peak
T_j	The jth peak maximum position
K	Intensity ratio of $K\alpha_2$ component to $K\alpha_1$
e	Correction for the peak separation of $K\alpha_1$ and $K\alpha_2$
b_1, b_2, b_3, b_4	Background level
w_1, w_2, w_3	Full-width at half-maximum
a_1, a_2, a_3	Peak asymmetry
r_{L1}, r_{L2}, r_{L3}	Decay rate on the low-angle side
r_{H1}, r_{H2}, r_{H3}	Decay rate on the high-ange side

2.2 Specimen broadening

The specimen profile f after removal of the instrument effect h from the observed profile g, conveys microstructural information representing size effects and lattice distortion (non-uniform microstrain). The overall profile function f is the convolution of the profile functions of these effects [Langford et al., 1988; Langford, 1999]. The following section summarises the theories of line broadening by lattice imperfections, which consist of small crystallites and non-uniform microstrains.

A basic theory of size broadening is presented by making an analogy of the effect of crystallite size on a diffraction pattern to the phenomenon associated with optical gratings [Guinier, 1963]. The optical phenomenon shows that the diffraction maximum depends only on the spacing between gratings and that the width of the diffraction line depends on the number of gratings in a spatial unit. Increasing the density of the grating will decrease the line width.

In the case of radiation diffraction, the number of reflecting lattice planes is analogous to the number of gratings. Reducing the number of lattice planes, however, corresponds to the smaller crystallite size.

Consider a thin plate crystal, large in surface area, which consists of N lattice planes of spacing d (Fig. 2.2). A radiation beam of wavelength λ incident on the

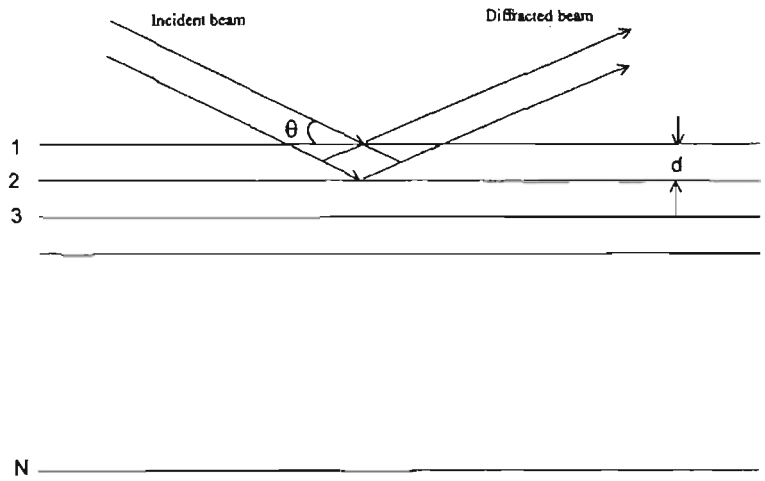

Figure 2.2: Diffraction at the Bragg angle of incident θ by N lattice planes with lattice spacing of d.

surface of the plate at the Bragg incident angle of θ, such that Bragg's law applies

$$\lambda = 2d \sin\theta \tag{2.16}$$

The beam scattered by N planes is in phase producing a scattered ray with amplitude NA, where A is the amplitude for a single lattice plane. If the angle of incidence is changed from θ to $\theta + \delta$, the path difference between two adjacent planes becomes

$$2d \sin(\theta + \delta) = 2d\delta \cos\theta \tag{2.17}$$

The scattered wave is now the sum of the N waves but with a phase difference of

$$2\phi = \frac{4\pi d}{\lambda}\delta \cos\theta \tag{2.18}$$

It can be shown that the intensity of the diffracted beam in a direction $\theta + \delta$ is [Guinier, 1963]

$$I(\delta) = A\frac{\sin^2 N\phi}{\sin^2 \phi} \tag{2.19}$$

$I(\delta)$ approaches zero as

$$N\phi > \pi \quad or \quad \delta > \frac{\lambda}{2Nd\cos\theta} \tag{2.20}$$

which means that the width of the angular domain of the reflection is inversely proportional to Nd. The thickness of the crystal ($L = Nd$, where L is perpendicular to the diffracting planes) is associated with the full width at half-maximum (FWHM) according to the following [Guinier, 1963]

$$FWHM = \frac{0.9 \cdot \lambda}{L \cos\theta} \tag{2.21}$$

2.2.1 The Laue interference function

Discussion on this topic involves use of the reciprocal lattice. Consider a set of three scalar numbers (ξ, η, ζ) defining a point in reciprocal space at a vector distance $\xi\mathbf{a}^* + \eta\mathbf{b}^* + \zeta\mathbf{c}^*$ from the origin, where $\mathbf{a}^*$, $\mathbf{b}^*$ and $\mathbf{c}^*$ are the primitive translation vectors of the reciprocal lattice. By defining the unit vector for the incident X-ray radiation as $\mathbf{s}_0$ and the scattered radiation vector as $\mathbf{s}$, the scattering function $I(\xi, \eta, \zeta)$ gives the maximum intensity when the following conditions of diffraction are met

$$\frac{\mathbf{s} - \mathbf{s}_0}{\lambda} = \frac{\mathbf{S}}{\lambda} = \xi\mathbf{a}^* + \eta\mathbf{b}^* + \zeta\mathbf{c}^* \tag{2.22}$$

$I(\xi, \eta, \zeta)$ can then be considered as a distribution in reciprocal space with its value at any point giving the intensity according to the diffraction conditions with the point being the extremity of the vector $\dfrac{\mathbf{S}}{\lambda}$ [James, 1965]. The total intensity of the scattered waves $I(\xi, \eta, \zeta)$ for any point in the reciprocal space is basically a product of two factors: the modulus of the structure factor $|F(\xi, \eta, \zeta)|^2$, where $F(\xi, \eta, \zeta)$ is the geometrical structure factor or structure factor, and the Laue interference factor $I_0(\xi, \eta, \zeta)$, or

$$I(\xi, \eta, \zeta) = |F(\xi, \eta, \zeta)|^2 \, I_0(\xi, \eta, \zeta) \tag{2.23}$$

The geometrical structure factor can be written as

$$F = \sum f' \cdot \exp(ik\mathbf{S}\rho) \tag{2.24}$$

where the summation is made over all atoms in a unit cell, f' is atomic scattering factor, $k = \frac{2\pi}{\lambda}$ - is the wave-number and ρ is the vector distance of any point in the unit cell from the origin of that cell. Defining

$$p = u\mathbf{a} + v\mathbf{b} + w\mathbf{c} \tag{2.25}$$

the structure factor can now be expressed as

$$F(\xi, \eta, \zeta) = \sum f' \cdot \exp(2\pi i(\xi u + \eta v + \zeta w)) \tag{2.26}$$

where (u,v,w) and $(\mathbf{a},\mathbf{b},\mathbf{c})$ are a set of numbers and a set of primitive translations in crystal-lattice space, respectively. This structure factor term is of importance in the theory of strain broadening by dislocations.

The interference function $I_0(\xi, \eta, \zeta)$ for a parallepiped crystal fragment with N_1, N_2, N_3 points parallel to the edges a, b, c respectively has a general form of [James, 1965]

$$I_0(\xi, \eta, \zeta) = \frac{\sin^2 N_1\pi\xi}{\sin^2 \pi\xi} \cdot \frac{\sin^2 N_2\pi\eta}{\sin^2 \pi\eta} \cdot \frac{\sin^2 N_3\pi\zeta}{\sin^2 \pi\zeta} \tag{2.27}$$

The interference function can be regarded as a representation of a periodic distribution dependent on the vector $\frac{\mathbf{S}}{\lambda}$ in the reciprocal-lattice space. In circumstances where a crystallite consists of a row of N equally-spaced points along the a axis, sheets of crystallites form in the $\mathbf{b}^*\mathbf{c}^*$ planes of the reciprocal lattice and are perpendicular to the a axis. Since now $N_2 = N_3 = 1$, the Laue interference function becomes

$$I_0(\xi) = \frac{\sin^2 N_1\pi\xi}{\sin^2 \pi\xi} \tag{2.28}$$

Considering the diffraction condition $\sin 2\theta = \frac{\lambda}{a}$ and the appropriate crystal lattice space distance $x = \frac{\xi}{v}$, the Laue interference function can be written as

$$I_0(\xi) = \frac{\sin^2 N\pi xa}{\sin^2 \pi xa} \tag{2.29}$$

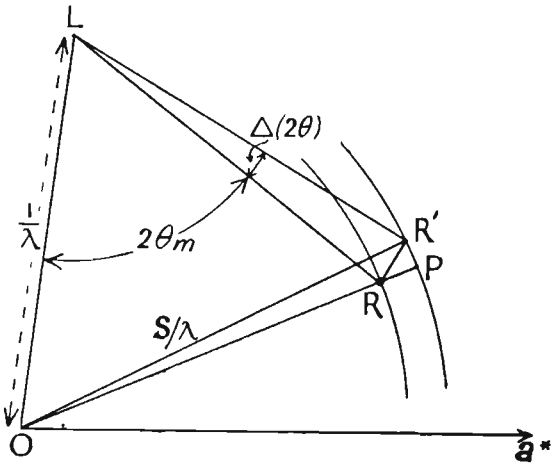

Figure 2.3

Consider now a system with a large number of identical crystallites. The average intensity of the scattered radiation corresponding to the distribution of the interference function can be calculated by including all possible crystallographic orientations. The calculation gives the average interference function $\overline{I_0}$ according to diffraction by crystallites with random orientation. Determining the appropriate distribution functions associated with the interference function is, therefore, essential in the intensity calculation.

If $\overrightarrow{OR}$ and $\overrightarrow{OR'}$ (see Fig. 2.3) are the position vectors for neighbouring reciprocal points (h, k, l) and $(h + \xi, k + \eta, l + \zeta)$, the interference function at R' can be written as $I_0(\xi, \eta, \zeta)$ [James, 1965]. Consider ds is a small element of the surface area for a sphere of radius of OR'. The diffracted intensity of radiation through an angle 2θ over an area ds at a distance from a point of origin $\rho = 2\sin\theta = \dfrac{|\mathbf{S}|}{\lambda}$, is determined by

$$\overline{I_0}(\rho) = \frac{1}{4\pi p^2} \int I_0(\xi, \eta, \zeta) ds \tag{2.30}$$

The integrated intensity can then be calculated by integrating $\overline{I_0}$ with respect to ρ.

The integral breadth of the line is given by

$$\beta(\rho) = \frac{\int \overline{I_0}(\rho)d\rho}{\overline{I_0(m)}} \tag{2.31}$$

where $\overline{I_0}(m)$ is the maximum value of $\overline{I_0}$. James [1965] used a Gaussian function to approximate the interference function for a cubic crystal system and found that the integral breadth of a diffraction line corresponds to the crystallite size following the Scherrer equation

$$\beta_{size}(2\theta) = \frac{K\lambda}{L\cos\theta} \tag{2.32}$$

where K is the Scherrer constant those value depends in general on the external form of the crystallites as well as on the order of the diffraction. Values for K have been tabulated for some cubic crystal solids [Stokes and Wilson, 1944]. It was argued by Stokes and Wilson [1944] that, usually, $K = 1$ is adequate to approximate the cubic crystallites.

2.2.2 Classical theory by Stokes and Wilson

This theory was first introduced by Stokes and Wilson [1944] after making use of the structure factor to calculate the non-linear strain (or, lattice distortion) from the integral line-breadth.

Consider a displacement of a unit cell positioned at $\mathbf{r}$ by a vector $\mathbf{u}(\mathbf{r})$. Another cell is also displaced with a distance t from the first cell and direction with a unit cell $\mathbf{n}$. In general, this displacement involves both rotation and translation. However, the rotation will not affect the phase of the scattered radiation unless it is very large compared to the translation. The rotational structure factor contribution can then be neglected [James, 1965]. Using (2.24), the structure factor for the displaced cells

is

$$\mathbf{F}' = \mathbf{F}\exp(iK\mathbf{S}\cdot\mathbf{u}(\mathbf{r})) \tag{2.33}$$

$$\mathbf{F}'' = \mathbf{F}\exp(iK\mathbf{S}\cdot\mathbf{u}(\mathbf{r}+\mathbf{n}t)) \tag{2.34}$$

For large values of t, $F'F''^{*}$ vanishes. For small t, $\mathbf{u}(\mathbf{r}+\mathbf{n}t)$ can be expanded in powers of t. Taking the first two terms gives

$$\mathbf{u}(\mathbf{r}+\mathbf{n}t) = \mathbf{u}(\mathbf{r}) + t\mathbf{n}\cdot\nabla\mathbf{u} \tag{2.35}$$

$\nabla\mathbf{u}$ is a tensor for which the symmetrical part gives the strains in the crystal at the point under consideration. In first approxymation, the intensity is

$$J_t = \overline{F'F''^{*}} = |F|^2\,\overline{\exp(ik\mathbf{S}\cdot t\mathbf{n}\cdot\nabla\mathbf{u})} \tag{2.36}$$

If $\mathbf{n}$ is perpendicular to the (hkl) planes, it can be found that $\mathbf{S} = \mathbf{n}\,|\mathbf{S}| = 2\mathbf{n}\sin\theta$. Defining $\mu = k\,|\mathbf{S}| = \dfrac{4\pi\sin\theta}{\lambda}$ then

$$J_t = \overline{F'F''^{*}} = |F|^2\,\overline{\exp(i\mu t\mathbf{n}\cdot\nabla\mathbf{u}\cdot\mathbf{n})} \tag{2.37}$$

or,

$$J_t = |F|^2\,\overline{\exp(i\mu e_{hh}t)} \tag{2.38}$$

since $\mathbf{n}\cdot\nabla\mathbf{u}\cdot\mathbf{n}$ is the tensile strain e_{hh} in the direction of $\mathbf{n}$ and perpendicular to the reflecting planes.

The integral breadth of a diffraction line can then be calculated using

$$\beta(2\theta) = \frac{|F|^2\,\lambda}{\cos\theta}\int J_t dt \tag{2.39}$$

If $w(e)de$ is a fraction of a crystal having e_{hh} between e and $e+de$ along the scattering vector, the "apparent particle size" can be determined using

$$D_{app} = \int\frac{J_t dt}{|F|^2} = \int_{\infty}^{\infty}\int_{\infty}^{\infty}\omega(e)\exp(i\mu te)dedt \tag{2.40}$$

It can be shown that

$$D_{app} = \frac{\lambda}{2\sin\theta}\omega(0) \tag{2.41}$$

$$\beta = \frac{2\tan\theta}{\omega(0)} \tag{2.42}$$

where $\omega(0)$ is $\omega(e)$ when $e = 0$. The 'apparent strain' is defined as

$$\epsilon_{app} = \beta\cot\theta = \frac{2}{\omega(0)} \tag{2.43}$$

2.2.3 Dislocations and line broadening

Dislocations are one-dimensional defects in a crystal. The theory of line broadening by dislocations has been reviewed by [Ungar, 1999]. The theory requires the definitions of vector positions of two cells when they are distorted and undistorted. These are, respectively, $\mathbf{r}_s^0$ and $\mathbf{r}_{s'}^0$ for the undistorted cells and $\mathbf{r}_s$ and $\mathbf{r}_{s'}$. for the distorted cells. According to the theory of kinematic scattering, the intensity of a Bragg reflection for a crystal with one atom in a unit cell is given by

$$I(\mathbf{k}) = f'^2 \sum exp(i\mathbf{k}\cdot(\mathbf{r}_s - \mathbf{r}_{s'})) \tag{2.44}$$

where $\mathbf{k}$ is the diffraction vector $(\mathbf{k} - \mathbf{k}_0)$, $\mathbf{k}$ and $\mathbf{k}_0$ being the wave vectors of the scattered and the incident waves, respectively. The diffraction vector can be expressed as

$$\mathbf{k} = \mathbf{g} + \mathbf{s} \tag{2.45}$$

where $\mathbf{g}$ is the reciprocal lattice vector related to the associated Bragg reflection and $\mathbf{s}$ is a vector which scans the reciprocal space in the vicinity of $\mathbf{g}$.

If $\delta\mathbf{r}_s$ is the displacement of a cell from the undistorted position, it follows that

$$\mathbf{r}_s = \mathbf{r}_s^0 + \delta\mathbf{r}_s \tag{2.46}$$

The intensity of the Bragg reflection can then be written as [Ungar, 1999]

$$I(\mathbf{s}) = f'^2 \sum exp\left[i\mathbf{s}\cdot(\mathbf{r}_s^0 - \mathbf{r}_{s'}^0)\right] exp\left[i\mathbf{g}\cdot(\delta\mathbf{r}_s^0 - \delta\mathbf{r}_{s'}^0)\right] \tag{2.47}$$

where the term $\mathbf{s}\delta\mathbf{r}$ is neglected. Equation (2.46) is of significance in the study of line broadening by dislocations from the following perspective:

- for a large and perfect crystal, the Bragg reflection is a sharp delta function;
- strain information is contained in the $\delta\mathbf{r}$;
- a Fourier transform of the phase shifts caused by the displacement component is represented in

$$A = exp\left[i\mathbf{g}\cdot(\delta\mathbf{r}_s^0 - \delta\mathbf{r}_{s'}^0)\right] \tag{2.48}$$

- the equation contains information about the crystal size.

The displacement component A becomes the focus of the theory. Several approaches have been developed by employing the displacement component A from different ways to obtain the strain-related information [Warren and Averbach, 1950; Groma et al., 1988; Krivoglaz, 1996].

2.2.4 Apparent crystallite size and strain

Wilson [1970] expressed the specimen broadening f as the inverse transform of the Fourier transforms of size $[V(t)]$ and strain $[Y(t)]$ effects

$$f(x) = \frac{\int V(t)Y(t)exp(-2\pi ixt)dt}{U} \tag{2.49}$$

where U is the volume of the unit cell. $V(t)$ can be interpreted as the volume common to a crystallite and its 'ghost' displaced a distance t in the direction of the diffraction vector $\mathbf{d}_{hkl}^*$ (see Fig. 2.4), where

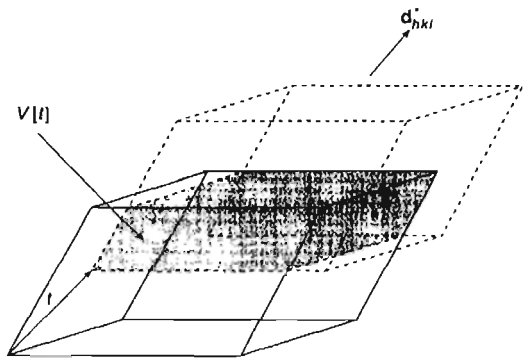

Figure 2.4: Crystal A of volume V and its 'ghost' B which is displaced by a distance t in the direction of the diffraction vector $\mathbf{d}^*_{hkl}$ [Langford, 1999].

$$|\mathbf{d}^*_{hkl}| = \frac{1}{d} = \frac{2sin\theta}{\lambda} \tag{2.50}$$

Langford [1999] applied the pattern decomposition approach to interpret the apparent size by employing reciprocal space integral breadth β^*_S in the absence of the strain effects. The size integral breadth is

$$\beta^*_S = \frac{V(0)}{\int_{-L}^{L} V(t)dt} \tag{2.51}$$

where $V(0)$ is the mean volume of crystallites and L is the value of t for which $V(t) = 0$ or the maximum thickness [Guinier, 1963]. The integral breadth apparent size $D_{app,\beta}$ is defined as

$$D_{app,\beta} = \frac{1}{\beta^*_S} \tag{2.52}$$

which can be interpreted as the volume-weighted thickness of crystallites measured in the direction of [hkl] [Langford, 1999]. The reciprocal of the slope of the Fourier transform of the normalised profile $\frac{V(0)}{V'(0)}$ is also a measure of crystallite thickness known as the Fourier apparent size $D_{app,F}$ [Wilson, 1963], or

$$D_{app,F}, = -\frac{V(0)}{V'(0)} \tag{2.53}$$

The integral breadth and Fourier sizes, D_β and D_F, are weighted average thickness in a particular direction which does not represent the actual mean dimensions and indication of shapes. It can be shown that the mean crystallite diameter $\langle D \rangle$ for spherical crystallites is given by [Wilson, 1962]

$$\langle D \rangle = \frac{4D_\beta}{3} \tag{2.54}$$

or

$$\langle D \rangle = \frac{3D_F}{2}. \tag{2.55}$$

Relationships between D and crystallite dimensions for various shapes have been reported as well [Langford and Louer, 1982; Langford, 1992, 1999].

Stokes and Wilson [1944] introduced the concept of apparent strain $\epsilon_{\beta,app}$ in association with the strain integral breadth β_D^* according to

$$\epsilon_{\beta,app} = \frac{2\beta_D^*}{d^*} \tag{2.56}$$

The apparent strain can be associated with the 'actual strain' e according to

$$\epsilon_{\beta,app} \approx 5\langle e^2 \rangle^{1/2} \tag{2.57}$$

where $\langle e^2 \rangle^{1/2}$ is the root mean square strain or e_{rms}.

In conclusion, §2.2 has explored the theories of line broadening due to crystallite size and strain. The discussion does not include line broadening due to mistakes or stacking faults. Two principal ways to introduce size and strain effects to the broadening formulation have been shown, i.e. using the line width (integral breadth method) and the Fourier methods. These principles then become the bases of the crystallite size and strain analysis which are discussed in the following section.

2.3 Methods of crystallite size and strain analysis

The theory of x-ray line broadening was developed initially using the Fourier transform approach. The application of this theory was performed, for example, by Warren and Averbach [1950, 1952]. It was also found that the classical Gaussian and Lorentzian PSF can be used to fit the diffraction pattern [Klug and Alexander, 1974]. In subsequent developments [Langford, 1978], line profile analysis was conducted by fitting appropriate mathematical functions such as the Voigt function to the diffraction data and then extracting size and strain parameters from the line width.

Various studies have been reported on the development of line broadening analytical methods. Three classical methods which can be used to extract crystallite size and strain contributions from x-ray line broadening data are Fourier transform method [Klug and Alexander, 1974], integral breadth method involving Gaussian and Cauchy functions, line profile variance methods.

As described briefly in §1.1, deconvolution of 'pure' specimen broadening must be carried out since an observed profile g is a convolution of the instrumental h and pure specimen f profiles (Fig. 1.1) following (1.1). If f represents the combined crystallite size and strain contributions to the profile, then f is a convolution of size and strain functions, f_D and f_S, respectively, [Langford, 1999]

$$f = f_S \otimes f_D \tag{2.58}$$

Classical size and strain analysis methods deduced microstructural information directly from experimental data of distorted metals [Warren and Averbach, 1950, 1952; Guinier, 1963; Klug and Alexander, 1974].

Recent improvements in computing power have allowed diffraction pattern fitting to be performed more effectively. However, progress has been limited by the use of

profile fitting functions for modelling which may not be physically correct for particular classes of materials. There are three ways to analyse crystallite size and strain by profile fitting, i.e. the use of a function containing microstructural parameters to fit the real-space diffraction data, the use of a function to fit the Fourier transforms of the diffraction data, and the use of an analytical function to fit diffraction data followed by a Fourier-based analysis.

Multi-line profile fitting methods are size and strain assessment techniques which employ more than one diffraction line. These methods might be expected to be superior to single-line procedures as the angular dependence of the separate strain and size contributions to the specimen function f are markedly different. Two wellknown multi-line methods have been widely used in the line broadening analysis, i.e. the Warren-Averbach [1950; 1952] and Williamson-Hall [1953] methods. Single-line methods, however, are recognised as rapid size and strain analysis procedures [de Keijser et al., 1982; Delhez et al., 1982] which under some assumptions are adequate for revealing the micro structural character of the specimen [York, 1999].

The following sub-sections explain the approaches which have been widely used for the extraction of strain-size information by x-ray diffraction line profile analysis.

2.3.1 Method of Warren and Averbach

The Warren-Averbach method [1950; 1952] is a multi-line size and strain procedure. If the instrumental profile function h is assumed, the specimen function f can be deconvoluted from the observed function f. Consider H, G and F are the Fourier transforms of h, g and f respectively. The deconvolution can be performed in terms of complex Fourier transforms as follows

$$F(n) = \frac{G(n)}{H(n)} \tag{2.59}$$

According to the Stokes' method [Stokes, 1948], the inverse Fourier transform gives the specimen broadened line profile

$$f(x) = \frac{1}{\sqrt{2\pi}} \sum_x \frac{G(n)}{H(n)} \exp(-\frac{2\pi i x n}{x_m}) \tag{2.60}$$

where x_m is the minimum value of x when the intensity can be considered to have dropped to its background value. The specimen profile can be expanded into sine and cosine terms, according to

$$f(x) = \frac{1}{\sqrt{2\pi}} \left[\sum_x F_r(n) cos(-\frac{2\pi x n}{x_m}) + \sum_x F_i(n) sin(-\frac{2\pi x n}{x_m}) \right] \tag{2.61}$$

It follows that computations of the Fourier transforms are greatly simplified if the g, h and f functions are symmetrical because the sine terms vanished. However, symmetric profiles are rarely observed. For instance, if Bragg-Brentano x-ray diffractometer is used, h can be asymmetric due to the introduction of $K\alpha_2$ peaks. Corrections for the $K\alpha$ doublet can be performed by mathematical elimination of the α_2 contribution [Rachinger, 1948; Huang and Parrish, 1975] by use of the iterative folding (convolution) method [Ergun, 1968].

According to (2.60), the specimen broadening f can be calculated directly from the observed profile g without knowledge on the peak shape function of the h and g profiles. However, it requires an accurate determination of the background limit x_m to give an accurate f. In addition, the specimen broadening should be sufficiently large relative to the instrument broadening in order to avoid unstable and inaccurate deconvolution [Delhez and de Keijser E. J. Mittemeijer, 1980]. Furthermore, the truncation of the Fourier series will always produce profile-tail ripples regardless of the extent of the specimen broadening. The major disadvantage is that overlapping peaks cannot be resolved without restoring the profiles with peak-shape functions. This step introduces further biases into the results. As a result, the Stokes deconvolution method can be performed appropriately only for materials with high crystallographic

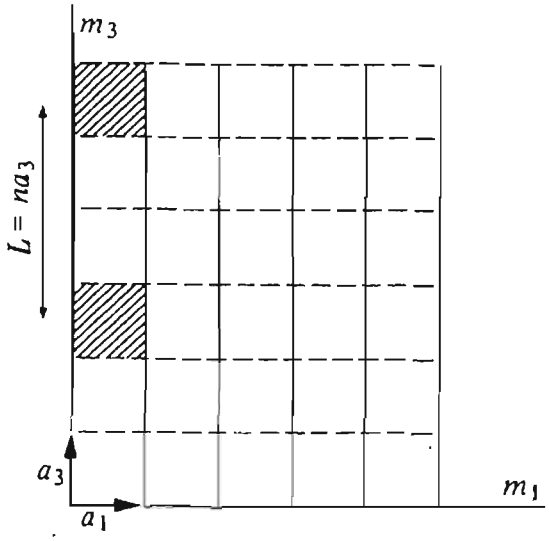

Figure 2.5: A crystal as an assemblage of columns of cells along the a_3 direction. N_3a_3 is the column length (after Warren [1969]).

symmetry [Balzar, 1999].

In order to deal with overlapping peak difficulties,[Balzar, 1992] introduced the use of the Voigt function, a convolution of a Lorentzian and a Gaussian function, as the peak shape of the h and g profiles. Since the convolution of two Voigt functions is also a Voigt function, the integral breadths of h, g and f profiles then have the relationships

$$\text{Lorentzian part:} \quad \beta_{fL} = \beta_{gL} - \beta_{hL} \tag{2.62}$$

$$\text{Gaussian part:} \quad \beta_{fG}^2 = \beta_{gG}^2 - \beta_{hG}^2 \tag{2.63}$$

The specimen breadths β_{fL} and β_{fG} can then be used to reconstruct the specimen profile f.

In the Warren-Averbach method, the cosine Fourier coefficients (A_n) of f are used to give information about crystallite size and strain, since the A_n coefficients are the product of two terms [Warren and Averbach, 1950]. The first term depends only on the column length (size coefficient S - (see Fig. 2.5) and the second term depends

only on distortion of the domains (distortion coefficient D):

$$A_n = A_n^S A_n^D \tag{2.64}$$

Taking l as the undistorted distance between two unidirectional crystallographic positions, a linear curve can be developed by plotting $lnA(l)$ vs. l^2 since each coefficient can be written as [Delhez and de Keijser E. J. Mittemeijer, 1980]

$$A_n^S = \frac{N(n)}{N_3} \tag{2.65}$$

$$A_n^D = \exp(-2\pi^2 l^2 \langle \epsilon^2(l) \rangle) \tag{2.66}$$

where $N(n)$ is the average number per column of pairs of unit cells a distance of n cells apart, N_3 is the average domain size in unit cells perpendicular to the reflecting planes, and $\langle e^2(l) \rangle$ is the rms (root-mean square) strain. The slope gives the rms strain value whereas the intercept produces the size coefficient function A_n^S from which the average surface weighted domain size can be obtained by

$$\left. \frac{dA_n^S}{dn} \right|_{n \to 0} = -\frac{1}{N_3} \tag{2.67}$$

Use of the Stokes' deconvolution procedure prior to the Warren-Averbach method, however, may introduce some errors in the microstructural information obtained from the method. Also, the application of this method is limited to high symmetry materials. Balzar [1992] proposed an X-ray size-strain analysis procedure which is a combination of the profile fitting and multi-line Warren-Averbach methods. In this approach, the instrumental profile is modelled with a split Pearson-VII function and the specimen profile with a Voigt function. The convolution between the functions is fitted to the measured profile. The Gaussian and Lorentzian components are then used to calculate the cosine Fourier coefficients, A_n. Both size and strain contributions were modelled using Voigt functions. The Warren-Averbach method is applied to the Fourier coefficients to determine the volume- and surface-weighted average domain

sizes and rms strain. The profile fitting procedure proposed by Balzar is applicable to overlapping peaks. However, the technique requires two orders of reflection of the same plane, which limits its applications.

2.3.2 Analysis according to Williamson and Hall

In the Williamson-Hall method [1953], it is assumed that particle size broadening of a line at Bragg position θ_i follows the Scherrer equation (with $K = 1$)

$$\beta_D = \frac{\lambda}{D \cos \theta_i} \tag{2.68}$$

while strain broadening is described by

$$\beta_\epsilon = 4\epsilon \tan \theta_i \tag{2.69}$$

where D is the crystallite size, e is the upper limit strain and β is the integral breadth of the peak. It is assumed that both the size and strain broadening contributions of the specimen to the profiles are Lorentzian. Langford [1992] emphasised that this method should not be used quantitatively but can provide qualitative information on the nature of microstructural effects causing peak broadening. The total broadening is described by the sum of (2.68) and (2.69) according to

$$\beta \cos \theta_j = \frac{\lambda}{D} + 4\epsilon \sin \theta_i. \tag{2.70}$$

The use of the Voigt function in an 'improved' Williamson-Hall method was introduced by Langford [1992] using a pattern decomposition approach. The integral breadth β of a Voigt function is approximated by

$$\beta^2 \approx \beta_L \beta + \beta_G^2 \tag{2.71}$$

where β_L and β_G are the integral breadths of the Lorentzian and Gaussian profiles, respectively, and

$$\beta_L = \frac{1}{D} \quad ; \quad \beta_G = \frac{\epsilon \cdot d^*}{2} \tag{2.72}$$

where $d^* = \frac{2sin\theta}{\lambda}$, with the integral breadths being in reciprocal units.

2.3.3 Single-line integral breadth method

The single-line methods can be performed either in Fourier or real space [Delhez and de Keijser E. J. Mittemeijer, 1980; de Keijser et al., 1982]. Most of the Fourier methods are vulnerable to deconvolution procedures particularly if the background is determined inappropriately or if the peaks under investigation overlap. Some improvements have been made by employing profile shape functions [de Keijser et al., 1983] so that the required Voigt integral breadths, for example, can be obtained readily by

$$\left.\frac{dA_n^f}{dn}\right|_{n\to 0} = -\frac{2\beta_L^f}{a} \tag{2.73}$$

$$\left.\frac{d^2A_n^f}{dn^2}\right|_{n\to 0} = \frac{4\left(\beta_L^f\right)^2}{a^2} - \frac{2\pi\left(2\beta_G^f\right)^2}{a^2} \tag{2.74}$$

where β_L^f is the Lorentzian breadth of the specimen profile f and a is period in a 2θ scale. These expressions were derived using (2.67) and approximating the size-broadened profile by a Laue interference function [Delhez et al., 1982] to give

$$\left.\frac{d^2A_n^S}{dn^2}\right|_{n\to 0} = \frac{4\left(\beta_L^f\right)^2}{a^2} \tag{2.75}$$

The area-weighted average crystallite size $\langle D\rangle_a$ and the rms strain $\langle e^2\rangle^{1/2}$ were calculated using [de Keijser et al., 1983]

$$\langle D\rangle_a = \frac{\lambda}{2\beta_L^f\cos\theta} \tag{2.76}$$

$$\langle e^2\rangle^{1/2} = \frac{\beta_G^f\tan\theta}{2\sqrt{2\pi}} \tag{2.77}$$

The correlations between the parameters for the pseudo-Voigt and Voigt functions have been parameterised [David, 1986] which leads to the possibility of performing

size and strain analysis using the pseudo-Voigt function, but with the introduction of additional uncertainties due to the parameterisation.

The integral breadth single-line methods use peak-shape functions to fit a diffraction peak and relate the adjusted peak width parameters with the microstructural information. This method of extraction of strain and/or size information from the analysis of single Bragg peaks is problematic in that the shape of a single Bragg peak may provide reasonable results for either strain or size modelling, but not where both effects are present. In situations where the broadening is likely to be strain-only or size-only, profile fitting is performed by associating the specimen-only function f with the assumed line width expression for either strain or size broadening, e.g. the Scherrer line width. Furthermore, the method requires use of physically sensible functions for the determination of functions h and g which is particularly difficult to achieve for XRD data due to the complex form of the instrument function h.

In the past, a single function such as Gaussian or Lorentzian was mainly used to fit both the size and strain components. However, theory and experiment showed that this approach to be inappropriate [de Keijser et al., 1982; Balzar, 1992] presumably due to the absence of any physical basis for use of the profile functions. The pseudo-Voigt function has also been used to fit X-ray diffraction profiles [Enzo and Schiffini, 1999]. However, the use of the pseudo-Voigt function also has no physical foundation and may provide unreasonable results.

Langford [1978] made substantial progress in dealing with the complex form of the profile function by employing the Voigt function (a convolution of Gaussian and Lorentzian functions) for X-ray diffraction profile fitting which was found to give a better approximation than its 'derivatives', i.e. Gaussian and Lorentzian functions.

The single-line integral-breadth method for extracting size and strain using the Voigt function can be applied according to the procedure proposed by de Keijser

et al. [1982] who used Gaussian and Lorentzian breadths (β_{hG} and β_{hG}, respectively) to estimate the specimen-only contributions (β_{hG} and β_{hG}) according to Langford [1978] with the expressions given by (2.62).

The angular dependence of the peak breadth β can be analysed to give crystallite size and strain values, by assuming that the Gaussian component (β_{hG}) is ascribed to strain and the Lorentzian component (β_{hL}) to size broadening

$$\beta_{fG} = 4\epsilon \tan\theta_i \tag{2.78}$$

and

$$\beta_{fL} = \frac{\lambda}{\langle D \rangle_V \cos\theta_i} \tag{2.79}$$

where ϵ is the weighted average strain, λ is the radiation wavelength and $\langle D \rangle_V$ is the volume-weighted average size.

2.3.4 Techniques of Whole-Powder Fitting

The Rietveld method for analysis of powder diffraction data [Rietveld, 1967, 1969] involves the fitting of the entire observed profile with a simulated pattern derived using models for the crystal structure and diffraction peak profiles. The method was originally developed for crystal structure analysis. The method may also provide microstructural information from peak profile character. The line profile model, which is introduced in all major Rietveld-refinement programs, is a generalisation of the Thompson et al. [1987] approach. It implicitly assumes that the observed and constituent line profiles are Voigt functions [Balzar and Ledbetter, 1995]. A convolution of any number of Voigt functions is also a Voigt function, therefore, one can write the following expressions for Gaussian and Lorentzian observed line widths [Balzar and

Popa, 2005]:

$$\Gamma_G^2 = U\tan^2\theta + V\tan\theta + W + P/\cos^2\theta \tag{2.80}$$

$$\Gamma_L = X/\cos\theta + Y\tan\theta + Z. \tag{2.81}$$

Here, Γ is the full width at half-maximum (FWHM) of the line profile, U, V, W, X, Y and Z are refinable parameters and L and G denote Lorentzian and Gaussian profiles, respectively.

As the parameters in Eqs. (2.80) and (2.81) are FWHMs, they should be converted to integral breadths of size-broadened and strain-broadened profiles before calculating associated domain size and strain values (see Tab. 2.1). Then, the Lorentz and Gauss integral breadths are combined for both size and strain parts according to the relation (see Tab. 2.1):

$$\beta_i = (\beta_G)_i \frac{\exp(-k^2)}{1-\mathrm{erf}(k)}; \quad k = \frac{\beta_L}{\sqrt{\pi}\beta_G} \tag{2.82}$$

where i stands for S and D. Only now can β_S and β_D be related to the corresponding values of D_V and e, according to following equations:

$$\beta_S = \frac{\lambda}{D_V\cos\theta}; \quad e = \frac{\beta_D}{4\tan\theta}. \tag{2.83}$$

2.3.5 Crystallite size distribution

The crystallite size distribution may be an important descriptor for materials with regard to the chemical and physical properties. For example, the activity and selectivity of catalysts are influenced by the size distribution. It is therefore desirable to determine this additional size information. This may be achieved through line broadening analysis.

If the Fourier method is used, the size (or, column length) distribution can be determined from the second derivative of the size Fourier coefficient A_n^S [Warren,

1969]

$$\frac{d^2 A_n^S}{dn^2} = \frac{p(|n|)}{N_3} \tag{2.84}$$

where p is the column-length distribution function.

The effect of a crystallite size distribution on diffraction line profiles has been investigated by Langford et al. [2000] by summing the intensity in reciprocal space (2.49), with the absence of the strain component, after applying an assumed Gaussian and lognormal distribution function as a weight factor for a particular morphology. The effect of a unimodal distribution of crystallite size on a diffraction line profile are to reduce its width and to disperse its tail. A line profile analysis was applied to the XRD pattern of CeO_2 nanopowder and resulted in a lognormal distribution mean value of 2.3 nm, which differed from the TEM result of 3.5 nm. They argued that this difference can be due to limited number of particles considered in the TEM analysis and also due to insufficient sampling. Note that the presence of any microstrain in the specimen was ignored in the study which may contribute to the XRD and TEM sizes difference.

Popa and Balzar [2002] developed an analytical size profile function which includes the empirical lognormal and Poisson distributions. The size function can readily be convolved with the strain and instrument functions. A test using CeO_2 powders showed that a 'super-Lorentzian' profile can be modelled with a broad lognormal size distribution. It was also shown that the common Voigt function cannot model very narrow and broad size distributions. It was argued that the crystallite size distribution cannot be fully determined by diffraction analysis. For example, a 'super-Lorentzian' character can be caused either by broad lognormal or multimodal size distributions. Transmission electron microscopy may be required to explain the true distribution.

2.3.6 Application and comparison of the methods

The Warren-Averbach method is commonly used in size and strain analysis despite its disadvantages. Some applications of the method, particularly for deformed metals and alloys, were compiled by Klug and Alexander [1974]. It appears that the Warren-Averbach method cannot be considered as a general size and strain analysis method due to inherent problems associated with truncation of line profiles and initial slope determination. This is a result of the 'hook' effect which results from inaccurate determination of background level. As a consequence, the Fourier and variance sizes, for instance, are very different by a factor which can be as high as two [Langford et al., 1988].

The Warren-Averbach and 'double-Voigt' methods were applied to the 'classical' materials W and MgO by Balzar [1999]. Standard specimens made from the same materials were used to deconvolute the instrument profile. Size and strain analysis was performed to obtain the relative values rather than the absolute values. It was concluded that size and strain profiles may be modelled accurately with the Voigt function. It was also found that there was a consistent relationship between the results for Warren-Averbach and integral breadth methods. In general, however, the methods showed small but systematic disagreement in the results.

The development of microstructure in nanocrystalline cerium oxide prepared by thermal decomposition of cerium (IV) oxide nitrate has been studied with x-ray diffraction data using the pattern decomposition method [Guillou et al., 1995]. The Williamson-Hall plots were used to test for anisotropy effects and showed no size or strain anisotropy effects. The apparent volume weighted average size and the apparent strain were calculated following the 'average size and strain plot' procedure given by Langford [1992]. It was found that the crystallites could be described as spherical,

and that their dimensions increased with annealing temperature. The diffraction diameter was markedly smaller than the SEM 'particles' diameter indicating that the SEM 'particles' consist of clusters of coherently diffracting domains. It was also found that the rms strain decreases progressively with annealing temperature.

Another study of microstructure development of nanocrystallite cerium oxide was described [Audebrand et al., 2000b] with particular reference to the growth of the crystallite size. The Williamson-Hall method was used to identify a size anisotropy. The size analysis was performed using the Stokes' deconvolution Warren-Averbach [Warren and Averbach, 1952] and the Langford [1992] average size and strain methods. The values of Fourier and Langford sizes were significantly different which was argued to be due to the presence of a crystallite size distribution. It was found that the distribution becomes narrower when the temperature increases. Again, larger SEM 'particles' than the crystallite size were found which was indicative of 'particles' composed of clusters of domains. Microstructural investigation using TEM showed that TEM 'particles' are crystallites in the sense of coherently diffracting domains [Auffredic et al., 1995] .

The Voigt integral breadth single-line method has been applied to various types of materials, for instance metals [de Keijser et al., 1982], β-SiC-whisker+Al_2O_3 composites [Balasingh et al., 1991] and MgO sintered ceramics [Pratapa et al., 2002]. The method relies on the assumption that strain contributes only to the Gaussian component of the Voigt function and that the size broadening contributes only to the Lorentzian component [de Keijser et al., 1982]. In general, analysis for different reflections gave results with reasonable agreement. Consistent results for reflections from the same crystallographic family were also obtained when the method was applied to nickel layers [de Keijser et al., 1982]. These results support the proposition that size and strain analysis using a single reflection should be adequate in general cases

[York, 1999]. Note, however, that Gaussian-strain and Lorentzian-size assumptions have been challenged recently [Wu et al., 1998a,b; Stephens, 1999] in terms of the anisotropic size and strain effects.

The Rietveld size-strain method has been used widely for strain and size analysis [Wu et al., 1998b; Nakamura et al., 2000; Pratapa et al., 2002]. The peak-shape function incorporated in the fitting procedure is of importance for assessments of the size and strain. The effect of crystallite anisotropy on diffraction peak broadening has been modelled [Greaves, 1985; Wu et al., 1998a; Stephens, 1999], and some Rietveld programs have incorporated anisotropic broadening into the refinement procedures. Larson and von Dreele [1987], for example, included an additional parameter to model the anisotropic size and two additional parameters to model the isotropic and anisotropic strains which were then incorporated into the Lorentzian profile. The model was applied, for instance, by Nakamura et al. [2000] to investigate dislocation characteristics in $LaNi_5$ which was subjected to an activation process and hydriding dehydriding cycles. Reasonable agreement was achieved when the dislocation results were contrasted to TEM data.

Four important observations can be summarised from the literature on strain and size assessment methods:

1. The methods which are commonly used to determine crystallite size and strain from line broadening are Fourier, variance and integral breadth methods. The Fourier methods have inherent problems mostly related to the deconvolution process and overlapping peaks.

2. The sources of disagreement among numerical results from size and strain analysis can be due to definitional differences for the parameters being used. The Fourier and integral breadth methods define the crystallite size as the volume-average dimension perpendicular to the reflecting planes, while the variance

method interprets the size as the cube root of the volume of the crystallites. In terms of strain, the Fourier method gives the rms strain $\langle e^2 \rangle^{1/2}$ in a direction perpendicular to the reflecting planes and averaged over a distance L. The integral breadth method provides an approximation to the strain value as the upper limit e such that $e \simeq 1.25\langle e^2 \rangle^{1/2}$, while the variance method gives $\langle e^2 \rangle^{1/2}$. The apparent size and strain values can be associated with the rms values after appropriate correction. Mean diameter $\langle D \rangle$ is $\frac{4D_{app,\beta}}{3}$ (calculated by integral breadth method) or $\frac{3D_{app,F}}{2}$ (by Fourier method), while the apparent strain can be associated with either rms strain or upper limit strain, by $e_{app} \approx 5e_{rms}$ or $e_{app} \approx 4\epsilon$.

3. There is no integral-breadth profile fitting procedure which is based on a physical model related to the microstructure of specimen.

Chapter 3

Development of the convolution model for size and strain line broadening

It was shown by Langford et al. [2000]; Popa and Balzar [2002] that the Voigt-based size-strain assessment method, wich was described in §2.3.4, can be used to obtain reasonable strain values but dubious size values. The latter observation could be attributed to the Voigt function not accommodating the size distribution. Moreover, the Voigt function is used for size and strain analysis by assuming that the size contributes only to the Lorentzian component and the strain to the Gaussian component. Further investigations showed that the Voigt function cannot be used if the diffraction line shape lies outside the Gaussian and Lorentzian regions, notably within the 'super-Lorentzian' region. Despite these limitations, the Voigt function provides the insight that a specimen profile function should be a convolution of functions from individual microstructural effects, that means a convolution of Gaussian-strain and Lorentzian-size profiles.

This chapter describes the development of a new convolution model for crystallite size and strain determination from diffraction line broadening. The size profile component function for the model involves a size parameter and a size distribution parameter which describes the dispersion of crystallite sizes. The involvement of the size distribution parameter is expected to advance the existing models for size and strain evaluations. The strain profile component function is Gaussian which can be used for strain modelling of small strain [Warren, 1969; Delhez et al., 1993; Balzar, 1999; Kojdecki, 2004].

3.1 Diffraction peak profiles from spherical crystallites with lognormal size distribution

The basic expression for a line profile resulting from a small crystal [Wilson, 1962] is given by

$$I(2\theta) = (\cos\theta/\lambda)I(k), \tag{3.1}$$

where $I(s)$, the intensity in reciprocal space expressed as a function of the distance $k = 2(\sin\theta - \sin\theta_{\mathrm{Bragg}})/\lambda$, is given by

$$I(k) = U^{-1}\int_{-\tau}^{+\tau} V(t)\cos(2\pi st)\mathrm{d}t, \tag{3.2}$$

where U is the volume of the unit cell. $V(t)$, the Fourier transform of $I(k)$, can conveniently be represented as the volume common to the crystal and its 'ghost' or double, displaced a distance t in the hkl direction. τ is then the value of t for which $V(t)$ becomes zero. $V(t)$ is clearly an even function, since displacements of $+t$ and $-t$ are equivalent, and the line profiles arising from crystallite size are thus always symmetrical, irrespective of the nature of the size distribution. $I(s)$ for crystals having any shape for which $V(t)$ can be expressed as a cubic in t with constant coefficients and continuous derivatives has been derived by Wilson [1962]. This mainly applies to morphologies having cubic symmetry, but $V(t)$, and hence $I(k)$, can readily be calculated for other regular shapes. For example, Langford and Louer [1982] have considered the case of cylindrical crystallites, Vargas et al. [1983] hexagonal prisms, etc. Cylindrical morphology is often a suitable approximation when crystallites are prismatic, acicular, or have the form of platelets. In practice, it is frequently observed that crystallites tend to be approximately equiaxial, such as in powders produced by sol-gel or hydrothermal decomposition, or cubic oxides obtained from solid-state reactions. Such particles can then be regarded as having on average a spherical

morphology. For a spherical crystallite, according to Langford and Wilson [1978]

$$A_S(t;D) \equiv \frac{V(t)}{V(0)} = 1 - \frac{3|t|}{2D} + \frac{|t|^3}{2D^3} \tag{3.3}$$

and the line profile is given by

$$I_S(k;D) \equiv I(k) = \left(\frac{\pi D^4}{2}\right)\left\{\frac{1}{s^2} - \frac{2\sin(s)}{s^3} + \frac{4\sin^2(s/2)}{s^4}\right\}, \tag{3.4}$$

where D is the diameter and $s = 2\pi kD$.

The normalised formula for the peak profile function $f_S(k;D)$ is derived from the Eq. 3.3:

$$f_S(k;D) = \int_{-D}^{D} A_S(t;D)e^{(-2\pi ikt)}\mathrm{d}t = 3D\left\{\frac{1}{s^2} - \frac{2\sin(s)}{s^3} + \frac{4\sin^2(s/2)}{s^4}\right\}. \tag{3.5}$$

It should be noted that the following relations,

$$I_S(k;D) = (\pi D^3/6) f_S(k;D) \tag{3.6}$$

are readily derived from the above equations.

It is assumed that the crystallite size obeys lognormal distribution with the median m and logarithmic standard deviation ω, the density function of which is given by

$$f_{\mathrm{LN}}(D;m,\omega) = \frac{1}{D\omega\sqrt{2\pi}}\exp\left\{-\frac{\ln^2(D/m)}{2\omega^2}\right\}, \tag{3.7}$$

and the cumulative distribution function is

$$F_{\mathrm{LN}}(D;m,\omega) = \frac{1}{2}\,\mathrm{erfc}\left\{-\frac{\ln(D/m)}{\sqrt{2}\omega}\right\}, \tag{3.8}$$

where the function erfc(x) is the complementary error function defined by

$$\mathrm{erfc}(x) \equiv \frac{2}{\sqrt{\pi}}\int_x^{\infty}\exp(-t^2)\mathrm{d}t. \tag{3.9}$$

It should be noted that geometric standard deviation, which is also frequently used in literature, is equal to $\exp(\omega)$.

The properties of the lognormal distribution have been reviewed by Langford et al. [2000]. The jth moment of the distribution is given by

$$\langle D^J \rangle \equiv \int_0^\infty D^j f_{LN}(D; m, \omega) \mathrm{d}D = m^j \exp\left(\frac{j^2\omega^2}{2}\right), \tag{3.10}$$

from which the arithmetic mean is

$$\langle D \rangle = m \exp(0.5\omega^2), \tag{3.11}$$

the variance is

$$\sigma^2 = \langle D \rangle^2 \left[\exp(\omega^2) - 1\right], \tag{3.12}$$

the area-weighted mean is

$$\langle D \rangle_A = \frac{\langle D^3 \rangle}{\langle D^2 \rangle} = m \exp(2.5\omega^2), \tag{3.13}$$

and the volume-weighted mean is

$$\langle D \rangle_V = \frac{\langle D^4 \rangle}{\langle D^3 \rangle} = m \exp(3.5\omega^2). \tag{3.14}$$

The diffraction peak intensity profile from lognormally distributed spherical particles (SLN) is given by

$$I_{\mathrm{SLN}}(k; m, \omega) = \int_0^\infty I_S(k; D) f_{\mathrm{LN}}(D; m, \omega) \mathrm{d}D, \tag{3.15}$$

while the normalised formula is given by

$$f_{\mathrm{SLN}}(k; m, \omega) = \int_0^\infty f_S(k; D) f_{\mathrm{LN}}[D; m \exp(3.5\omega^2), \omega] \mathrm{d}D. \tag{3.16}$$

Although it is difficult to solve the integral in equation (3.16) analytically, the exact solution of the Fourier transform

$$A_{\mathrm{SLN}}(t; m, \omega) \equiv \int_{-\infty}^\infty f_{\mathrm{SLN}}(k; m, \omega) e^{(-2\pi i k t)} \mathrm{d}k \tag{3.17}$$

is available [Ungar et al., 2001]. The solution is

$$\begin{aligned} A_{\mathrm{SLN}}(t;m,\omega) &= (1/2)\,\mathrm{erfc}\{[\ln(|t|/m) - 3\omega^2]/\sqrt{2}\omega\} \\ &\quad -(3|t|/4m)\exp(-2.5\omega^2)\,\mathrm{erfc}\{[\ln(|t|/m) - 2\omega^2]/\sqrt{2}\omega\} \\ &\quad +(|t|^3/4m^3)\exp(-4.5\omega^2)\,\mathrm{erfc}\{[\ln(|t|/m)]/\sqrt{2}\omega\}. \end{aligned} \tag{3.18}$$

Even though the SLN profile is clearly defined by equation (3.16) in integral form, it is not easy to evaluate the integral numerically, especially for large values of ω. Langford et al. [2000] and later Popa and Balzar [2002] have proposed the numerical formulae for evaluation of Eq. (3.16) which are valid just for small values of ω. As it was showed by Ida et al. [2003], the method describe in §4.4.1 can be also used to the evaluation of the SLN function $f_{\mathrm{SLN}}(k;m,\omega)$ with only slight modification, which gives the following equations [Ida et al., 2003]:

$$f_{\mathrm{SLN}}(k;m,\omega) \simeq H_0 \textstyle\sum_{j=1}^{N} w_j g_j / G'_j, \tag{3.19}$$

$$D_0 = m\exp(4\omega^2), \tag{3.20}$$

$$G_0 = (\pi k)^{-1}\arctan(3\pi k D_0/2), \tag{3.21}$$

$$H_0 = 2^{-1}\exp(-0.5\omega^2)G_0, \tag{3.22}$$

$$\xi_j = x_j G_0, \tag{3.23}$$

$$D'_j = (4/3\pi k)\tan(\pi k \xi_j), \tag{3.24}$$

$$D_j = m\exp[4\omega^2 - 2^{1/2}\omega\,\mathrm{erfc}^{-1}(D'_j/D_0)], \tag{3.25}$$

$$g_j = f_S(k;D_j)/D_j, \tag{3.26}$$

$$G'_j = (3/4)[1 + (3\pi k D'_j/4)^2]^{-1}, (i = 1,\ldots,N) \tag{3.27}$$

where $\{x_j\}$ and $\{w_j\}$ are the abscissas and weights of the Gauss-Legendre quadrature.

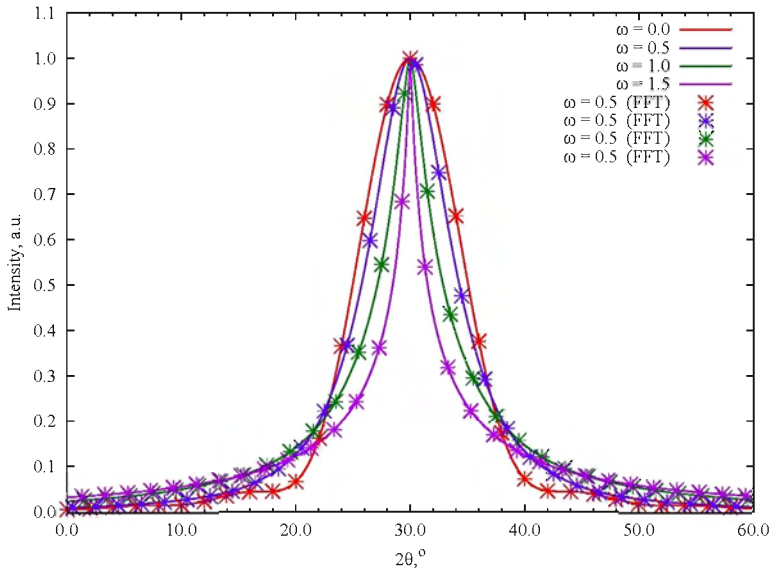

Figure 3.1: The SLN profiles for the median $m = \exp(-3.5\omega^2)(\langle D\rangle_V = 1)$ and the logarithmic standard deviation $\omega = 0, 0.5, 1, 1.5$. Markers denote the values obtained by the Fourier transformation.

The SLN profiles for $\omega = 0, 0.5, 1, 1.5$, calculated by the Eqs. 3.19-3.27 using 16-term numerical integrals, are shown in Fig. 3.1. All of the calculated profiles coincided well with those derived from the inverse Fourier transform of $A_{\mathrm{SLN}}(t; m, \omega)$ calculated by equation (3.18).

3.1.1 Comparison with the Voigt profile

The lognormal distribution for spherical crystallites is characterized by two parameters, the average diameter $\langle D\rangle$ (Eq. (3.11)) of the particles and the dispersion σ^2 (Eq. (3.12)). It is convenient to define the dimensionless ratio [Popa and Balzar, 2002]

$$c = \sigma^2/\langle D\rangle^2 \tag{3.28}$$

The simulated diffraction data, calculating with Eg. (3.19-3.27), for various crystallite size and dispersion were used to find the region where a simple Voigt profile can be used. The Voigt approximation was done using commercial available software TOPAS v2.1.

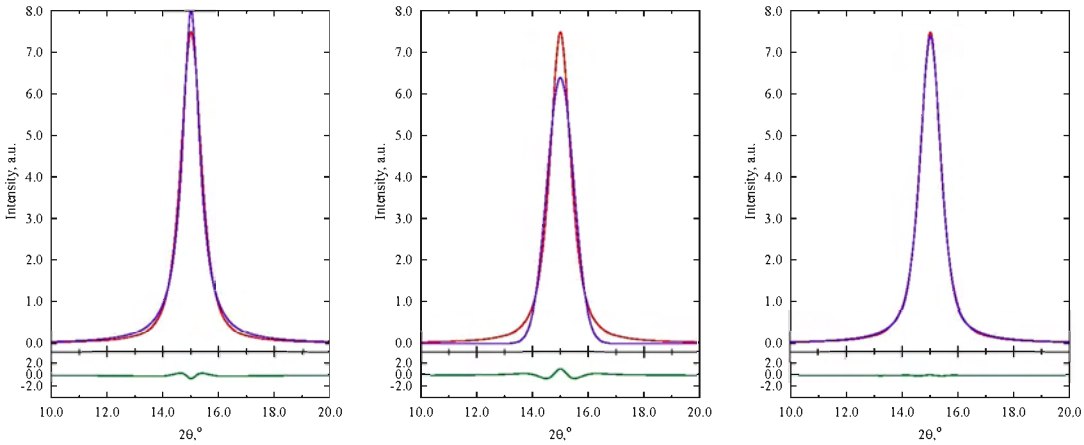

a) Lorentz; GoF=0.08 b) Gauss; GoF=0.17 c) Voigt; GoF=0.02

Figure 3.2: Fitting (blue line of the simulated profile (red line) for spherical crystallites with lognormal size distribution with $\langle D \rangle_V = 10nm$ and $c = 0.2$.

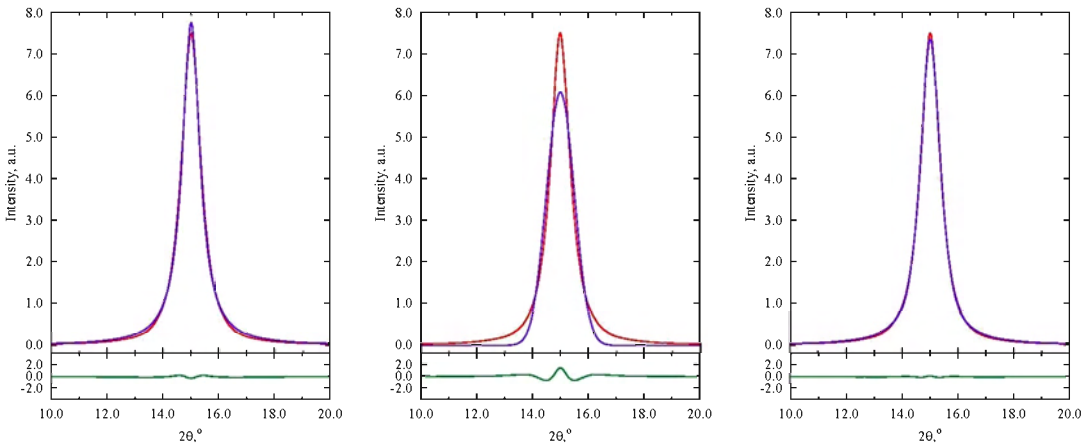

a) Lorentz; GoF=0.05 b) Gauss; GoF=0.19 c) Voigt; GoF=0.02

Figure 3.3: Fitting (blue line) of the simulated profile (red line) for spherical crystallites with lognormal size distribution with $\langle D \rangle_V = 10nm$ and $c = 0.3$.

As can be seen from Figs. 3.2-3.5, the pseudo-Voigt function shows a satisfactory approximation for the size-broadened profile only for $c < 0.4$. For higher value of c, a second Lorentz function must be added [Popa and Balzar, 2002]. Its weight increases with increasing of c. The weight of the Gauss component decreases with increasing

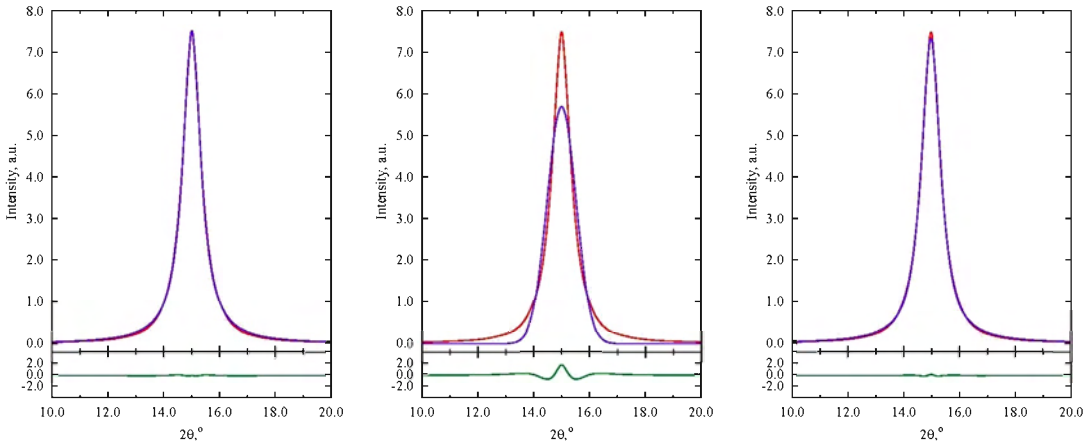

a) Lorentz; GoF=0.03 b) Gauss; GoF=0.22 c) Voigt; GoF=0.02

Figure 3.4: Fitting (blue line) of the simulated profile (red line) for spherical crystallites with lognormal size distribution with $\langle D \rangle_V = 10nm$ and $c = 0.4$.

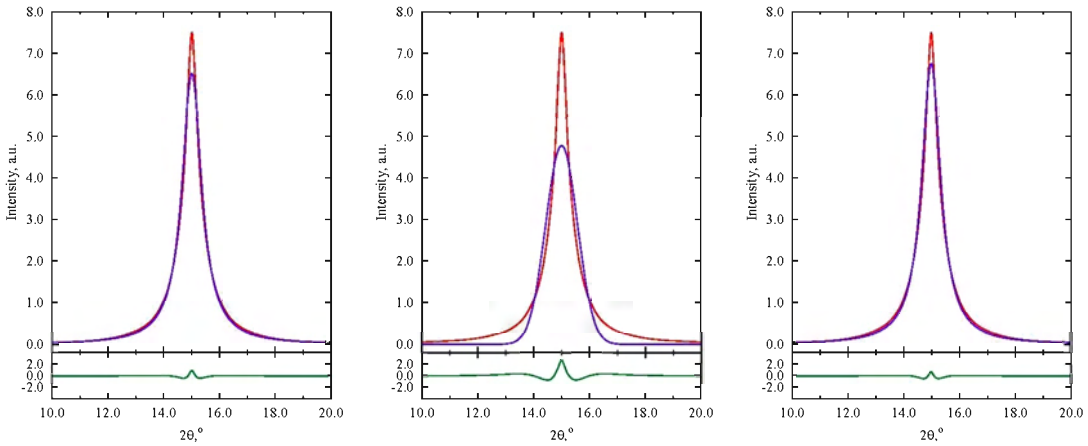

a) Lorentz; GoF=0.07 b) Gauss; GoF=0.3 c) Voigt; GoF=0.06

Figure 3.5: Fitting (blue line) of the simulated profile (red line) for spherical crystallites with lognormal size distribution with $\langle D \rangle_V = 10nm$ and $c = 1.0$.

of c and from approximately $c = 0.3$ it is negligible. It gives the range where Single-line Integral Method (see §2.3.3) can be used. Although Langford et al. [2000] have suggested that the Lorentzian or 'super-Lorentzian' size effect might be attributed to a non-unimodal size distribution, both shapes can be rather naturally explained by the unimodal lognormal size distribution with large logarithmic standard deviation,

as has been concluded by [Popa and Balzar, 2002]. Furthermore, 'super-Lorentzian' [Wertheim et al., 1974] line profiles, which have been reported [e.g. Plevert and Louer, 1990], are also likely to be observed in the case of a broader size distribution (see Fig. 3.5).

3.2 Strain profile function

A Gaussian strain profile function was assumed which should be adequate, according to others [e.g. de Keijser et al., 1982; Delhez et al., 1993; Wu et al., 1998a], for samples with microstrain values in the vicinity of 10 or less. Examples for the adequacy of the use of the Gaussian strain profile were found in CeO_2 powders (ca. $0.33 \cdot 10^{-3}$ - Popa and Balzar [2002]), $\alpha - AI_2O_3$ whisker composites (ca. $0.7 \cdot 10^{-3}$ - Balasingh et al. [1991]) and cold-work nickel, nitrided steel and liquid-quenched AlSi alloy (ca. $2.0 \cdot 10^{-3}$, $1.4 \cdot 10^{-3}$ and $1.3 \cdot 10^{-3}$ respectively - de Keijser et al. [1982]). It is worth noting that the Gaussian strain distribution function describes the configuration of strain probability in the crystal space, while the Gaussian profile function specifies a profile-shape function. The strain profile function takes the form

$$f_{Strain}(\theta) = I_0 \exp\left[-\frac{(2\theta - 2\theta_0)^2}{W_\varepsilon^2}\right] \tag{3.29}$$

where W_ε is the full-width at half maximum intensity and can be associated with the integral breadth for strain β_ε as

$$\beta_\varepsilon = \frac{W_\varepsilon}{\sqrt{\pi}} \tag{3.30}$$

The maximum (upper limit) strain, ε, can be calculated using

$$\beta_\varepsilon = 4\varepsilon \tan\theta_0 \tag{3.31}$$

where θ_0 is the Bragg peak position. For Gaussian strain distribution, the root mean square strain, ε_{rms} , can be determined as [Stokes and Wilson, 1944]

$$\varepsilon_{rms} = \sqrt{\frac{2}{\pi}}\varepsilon \tag{3.32}$$

The overall convolution profile function for both size and strain effects can then be expressed as

$$F(\varepsilon, D, \sigma) = S \cdot f_{SLN} \otimes \exp\left[-\frac{(2\theta - 2\theta_0)^2}{W_\varepsilon^2}\right] \tag{3.33}$$

where S is a scale factor which keeps the area under the profile constant. The calculation of above convolution was done using the technique described in §4.4.1.

Chapter 4

Development of the approximation for instrumental function

In the following chapter a new approach to approximate the total instrumental function based on physical properties of diffractometer is presented. There are no limitations on the size of the source, sample or receiving slit, or the axial or equatorial divergence. The proposed method, valid over a full range of 2θ from 0 to 180^o, can be applied to different diffractometer geometries and can be implemented in different refinement programs.

The line profile in X-ray powder diffraction for a monochromatic beam is determined by sample broadening and instrumental aberration. According to Klug and Alexander [1974], this can be represented as the convolution of a pure diffraction profile f and an instrumental function h (Eq. 1.1).

The following diffractometer factors affect the instrumental function: angular non-uniformity of the intensity distribution, deviation of the flat specimen surface from the focusing circle, axial divergence, specimen transparency and the finite width of the receiving slit. Misalignments of the diffractometer, among them the deviation of the sample plane from its ideal position, will also cause the changes of instrumental. Additional optical elements, such as a crystal monochromator or analyzer, will also influence the instrumental profile. Alexander [1954] supposed that each of these factors can be described by a separate instrumental function and that the total instrumental function can be calculated as a convolution of specific instrumental functions. The instrumental aberration causes three effects: a shift in the peak position, a change in the profile width and an asymmetry of the profile. The influence of the different

instrumental factors on the profile, especially for estimating the shift in the peak position, are considered in detail by Wilson [1963]. According to Klug and Alexander [1974]; Wilson [1963], the axial divergence is the most important contribution to the total instrumental function. The calculation of the axial instrumental function is considered by Cheary and Coelho [1998]; Finger et al. [1994]; Ida [1998a].

The most complete approach based on the convolving of specific instrumental functions is realized in the fundamental parameter approach (FPA) developed by Cheary and Coelho [1998]. Special attention was given to calculate a specific instrumental function caused by axial divergence. The representation of the total instrumental function as a convolution is based on the supposition that specific instrumental functions are completely independent. To compensate for the lack of knowledge about the influence of coupling specific instrumental functions in FPA, it is also necessary to tune the fundamental parameters in order to allow a best fit for the experimental data [Cheary et al., 2004]. The other approach to calculate the total instrumental function is ray tracing, in which the contribution of all possible incident and diffracted rays to the total intensity is numerically treated. This approach, for example, was followed by Bergmann et al. [1998] in the program BGMN. The approaches based on ray tracing are time consuming. Kogan and Kupriyanov [1992] have suggested the calculation of Fourier coefficients for instrumental functions. It was supposed that primary beam intensity, transmission and absorption in the system can be represented as a product of n instrumental functions. This supposition is equivalent to the assumtion that the total instrumental profile can be consider as a convolution of specific instrumental functions. The dimensions of the focus and the receiving slit in the equatorial plane were assumed to be so small that they can be neglected. Honkimaki [1996] suggested a method for the calculation of the instrumental function based on the consideration of

all possible paths in the diffractometer, in which the second order terms in the equatorial axial coupling were taken into account. Recently, Masson et al. [2003] showed that, for highresolution synchrotron powder diffraction, the instrumental function can be represented as a convolution of four specific instrumental functions describing the equatorial intensity distribution, the monochromator and analyzer transfer function, and the axial aberration function.

4.1 The effect of the spectroscopic profile of the K_α emission spectrum of copper

A knowledge of the exact shape of the main lines of X-ray emission spectra and their analytical description is necessary for the detailed evaluation of diffraction experiments. There are some different approaches for explaining the asymmetric line profiles by physical arguments, which are likewise contradictory. The asymmetric shape of emission lines is usually assumed to be due to non-resolved multiplet splitting of the lines. According to Tsutsumi and Nakamori [1973], the $K_{\alpha 1}$ and $K_{\alpha 2}$ lines of the iron group elements and of copper are composed of two component lines due to the splitting of the L_{II} or L_{III} levels, respectively, into two sublevels caused by exchange interactions between the electrons of the incomplete shells. They suggested that both of the components are skewed Lorentzians. An attempt to describe the observed fine structure of the CuK_α spectrum by means of a sophisticated multiplet model was made by Sauder et al. [1977]. They attributed the structure of the spectrum to transitions between double vacancy states. However, this fine structure was not confirmed by other workers [Bremer et al., 1982], that found the spectrum to be smooth. A description assuming five Lorentzians to be superimposed was also given for the more complicated $CuK_{\beta 1,3}$ profile [Bremer and Serum, 1979]. Another approach to the CuK_α spectrum consists in the separation of a symmetrical curve as represented

by the short-wavelength side of each line and taking the difference from the observed intensity distribution as a likewise asymmetric 'satellite line' [Bremer et al., 1982; Parratt, 1959]. The satellite line is assumed to be result from Auger processes [Bremer et al., 1982]. None of the above approaches leads to a simple analytical expression for the CuK_α emission spectrum. A simple description of the asymmetric line profiles by considering them as two half-dispersion (Lorentzian) curves having different half-widths, as proposed by some workers [Finster et al., 1971; Ladell et al., 1959] is not relevant from the physical point of view and not compatible to the observed spectral distributions. In order to obtain a sufficiently simple analytical description of the spectrum, a calculated distribution was fitted to experimental data assuming a doublet model of each K_α line.

The spectrum for the above model may be written as a superposition of four symmetrical component lines, each described by the following dispersion equation (Lorentzian curves [see e.g. Agarwal, 1979]):

$$S(\lambda) = \sum_{j=1}^{4} \frac{Q_j}{1 + \left[\frac{2}{w_j}(\lambda - \lambda_j)\right]^2} \tag{4.1}$$

where λ is the wavelength, λ_j - the peak wavelength of a single line, w_j its half-width and Q_j the relative peak height, j equal 1 and 2 for K_{α_1} and 3 and 4 for K_{α_2} , respectively. The distribution function $S(\lambda)$ is experimentally determined by means of the integrated intensity $R(\theta)$ reflected by the net planes of a single crystal (θ-glancing angle). The wavelength variable is transformed exactly to the θ scale by considering angular dispersion es follows:

$$\frac{2}{w_j}(\lambda - \lambda_j) = \frac{2\lambda_j}{w_j}(\cos x + \sin x \cot \theta_j - 1) \tag{4.2}$$

with $x = \theta - \theta_j$.

All the parameters characterising the spectrum are given in Tab. 4.1. They are based on the values of Bearden [1967] for the K_{α_1} and K_{α_2} lines, which are generally

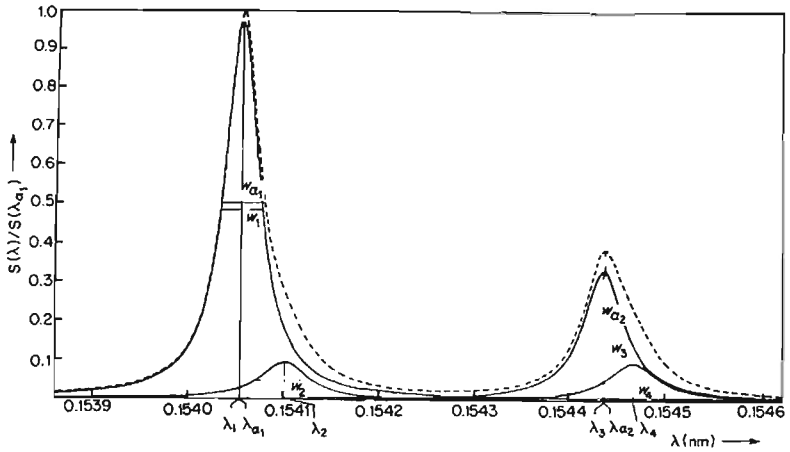

Figure 4.1: X-ray CuK$_\alpha$ emission spectrum as calculated from spectrum parameters (Table 4.1). Full lines, component spectral lines;

Line		Peak intensity ratio, α/α_1	Integrated intensity ratio, I/I_{α_1}	Half-width		Index of asymmetry[9]	Peak wavelength, λ (nm)	Separation between component peaks	
j				w_λ (10^5 nm)	w_E (eV)			$\Delta\lambda$ (10^5 nm)	ΔE (eV)
1	α_{11}	0.970	0.882	4.37	2.28	1	0.1540560	4.62	2.41
2	α_{12}	0.095	0.118	6.0	3.1	1	0.1541022		
3	α_{21}	0.331	0.358	5.20	2.70	1	0.1544374	3.11	1.62
4	α_{22}	0.093	0.120	6.2	3.2	1	0.1544685		
	α_1	1	1	4.61	2.41	1.08	0.1540562[16]		
	α_2	0.382	0.479	6.52	3.39	1.36	0.1544390[16]		

Table 4.1: CuK$_\alpha$ emission spectrum parameters

accepted at present. The X-ray CuK$_\alpha$ emission spectrum as calculated from spectrum parameters (Table 4.1) is presented in Fig 4.1, whereas Fig. 4.7 shows the dependence of the CuK$_\alpha$ spectroscopic profile on the diffraction angle.

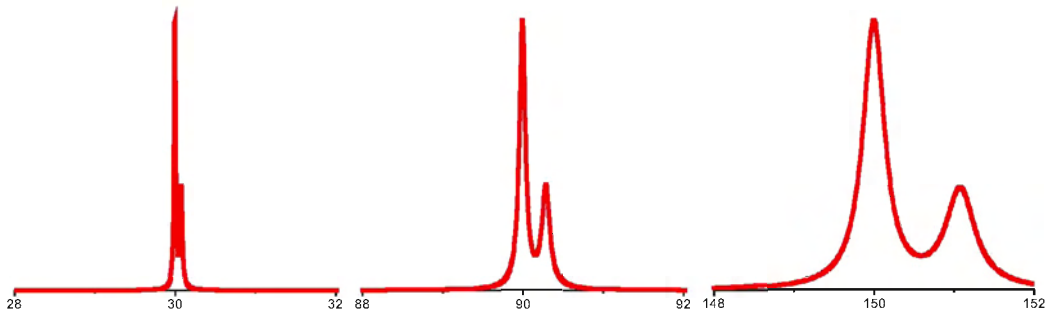

Figure 4.2: The dependence of the CuK$_\alpha$ spectroscopic profile on the diffraction angle.

4.2 Axial divergence effect

The axial divergence aberration is due to divergence of the X-ray beam along the diffractometer axis in the plane of the specimen and is one of the most dominant instrument contributions. In practice, the axial divergence is most readily recognised by the asymmetry that introduces into low angle diffraction lines where the low angle tails extend further than the high angle tails.

In general, a diffractometer will record X-ray counts over a range of measured angles 2θ rather than the true diffraction angle $2\theta_0$. The only rays for which $2\theta = 2\theta_0$ will be those propagating parallel to the equatorial plane and incident on the diffractometer axis. For a particular ray path the measured diffraction angle 2θ for a true diffraction angle $2\theta_0$ depends on the axial divergence α and β in the incident and diffracted rays (see Fig. 4.3).

In Fig. 4.4 the geometry of powder diffractometry including vertical divergence is presented. The diffraction angle $2\theta_0$ for given α and β is exactly related to the horizontal angle 2θ by the following equation:

$$\cos(2\theta_0) = \cos(2\theta)\cos(\alpha)\cos(\beta) + \sin(\alpha)\sin(\beta) \tag{4.3}$$

or

$$2\theta - 2\theta_0 = \arccos(\cos(2\theta_0)\sec(\alpha)\sec(\beta) - \tan(\alpha)\tan(\beta)) - 2\theta_0 \equiv z(\alpha, \beta) \tag{4.4}$$

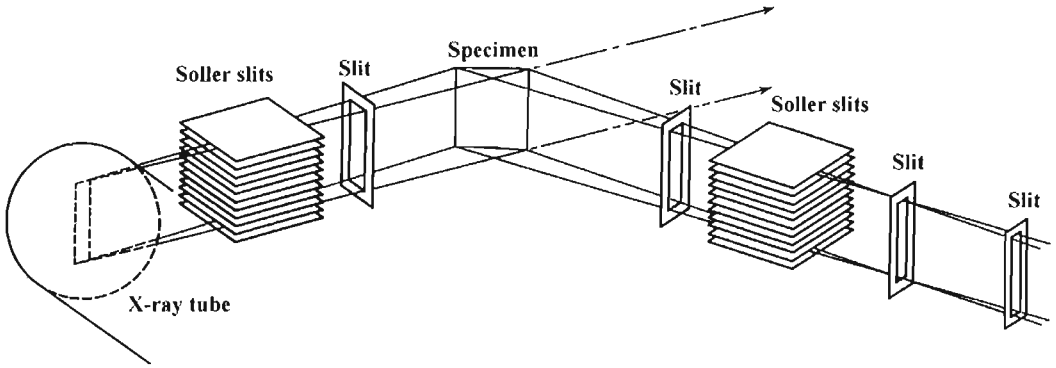

Figure 4.3: Schematic view of a conventional powder diffractometry system with double Soller slit geometry

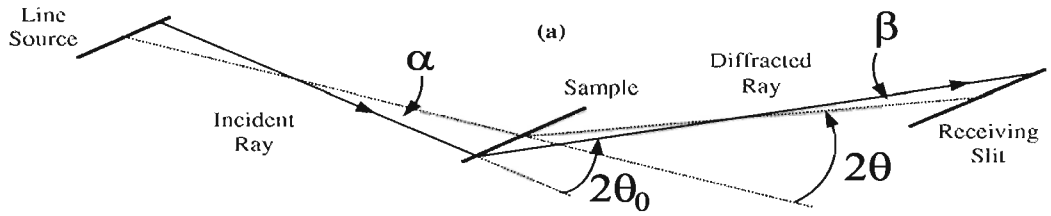

Figure 4.4: Geometry of powder diffractometry including vertical divergence. The overall diffraction angle and its horizontal component are denoted by $2\theta_0$ and 2θ; α and β are the angles of the deviations of the incident and scattered beams from the horizontal plane.

the function $z(\alpha, \beta)$ can be approximated by

$$z(\alpha, \beta) \cong -\frac{\alpha^2 + \beta^2}{2} \cot(2\theta_0) + \alpha\beta \mathrm{cosec}(2\theta_0), \tag{4.5}$$

on the assumption that α and β are sufficiently small. By changing the variables (α, β) to (x,y) by $\alpha \equiv (x + y)/\sqrt{2}$ and $\beta \equiv (x - y)/\sqrt{2}$, the above relation can be simplified as [Ida, 1998a]

$$z \cong -\frac{1}{2}(x^2 t - y^2/t), \tag{4.6}$$

where $t \equiv \tan(\theta_0)$. Assuming that the vertical window profiles of the incident and

scattered beams to be $f_{\mathrm{V1}}(\alpha)$ and $f_{\mathrm{V2}}(\beta)$, and the horizontal profile to be $f_H(2\Theta-2\theta)$, where 2Θ is the horizontal angle which defines the position of the receiving slit or the detector. When we define $\Delta 2\theta \equiv 2\Theta - 2\theta_0$, the convoluted profile function $P(\Delta 2\theta)$ has a general form of

$$P(\Delta 2\theta) = \int\int\int f_{\mathrm{H}}(2\Theta - 2\theta) f_{\mathrm{V1}}(\alpha) f_{\mathrm{V2}}(\beta)\delta(2\theta - 2\theta_0 - z)d\alpha d\beta d(2\theta), \tag{4.7}$$

where $\delta(x)$ is the Dirac delta function. The integration of Eq. 4.7 on 2θ gives

$$P(\Delta 2\theta) = \int\int f_{\mathrm{H}}(\Delta 2\theta - z) f_{\mathrm{V1}}(\alpha) f_{\mathrm{V2}}(\beta)d\alpha d\beta. \tag{4.8}$$

When we compare the above formula with the following standard form of convolution:

$$P(\Delta 2\theta) = \int f_{\mathrm{H}}(\Delta 2\theta - z)w(z)dz, \tag{4.9}$$

where $w(z)$ is the window function to be convoluted to the original profile function $f_{\mathrm{H}}(z), w(z)$ is found to be given by the following integration:

$$w(z) = \int f_{\mathrm{V1}}(\alpha) f_{\mathrm{V2}}(\beta)\frac{d\beta}{dz}d\alpha, \tag{4.10}$$

or alternatively,

$$w(z) = \int f_{\mathrm{V1}}\left(\frac{x+y}{\sqrt{2}}\right) f_{\mathrm{V2}}\left(\frac{x-y}{\sqrt{2}}\right)\frac{dy}{dz}dx. \tag{4.11}$$

If the Soller slits are ideally designed and the beam source or the detector have sufficient length in the vertical direction, the vertical window functions should have the profile of a triangle as illustrated in Fig. 4.5, which is known as a Bartlett window in the field of time series analysis. The normalised Bartlett window function $f_{\mathrm{B}}(\varphi)$ with the full width at half maximum (FWHM) of Φ_{B} is given by

$$f_{\mathrm{B}}(\varphi) = \frac{1}{\Phi_{\mathrm{B}}}(1 - \frac{|\varphi|}{\Phi_{\mathrm{B}}})\mathrm{for}|\varphi| < \Phi_{\mathrm{B}}, \tag{4.12}$$

and $f_{\mathrm{B}}(\varphi) = 0$, elsewhere. Usually the Soller slits for the incident and scattered beams have symmetric geometry, that is,

$$f_{\mathrm{V1}}(\varphi) = f_{\mathrm{V2}}(\varphi) = f_{\mathrm{B}}(\varphi). \tag{4.13}$$

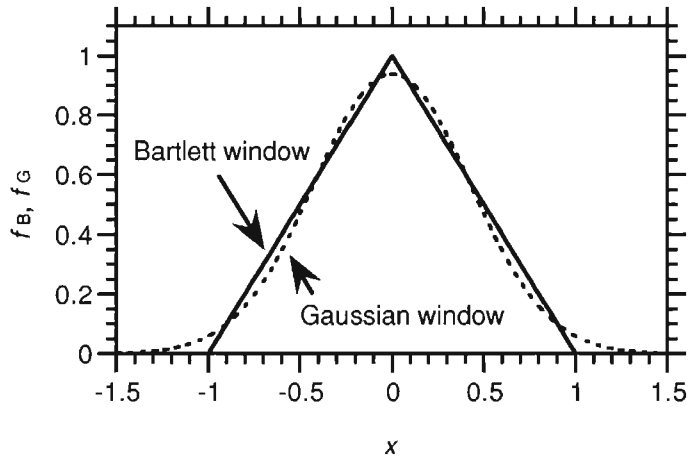

Figure 4.5: Profiles of normalized Bartlett and Gaussian window functions with FWHM (Φ_B, Φ_G) of 1

As it was proposed by Ida [1998a] the double vertical Bartlett windows can be approximated by vertical Gaussian windows (Fig. 4.5), the analytical solution of which is easier owing to the infinite integral range. Furthermore, a model based on Gaussian windows will be appropriate, if the real Soller slits have random error in geometry. The normalized Gaussian window function $f_G(\varphi)$ with the FWHM of Φ_G is given by

$$f_G(\varphi) = \frac{2\sqrt{\ln 2}}{\sqrt{\pi}\Phi_G} \exp\left[-4(\ln 2)\frac{\varphi^2}{\Phi_G^2}\right] \tag{4.14}$$

or

$$f_G(\varphi) = \frac{1}{\sqrt{\pi}\Psi_G} \exp\left[-\frac{\varphi^2}{\Psi_G^2}\right], \tag{4.15}$$

where

$$\Psi_G \equiv \frac{\Phi_G}{2\sqrt{\ln 2}}. \tag{4.16}$$

When the Soller slits for the incident and scattered beams have symmetric geometry again,

$$f_{V1}(\varphi) = f_{V2}(\varphi) = f_G(\varphi). \tag{4.17}$$

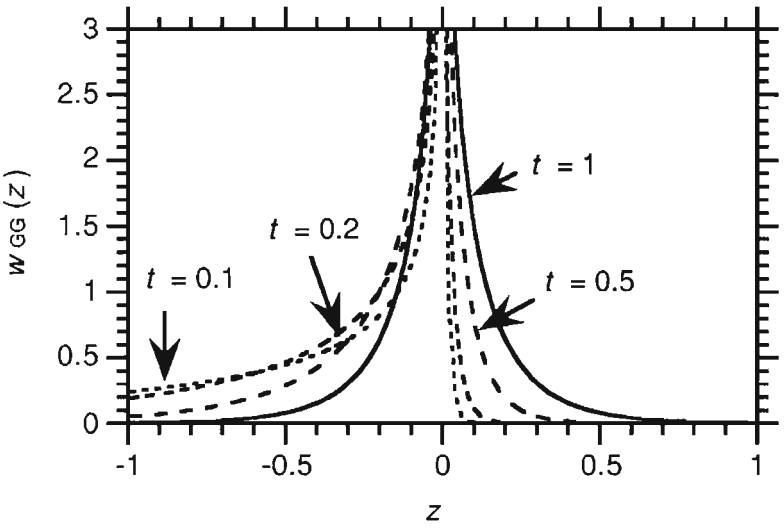

Figure 4.6: Horizontal window function w_{GG} mapped from symmetric double vertical Gaussian window functions with the FWHM $\Phi_{\mathrm{G}} = 1$ for various t ($= \tan\theta_0$) values [Ida, 1998a].

The horizontal window function w_{GG} has a much more simple analytical form than horizontal window function w_{BB} derived from Barlett window , that is [Ida, 1998a],

$$w_{\mathrm{GG}} = \frac{2}{\pi\Psi_{\mathrm{G}}^2} \exp\left[\frac{t^2-1}{t}\frac{Z}{\Psi_{\mathrm{G}}^2}\right] \mathrm{K}_0\left(\frac{t^2+1}{t}\frac{|z|}{\Psi_{\mathrm{G}}^2}\right), \tag{4.18}$$

where $\mathrm{K}_0(x)$ is the modified Bessel function of the second kind. Fig. 4.6 plots the profiles of the $w_{\mathrm{GG}}(z)$ function for various t values. The profile of $w_{\mathrm{GG}}(z)$ is found to be quite similar to that of $w_{\mathrm{BB}}(z)$ [Ida, 1998a].

Fig. 4.7 shows the dependence of the axial divergence aberration functions on the diffraction angle.

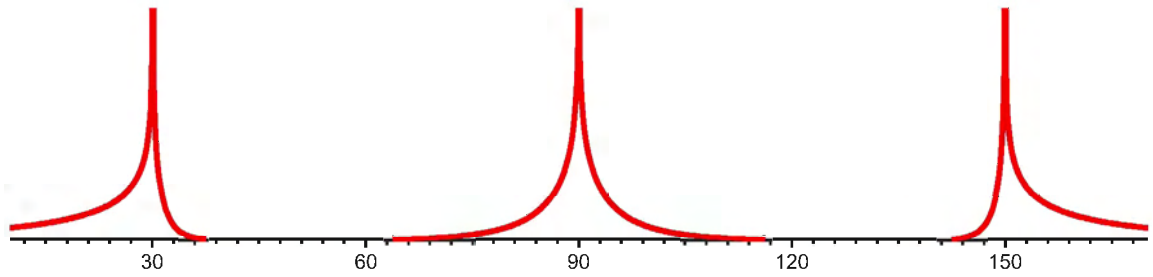

Figure 4.7: The dependence of the axial divergence aberration functions on the diffraction angle for the axial divergence angle $\Phi_G = 5$.

4.3 Flat-specimen effect

The basic optics of the focussing powder diffractometer set up for symmetric diffraction is illustrated in Fig. 4.8. The X-rays are incident at an angle θ on an ideal polycrystalline specimen with a surface radius of curvature ρ. For diffraction from a particular *hkl* plane the common property of all the diffracted rays from the specimen is that they all deviate through the same angle 2θ. By simple geometry it can be shown that all the diffracted rays converge to a focus on a circle which has the same curvature as the specimen surface. The focus of the diffracted rays defines the position of the receiving slit. In commercial diffractometers the specimen is invariably flat and the diffracted beam no longer perfectly focusses.

Fig. 4.9 illustrates the relation of the diffraction angle 2θ and the goniometer angle 2Θ, when the incident X-ray beam deviates from the centre of the flat specimen by the angle φ. The above three angles are mutually related by the following equation:

$$2\cot\Theta = \cot(\Theta + \varphi) + \cot(2\theta - \Theta - \varphi). \tag{4.19}$$

Therefore, when we define $y \equiv 2\Theta - 2\theta$, y is given by

$$y = \Theta - \varphi - \operatorname{arccot}\left[2\cot\Theta - \cot(\Theta + \varphi)\right], \tag{4.20}$$

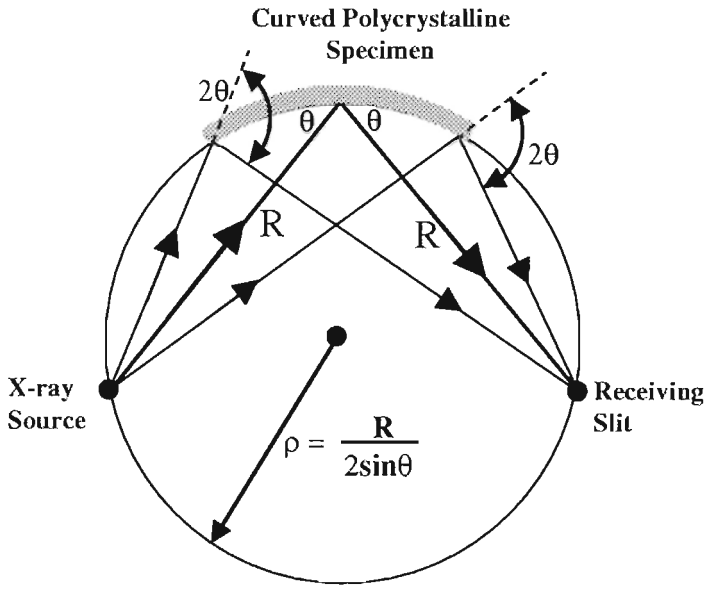

Figure 4.8: Focussing in a symmetric powder diffractometer [Cheary et al., 2004].

or approximately [Ida and Kimura, 1999b],

$$y \approx -2\varphi^2 \cot\Theta, \tag{4.21}$$

for sufficiently small φ.

When we assume that the peak profile function for the $\varphi \to 0$ limit is expressed by $f_0(2\theta - 2\theta_0)$, where $2\theta_0$ is the Bragg angle and φ varies from $-\Phi_H/2$ to $\Phi_H/2$, that is, the horizontal divergence angle is defined by Φ_H, the asymmetrised peak profile is given by

$$p(\Delta 2\theta) = (1/\Phi_H) \int_{-\Phi_H/2}^{\Phi_H/2} f_0(\Delta 2\theta - y)\mathrm{d}\varphi, \tag{4.22}$$

where $\Delta 2\theta \equiv 2\Theta - 2\theta_0$. The approximated form of (4.22) is given by

$$p(\Delta 2\theta) \approx \frac{1}{2(\gamma_H)^{1/2}} \int_{-\gamma_H}^{0} f_0(\Delta 2\theta - y)|y|^{-1/2}\mathrm{d}y, \tag{4.23}$$

where

$$\gamma_H \equiv \frac{\Phi_H^2}{2} \cot\Theta. \tag{4.24}$$

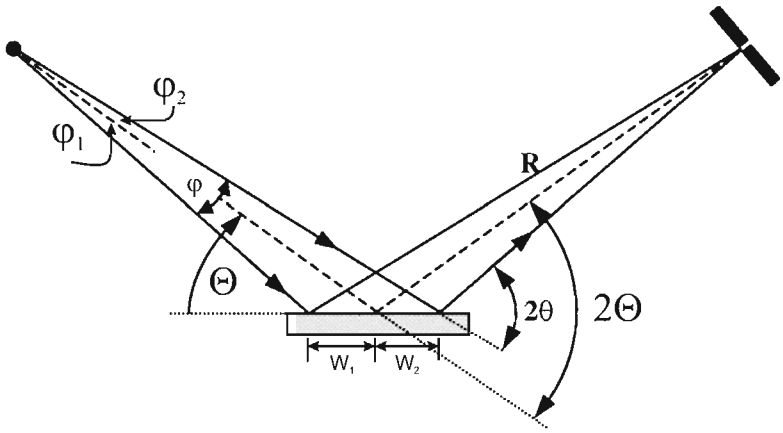

Figure 4.9: Diffraction from a flat plate showing the relationship between the measured angle 2Θ on the diffractometer and the diffraction angle 2θ for a ray at the outer limit of a beam of divergence φ.

As it was proposed by Ida and Kimura [1999a], if we compare the above formula with the standard form of convolution,

$$p(\Delta 2\theta) = \int f_0(\Delta 2\theta - y) w_H(y) \mathrm{d}y, \tag{4.25}$$

where $w_H(y)$ is the window function to be convoluted, the asymmetric window function for the flat-specimen effect $w_H(y)$ is found to be given by

$$w_H(y) = \begin{cases} |y|^{-1/2} \dfrac{1}{2(\gamma_H)^{1/2}} & \text{for } -\gamma_H < y < 0 \\ 0 & \text{elsewhere} \end{cases}. \tag{4.26}$$

Limitation of the horizontal divergence by the sample width

Although the horizontal divergence angle Φ_H is primarily determined by the open angle of divergence/scattering slits ($\Phi_{\mathrm{DS/SS}}$), the effective angle is limited when the sample size is not sufficient for covering the irradiated area. Fig. 4.9 illustrates briefly the relation of the limits of the horizontal divergence and the sample width. The horizontal deviation angles φ_1 and φ_2 and the sample widths W_1 and W_2 are

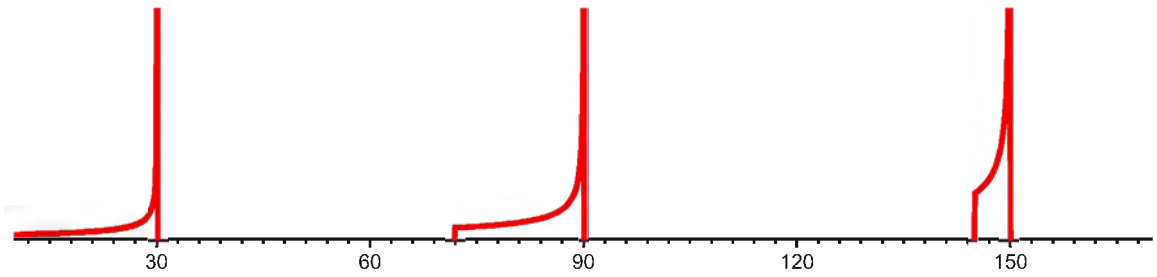

Figure 4.10: The dependence of the flat-specimen aberration function on the diffraction angle.

exactly related by the following equations:

$$\varphi_1 = -\Theta + \arctan \frac{\sin\Theta}{\cos\Theta - \dfrac{W_1}{R}}, \tag{4.27}$$

$$\varphi_2 = \Theta - \arctan \frac{\sin\Theta}{\cos\Theta + \dfrac{W_2}{R}}. \tag{4.28}$$

When $W_1 = W_2 = W$, the effective horizontal divergence angle $\Phi_{H,\text{eff}}$ is approximately given by

$$\Phi_{H,\text{eff}} \simeq \varphi_1 + \varphi_2 = \frac{\arctan\left(2\dfrac{W}{R}\right)\sin\Theta}{1 - \left(\dfrac{W}{R}\right)^2}, \tag{4.29}$$

where R is the goniometer radius. If $\Phi_{\text{DS/SS}}$ is larger than $\Phi_{H,\text{eff}}$, Φ_H should be determined by $\Phi_{H,\text{eff}}$ instead of $\Phi_{\text{DS/SS}}$, and the intensity of reflection should be multiplied by $\Phi_{H,\text{eff}}/\Phi_{\text{DS/SS}}$.

The dependence of the profile of $w_H(y)$ on the diffraction angle is shown in Fig. 4.10.

4.4 Instrumental function as convolution

The symmetrical part of the instrumental aberration can be described by a Voigt function Thompson et al. [1987]. The shift of diffraction peaks and their asymmetry

are mainly caused by following effects: Spectroscopic profile of CuK_α radiations, axial divergence and flat specimen aberrations.

As it was assumed in the beginning of this chapter the instrumental function is the convolution of the four above mentioned effects and can be described as:

$$h = w_x \otimes w_H \otimes w_V \otimes w_{GL} \tag{4.30}$$

where w_{GL} is the symmetric feature of the profile function given by pseudo-Voigt function [Thompson et al., 1987], w_x represent the effect of CuK_α emission spectrum, w_H the horizontal aberration effect (flat-specimen effect) and finally w_V the vertical aberration effect. The analytical solution is available only for the Lorenz component of pseudo-Voigt function with w_H. Therefore an efficient method to calculate the convolution is necessary.

4.4.1 An efficient method for numerical calculation of convolution

An efficient method for the numerical integration of the convolution was proposed by Ida [1998b]; Ida and Kimura [1999b]. The method is applicable to any kind of aberration functions and the basic idea of this method is to substitute the variable y of the integral

$$I = \int_a^b f(x-y)w(y)\mathrm{d}y \tag{4.31}$$

by the following equation:

$$\begin{aligned} \xi &\equiv W\left[\frac{F(x)-F(x-y)}{F(x)-F(x_0)}(x-x_0)\right] \\ \Longleftrightarrow y &\equiv x - F^{-1}\left[F(x) - \frac{F(x)-F(x_0)}{x-x_0}W^{-1}(\xi)\right], \end{aligned} \tag{4.32}$$

where we assume that the peak of $f(x)$ is located at $x \simeq x_0$ and the primitive functions of $f(x)$ and $w(y)$ are approximated by $F(x)$ and $W(y)$, respectively. Then

the approximate formula based on numerical integration is given by

$$I \approx (\beta - \alpha)\frac{F(x) - F(x_0)}{x - x_0} \times \sum_{i=1}^{N} \frac{w_i f(x - y_i) w(y_i)}{F'(x - y_i) W[W^{-1}(\xi_i)]}, \tag{4.33}$$

where we define

$$y_i \equiv x - F^{-1}[F(x) - \frac{F(x) - F(x_0)}{x - x_0} W^{-1}(\xi_i)], \tag{4.34}$$

$$\xi_i \equiv \alpha + (\beta - \alpha)x_i, \tag{4.35}$$

$$\alpha \equiv W[\frac{F(x) - F(x - a)}{F(x) - F(x_0)}(x - x_0)] \tag{4.36}$$

$$\beta \equiv W[\frac{F(x) - F(x - b)}{F(x) - F(x_0)}(x - x_0)], \tag{4.37}$$

and x_i and w_i are the Gauss-Legendre abscissae and weights associated with the ith point [Press et al., 1986].

4.4.2 Non-linear Least-squares Optimization

In the least-square procedure, a model is presumed to be optimal when the sum S of the squares of the differences between the measured and the calculated patterns are as amall as possible, that is when

$$S = \sum w_m (y_{o,m} - y_{c,m})^2 \tag{4.38}$$

reaches a minimum. Here, $y_{o,m}$, is the observed step intensity, $y_{c,m}$ is the corresponding calculated value, and w_m is the weighting factor for point m in the pattern which is normally set as the reciprocal of the variance of the measured intensity at point m, i.e. $w_m = \frac{1}{\sigma^2}$. The calculated intensity is given by summing the contributions from neighbouring Bragg reflections and background bkg_m.

The non-linear least-squares refinement C++ code has been written for profile fitting, using equation (4.30), based on the standard algorithm given by Marquardt,

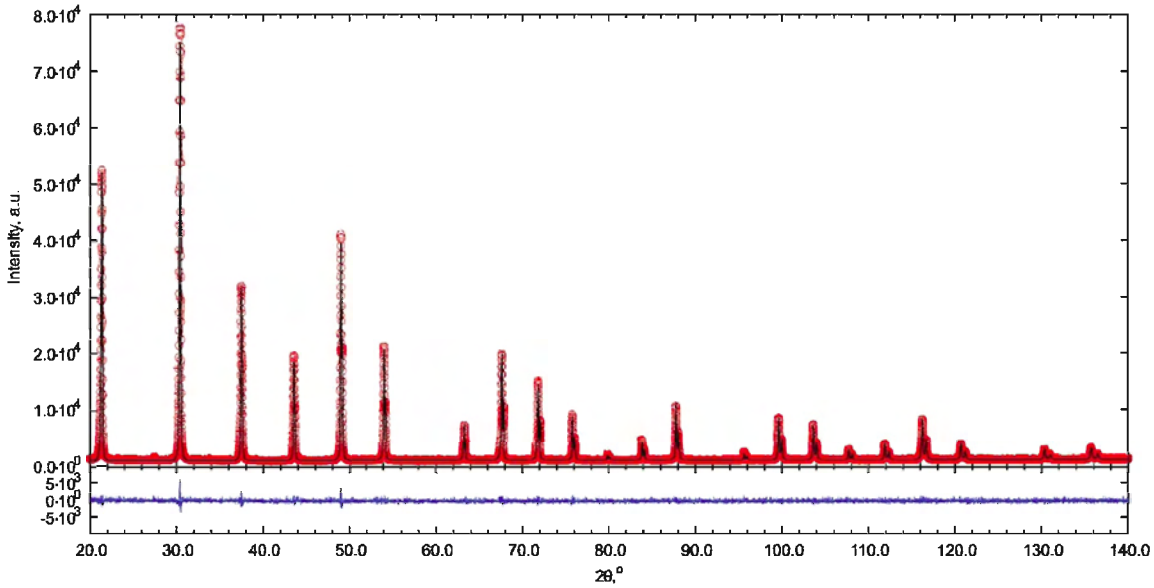

Figure 4.11: Agreement between calculated and measured XRD patterns fot the LaB_6 SRM660a standard samples. The observed data are indicated by red circle and the calculated profile the continuous black line in the same field. The lower plot is the difference between the calculated and measured patterns.

which is also known as the Marquardt or Levenberg-Marquardt method [Marquardt 1963; Press et al. 1989].

Refinement quality is assessed using the difference plot and the Criteria of Fit (CoF). The difference plots were used to compare the agreement between calculated and measured patterns. For example, Fig. 4.11 shows the agreement between calculated and measured XRD patterns for the LaB_6 SRM660a standard samples. The Criteria of Fit comprises

- profile R-factor, R_p

$$R_p = \sqrt{\frac{\sum |y_{o,m} - y_{c,m}|}{\sum |y_{o,m} - bkg_m|}} \tag{4.39}$$

- weighted profile R-factor, R_{wp}

$$R_{wp} = \sqrt{\frac{\sum w_m (y_{o,m} - y_{c,m})^2}{\sum w_m (y_{o,m} - bkg_m)^2}} \tag{4.40}$$

- R-expected, R_{exp}

$$R_{\exp} = \sqrt{\frac{\sum M - P}{\sum w_m (y_{o,m} - bkg_m)^2}} \tag{4.41}$$

where M - the number of data points and P - the number of parameters

- "Goodness of fit" (GoF) index, GOF

$$GoF = \frac{R_{wp}}{R_{\exp}} = \sqrt{\frac{\sum w_m (y_{o,m} - y_{c,m})^2}{M - P}} \tag{4.42}$$

- Bragg R-factor, R_B

$$R_B = \frac{\sum |I_{o,k} - I_{c,k}|}{\sum I_{o,k}} \tag{4.43}$$

4.5 Experimental proof of the proposed model for instrumental function

The quality of the proposed model for instrumental function approximation was tested by least squares fitting of experimental data sets resulting from the reference materials LaB_6 (NIST SRM660a), Al_2O_3 and SiO_2, respectively. A Siemens D5000 X-ray diffractometer with CuK_α radiation tube as the X-ray source was used in this study.

In Figs. 4.12 and 4.13 the fit of selected peaks for LaB_6 and Al_2O_3 standard samples are shown. The observed asymmetry of the peak is well reproduced by the model functions. It would be unrealistic to expect the refined parameters for a diffractometer to match the directly measured values exactly as there are a number of second-order effects in diffractometer profiles that are not incorporated in the fitting model. Moreover, not all of the instrumental aberrations are independent and such a convolutional model is not strictly valid for a certain combinations of aberrations [Cheary and Coelho, 1992]. Nevertheless, the differences in the parameters for the instrumental function obtained by LaB_6 and Al_2O_3 (see Table 4.2) do not exceed 10%. It was observed that when deliberate changes were made to the diffractometer set-up, such as changing the receiving slit width, the change in the refined instrument values corresponded well to the actual changes.

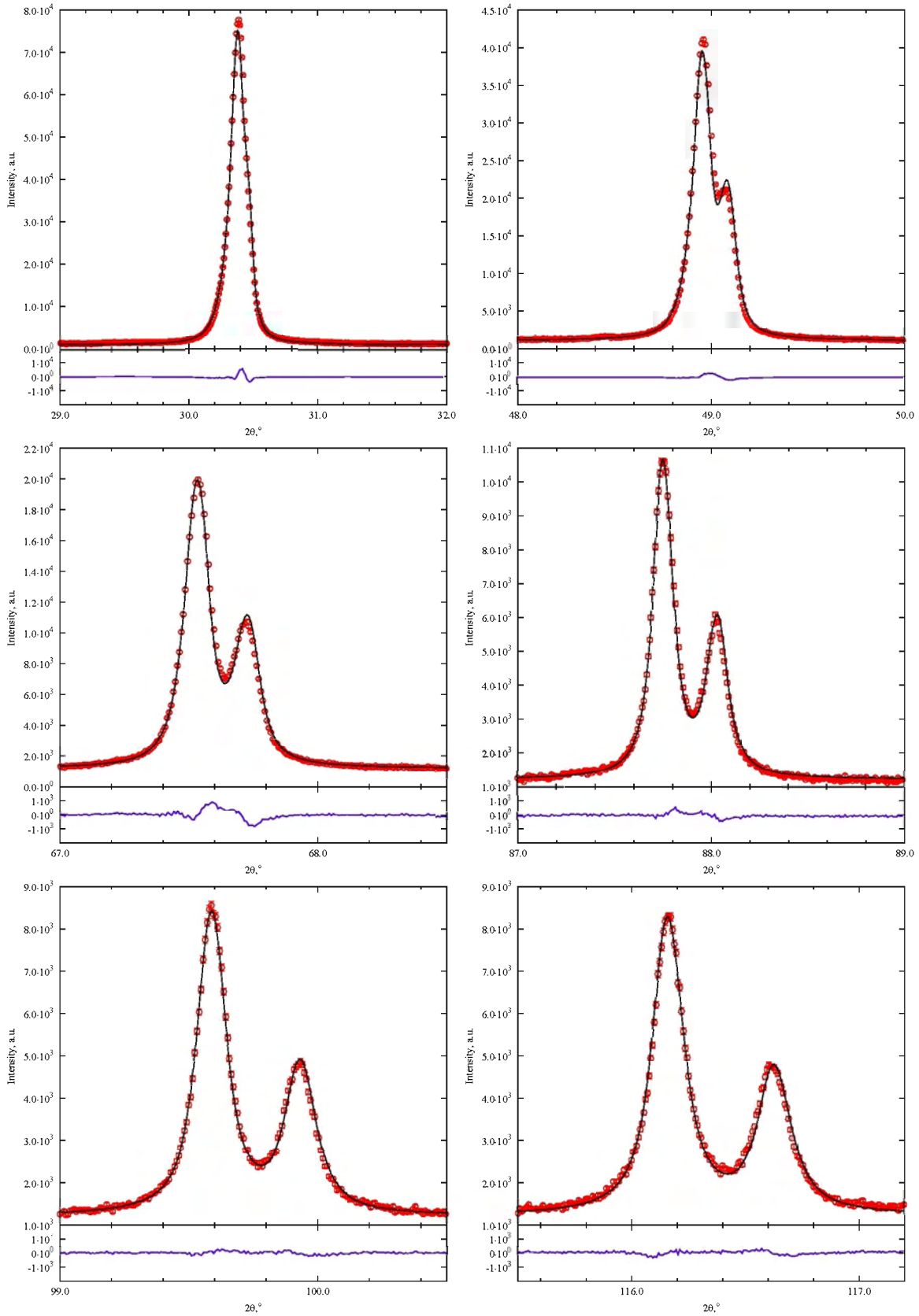

Figure 4.12: Results of fitting 110, 210, 300, 321, 410 and 421 profiles from LaB_6 with the parameters shown in Table 4.2. $GoF = 2.1$. Red circles represent observed profile and black line - fitting profile.

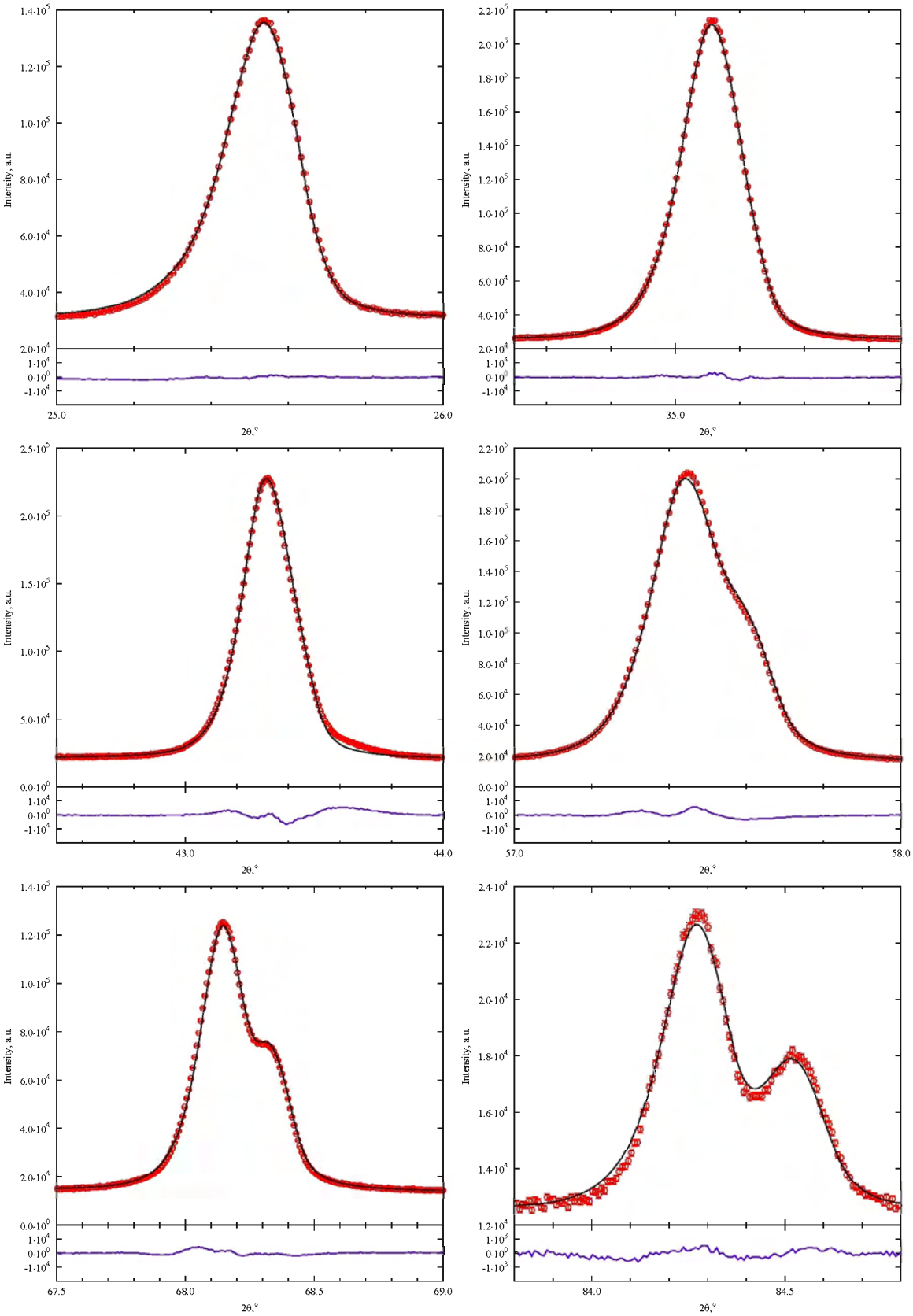

Figure 4.13: Results of fitting 012, 104, 113, 116, 300 and 223 profiles from Al_2O_3 (corundum) with the parameters shown in Table 4.2. $GoF = 3.2$ Red circles represent the observed profile and black line - fitting profile.

Table 4.2: Fitting parameters for LaB_6 and Al_2O_3 diffraction data based on Eq. (4.30)

	LaB_6	Al_2O_3
$w_G,^o$	$3.5 \cdot 10^{-2}$	$4.1 \cdot 10^{-2}$
$w_L,^o$	$5.46 \cdot 10^{-2}$	$4.8 \cdot 10^{-2}$
$\Phi_V,^o$	2.23	2.33
$\Phi_H,^o$	1.34	1.21

The established instrumental parameters describe specific configuration of diffractometer if they are in a good agreement with their actual values. Therefore they can be used as fixed parameters in the further fitting routine for different samples.

The quality of fitting a SiO_2 profile using the previously defined parameters are shown in Fig. 4.14. As parameters for the instrumental function the average values from Tab. 4.2 were used. Again, no significant error was found in the fit. Hence, the proposed model is in practice a useful compromise between accuracy and numerical effort.

The proposed approximation for instrumental function offers a number of benefits in comparison with empirical methods based on splitting Voigt or Pearson VII functions approximations (see §2.1). The application based on a physical model of the diffractometer and its refined parameters should be self consistent with physical dimensions of the diffractometer. On this basis it can therefore identify whether or not a diffractometer operates at optimum resolution for the conditions used and provides a means for assessing the performance of a diffractometer in a particular application. The number of parameters which are necessary for successfully description of the instrumental function are dramatically decreased (from 18 in the case of split Pearson VII function (see §2.1) down to 4 parameters) which made the fitting routine more stable and instrumental function more reproducible from sample to sample.

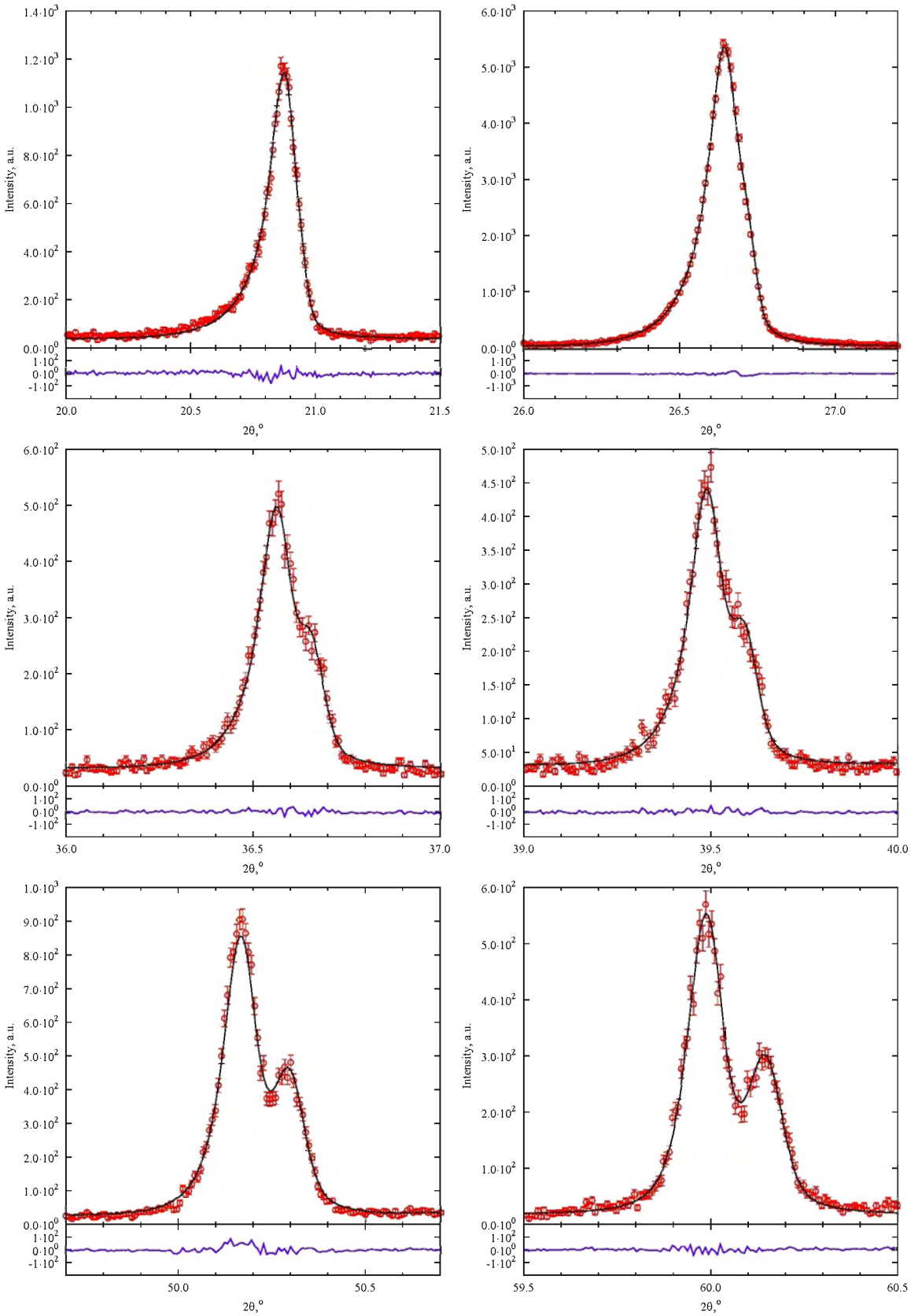

Figure 4.14: Results of fitting 100, 101, 110, 102, 112 and 211 profiles from SiO_2 with the instrumental parameters defined by other standards samples. $GoF = 1.7$ Red circles represent the observed profile and black line - fitting profile.

4.6 Deconvolution of the instrumental aberrations from powder X-ray diffraction data based on a Fourier method

It has been well recognised that experimental X-ray diffraction profiles are convolutions of the incident X-ray spectral distribution, the various instrumental aberrations and the intrinsic diffraction pattern of the powder or polycrystalline sample [Ladell et al., 1959]. A variety of methods have been proposed for the elimination of instrumental broadening, including that caused by the $\alpha_1 - \alpha_2$ doublet [Rachinger, 1948; Stokes, 1948; Keating, 1959; Gangulee, 1970; Ladell et al., 1975]. However, none of these methods can be used to eliminate the instrumental aberrations from the entire observed diffraction pattern in a one-step operation. The other methods restrict the solution of this problem to a small part of the pattern (a single diffraction line). It is impossible to deconvolute all of the instrumental effects from an entire diffraction pattern by a standard Fourier method, because the profile of the instrumental function for powder diffractometry is varied in a complex manner depending on the diffraction angle 2θ. No significant improvement has been achieved in Fourier-based methods for the elimination of the instrumental aberration from experimental peak profiles, after the pioneering work of Stokes [1948] except the following application.

One of the best Fourier based approaches to deconvolute the instrumental aberration functions from the experimental powder X-ray data has been proposed by Ida and Toraya [2002]. This method is based on the combination of scale transformation, interpolation of data and fast Fourier transformation. In this method the effects of axial divergence, flat specimen, sample transparency and spectroscopic profile of the source X-ray are eliminated from the entire observed diffraction pattern in the next steps:

- The elimination of $K\alpha_2$ and the higher-angle component of the axial divergence aberration on the $\ln(\sin\theta)$ scale.

- The elimination of the lower-angle component of the axial divergence aberration and flat-specimen aberration on the $-\ln(\sin\theta)$ scale.

- The elimination of the aberration caused by the sample transparency on the $\breve{}\ln[(1+\cos 2\theta)/(1-\cos 2\theta)]$ scale.

- The elimination of symmetric feature of the profile function.

It is well-known, that the Fourier based deconvolution always exaggerates the noise in the source data. To suppress the unwanted increase of the noisy structure Gaussian filtering of the signal was performed after each deconvolution step. It is obvious that this smoothing process introduces an additional error in the deconvoluted signal, but it is impossible to avoid this additional filtering, as otherwise, any Fourier based method will be even not stable against numerical noise introduced by limited accuracy of calculation.

The simulation of an instrument-broadened X-ray profile was carried out to investigate the properties and stability of this method. The simulations include the generation of an observed profile from the convolution of an instrumental and specimen profile. The instrument profile was assumed to be as described in §4.4 and the experimentally defined parameters from §4.5 were used. The instrument profile function was normalised according to Eq. (5.2). The simulated pattern for nanostructured gold with the median $m = 20nm$ and the logarithmic standard deviation $\omega = 0.3$ according to Eg. (3.33) was used as the specimen profile. Both profiles were calculated over the interval of $30.0^o - 90.0^o$. The small constant background was added to simulate the effect of the misfitting error of the background level. Additionally, Gaussian noise, calculated by standard technique was added to the convoluted result. Its negative value was not restricted despite of strictly positive value of registered signals. In fact, negative values can arise after background removing procedure.

The normalised specimen and instrumental profiles, as well as the simulated observed profile for different noise level are given in Figs. 4.15, 4.16 (Top).

It is easy to see (Fig. 4.15) that in spite of additional smoothing procedure the Fourier based deconvolution still causes dramatically increase of noise in the deconvoluted profile. Even with relative small instrumental noise ($\sim 10\%$) this technique became absolutely not stable (see Fig. 4.16). Therefore for the successfull application of this method to the real experimental data they have to be fitted first with some empirical functions (like split Pearson, split Voigt and etc.) and then a Fourier based deconvolution can be applied. But this fitting procedure will suppress or at least distort information about peak shape. As it was shown in Chapter 3 the information about specimen properties like size and strain distributions is hidden not just in FWHM but also in peak shape. Therefore, applying this additional fitting routine, it will be impossible to retrieve this information after the deconvolution. Additional disadvantage of the above described technique is its dependence on the concrete analytical form of the approximation of the instrumental function. Hence, the introduction of additional effects to describe the instrumental function requires an additional deconvolutional step and scale transformations that will decrease the stability of this procedure even more.

Therefore the development of new deconvolution technique which should be fast, independent of concrete analytical form of the instrumental function and more reliable in terms of stability, especially in the case of large non neglectable experimental noise, is required.

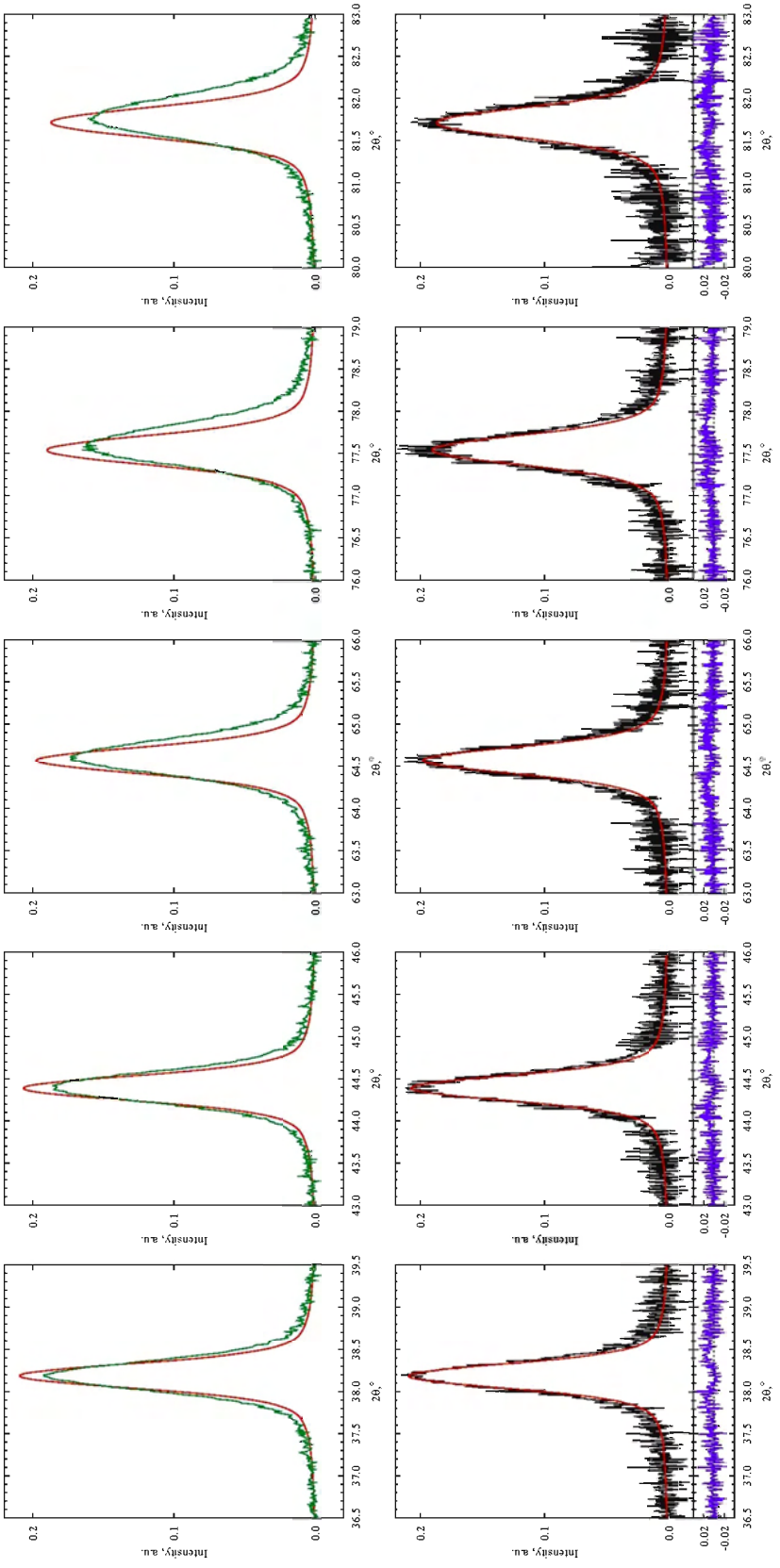

Figure 4.15: Results of applying Fourier based deconvolution technique. Top - simulated powder diffraction pattern for Au (111, 200, 220, 311 and 222 reflections) with $m = 20nm$ and $w - 0.3$ (red line) convoluted with experimentally defined instrumental function and superimposed with 3% random noise and background signals (green line). Bottom - the deconvoluted (black line) and original (red line) patterns.

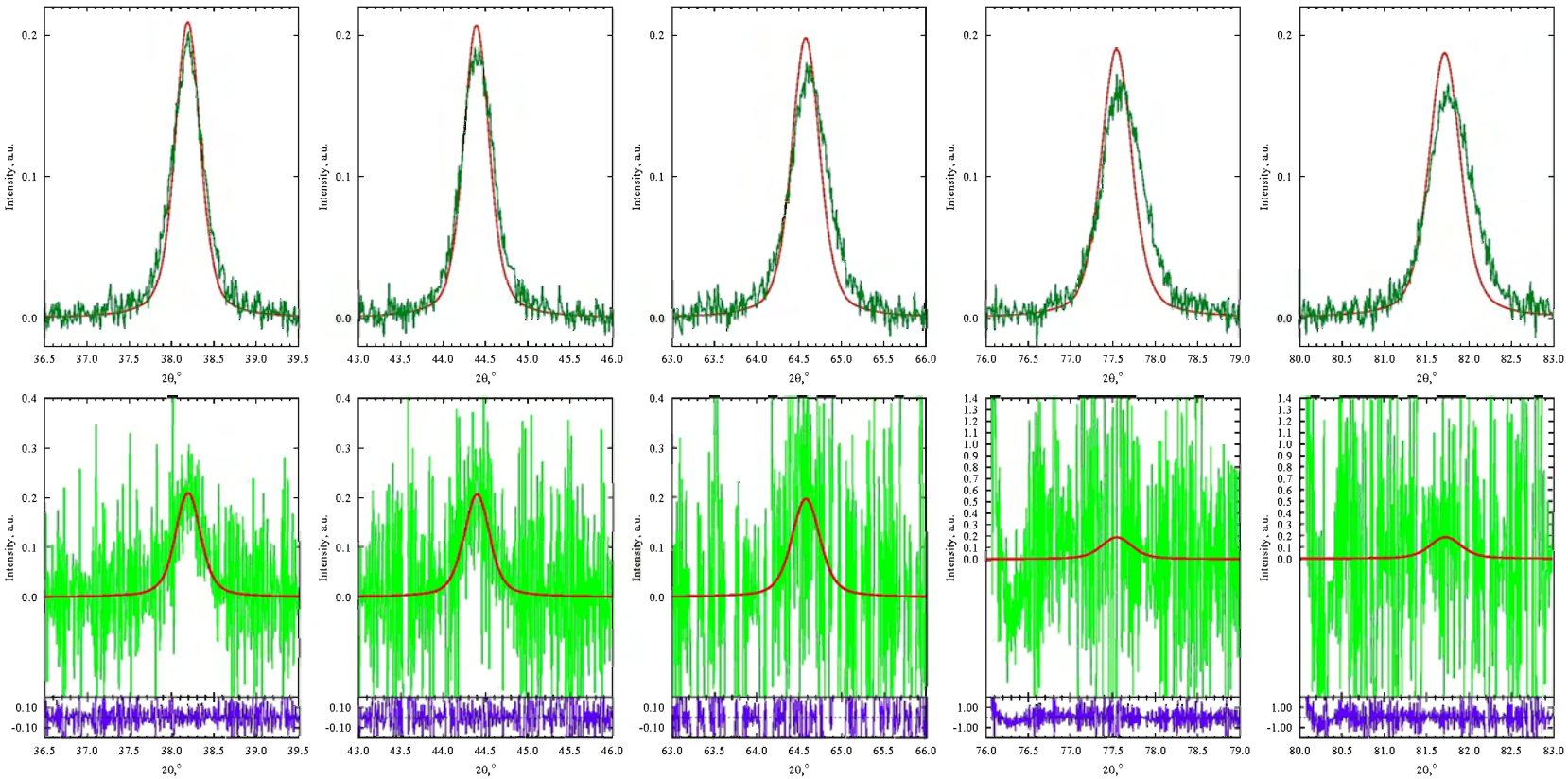

Figure 4.16: Results of applying Fourier based deconvolution technique.
Top - simulated powder diffraction pattern for Au (111, 200, 220, 311 and 222 reflections) with $m = 20nm$ and $w = 0.3$ (red line) convoluted with experimentally defined instrumental function and superimposed with 10% random noise and background signals (green line). Bottom - the deconvoluted (green line) and original (red line) patterns.

Chapter 5

Superresolving reconstruction of signals in X-ray diffractometry

The restoration of 'pure' specimen profile $F(z)$ from the experimental results obtained by means of X-ray diffractometry is the typical problem of super resolution. This leads to the solution of the inverse problem:

$$G(t) = H\{t, F(z)\} + \eta(t) = \int F(z)h(t,z)dz + \eta(t) \tag{5.1}$$

where $F(t)$ is measured profile, $h(t,z)$ is the instrumental function of the diffractometer, $\eta(t)$ is the additive noise. All the physical magnitudes are assumed to have dimensionless form and the operator H is renormalised in the following way:

$$\|H\| \equiv \frac{\int \left|\int F(z)h(t,z)dz\right|^2 dt}{\int |F(z)|^2 dz} = 1 \tag{5.2}$$

This idealised problem of the restoration $F(z)$ leads to the determination of inverse operator H^{-1}

$$H^{-1}\{z, G(t)\} = F(z) \tag{5.3}$$

and can be solved in different ways depending on the concrete form of the transformation H on conditions that the random noise is absent. The practical problem of the restoration is the determination of the estimation $\tilde{F}(z)$, which describes the true distribution of $F(z)$ satisfactorily (better than $G(t = z)$). The limitations of accuracy during the solution of practical problem are determined by the influence of the additive noise $\eta(t)$ which can not be removed from experimental measurements. Therefore, from possible solutions of an idealised problem for practical applications,

only those which provide stability of a solution against noise and with acceptable accuracy should be chosen [Beyts and Mak-Donnell, 1989].

The aim of this chapter is the investigation of the effectiveness of the methods of multiplicative inverse filtering for superresolving restoration of "pure" specimen profile in X-ray diffraction experiments.

Let us examine an idealised problem.

The shape of instrumental function of diffractometer $h(t,z)$ depends on different physical factors and structural specifications of device. In the following work it is assumed that the function $h(t,z)$ can be described as shown in chapter 4. It is easy to see from Eq. (4.30) that the kernel $h(t,z)$ is invariant by the displacement of the argument ($h(t,z) \neq h(t-z)$) and non self-adjoint ($h(t,z) \neq h^{+}(z,t)$). Therefore, inverse transformation (5.3) should be presented as numerical procedure which takes onto account listed properties of direct transformation kernel.

Let us determine the left and the right iterated kernels $R_l(z_1,z_2)$, $R_r(t_1,t_2)$ as:

$$R_l(z_1,z_2) = \int h(t,z_1)h(t,z_2)dt \tag{5.4}$$

$$R_r(t_1,t_2) = \int h(t_1,z)h(t_2,z)dz \tag{5.5}$$

From the determination (5.4), (5.5) and boundedness of function$h(t,z)$ follows that $R_{l,r}(z_1,z_2) = R_{l,r}(z_2,z_1)$ and $\int |R_{l,r}(z_1,z_2)|^2 dz_1 dz_2 < +\infty$. Therefore, there exist the solutions $\phi_j(z)$, $\varphi_j(t)$, $\lambda_j^{l,r}$, $j = 1,2,...$ of spectral problems

$$\int R_l(z_1,z_2)\phi_j(z_1)dz_1 = (\lambda_j^l)^2\phi_j(z_2) \tag{5.6}$$

$$\int R_r(t_1,t_2)\varphi_j(t_1)dt_1 = (\lambda_j^r)^2\varphi_j(t_2) \tag{5.7}$$

which have the following properties:

1. the functions $\{\phi_j(z)\}$ and $\{\varphi_j(t)\}$ are orthonormal bases in corresponding spaces;

2. $\lambda_j^l = \lambda_j^r \equiv \lambda_j > 0$;

3. The operator H implements the representation $\phi_j \leftrightarrow \varphi_j$, therefore:

$$\int h(t,z)\varphi_j(t)dt = \lambda_j \phi_j(z) \tag{5.8}$$

$$\int h(t,z)\phi_j(z)dz = \lambda_j \varphi_j(t) \tag{5.9}$$

The solution of idealised problem (5.3) can be described as

$$f(z) = \sum_{j=1}^{\infty} f_j \phi_j(z) \tag{5.10}$$

The measured output signal of the diffractometer can be presented as a series expansion in basis functions $\{\varphi_j(t)\}$:

$$G(t) = \sum_{j=1}^{\infty} g_j \varphi_j(t) \tag{5.11}$$

where

$$g_j = \int \varphi_j(t) G(t) dt \tag{5.12}$$

It should be mentioned that the sets of coefficients $\{g_j\}$ and $\{f_j\}$ contain all the information about the functions $G(t)$ and $F(z)$ and should be interpreted as their generalized spectrums. According to (5.8), (5.9) there is a relation $g_j = \lambda_j f_j$ between the expansion coefficients which determines the transformation of signal spectrum by the recording system. Therefore, the sequence of proper numbers $\{\lambda_j\}$ is the transfer characteristic of the recording system. The reconstruction of profile $F(z)$ in common spectral presentation leads to the elementary operation :

$$f_j = \frac{g_j}{\lambda_j} \tag{5.13}$$

The relations (5.12), (5.13), (5.10) determine the inverse operator H^{-1} as a simple inverse filter $\{\lambda_j^{-1}\}$. The application of this filter provides a precise reconstruction of

'pure' specimen profile according to the measurements made with low resolution on conditions that the noise is infinitesimal.

The practical application of this simple inverse filtration for the restoration of a signal credited with considerable limitations, which depend on the noise component $\eta(t)$. The difference between a real, experimental and in idealised problem of reconstruction is the obligatory presence of additive random constituent in the measured signal $G(t)$ (at least as the precision of measurements is limited). The correctness of the above mentioned statement can be understood from the analysis of Eqs. (5.1), (5.12), (5.13). Therefore, the inverse filtering of the signal $G(t)$ leads to a spectrum $\{\nu_j\}$, which is the sum of the required spectrum $\{f_j\}$ and a random noise component:

$$\nu_j = f_j + \frac{\eta_j}{\lambda_j} \tag{5.14}$$

The diffractometer has a limited discrete resolution, therefore, its transfer characteristic decreases in a high frequency region as fast as the device resolution decreases: $\lambda_j \xrightarrow[j\to\infty]{} 0$. Therefore, with increasing j, a random component increases unlimited those leads to the complete destruction of the solution by the use of an inverse transformation (5.10). Thus, the solution of the practical restoration problem requires the limitations of an influence of high frequency noises. This can be made by the replacement of the inverse filter $\{\lambda_j^{-1}\}$ by some regularisation filter $\tilde{H}^{-1}(\lambda_j)$, whose transfer characteristic has to coincide with $\{\lambda_j^{-1}\}$ in the region of low j and has to decrease to zero by $j \to +\infty$:

$$\tilde{H}^{-1}(\lambda_j) \approx \lambda_j^{-1}, \qquad \lambda_j > \Lambda_0 \tag{5.15}$$

$$\tilde{H}^{-1}(\lambda_j) \to 0, \qquad \lambda_j << \Lambda_0 \tag{5.16}$$

The value Λ_0 determines a division of the signal spectrum into informative and noisy regions and is proportional to the effective level of noise (in the case of weighted

noise to its root-mean-square amplitude).

The simplest method of the restoration of the experimental regularisation problem leads to the use of a procedure when in expansion (5.10) only a limited number of coefficients f_j comprises, which corresponds to relative high values of λ_j [Piskarev et al., 1997]. Such a procedure is equivalent to the filtration of the spectrum $\{f_j\}$ by the inverse rejector filter with its transfer characteristic

$$\tilde{H}^{-1}(\lambda_j, J_0) = \begin{cases} \lambda_j^{-1}, & j \leqslant J_0 \\ 0, & j > J_0 \end{cases} \tag{5.17}$$

The approximate solution $\{\tilde{f}_j\}$ of the restoration problem can be described as :

$$\tilde{f}_j = \tilde{H}^{-1}(\lambda_j, J_0) \cdot g_j \tag{5.18}$$

The transition $\{\tilde{f}_j\} \rightarrow \tilde{F}(z)$ is achieved by the use of (5.10).

The rejection limit J_0 depends on the noise level and on the velocity of the decrease of proper numbers λ_j and should be chosen in the following way: noise constituent must have an acceptable amplitude. The disadvantage of rejective filter is the "break" of its transfer characteristic at $j = J_0$. In most cases it leads to significant distortions of the retorted signal. For this reason, a regularisation filter with a smoothed characteristic is desired for the practical use.

Smoothed filters with the properties (5.15) are built by cutting the inverse filter extension into the power series:

$$\frac{1}{\lambda_j} = \sum_k a_k (1 - \tau\lambda_j)^k, \; k \in Z \tag{5.19}$$

The kind of the regularisation filter is determined by the choice of expansion coefficients a_k, constant τ and order of filter K:

$$\tilde{H}^{-1}(\lambda_j, K) = \sum_{k=0}^{K} a_k (1 - \tau\lambda_j)^k \tag{5.20}$$

The methods of the solution of the restoration problem by applying the filters (5.20), are nothing else but the modification of a Tikhonov inverse problem regularisation procedure for a generalized spectral representation (5.10), (5.11). The particular feature of Tikhonov filters is the possibility of their optimization by different parameters (K, a_k, τ) for obtaining the best solution. Unfortunately it is rather difficult to determine a well-founded criterion for such an optimization even for one problem. Therefore, the effectiveness of Tikhonov regularisation technique in most cases depends on the experience of the researcher.

The problem of the creation of optimal regularised inverse filter leads to the solution of the next statistical model.

Let us imagine a sequence of measurements $G_1(t)$,$G_2(t)$,..., which corresponds to the specimen profile $F_1(z)$, $F_2(E)$,.... It is supposed, that the ensemble of all possible realisations of the signal $\{F_s(z)\}$ and the noise $\{\eta(t)\}$ create crossuncorrelated central random processes with certain correlation functions $\langle F(z_1)F(z_2)\rangle$ and $\langle \eta(t_1)\eta(t_2)\rangle$ and corresponding to spectral density matrices $\langle f_j f_k\rangle$ and $\langle \eta_j \eta_k\rangle$, respectively (brackets denote the realisation ensemble averaging). The filter $\tilde{H}^{-1}_{opt}(\lambda_j)$ is supposed to be the statistically optimal inverse filter, if it minimises the root-mean-square restoration error in means of ensemble:

$$\sigma^2(E) = \left\langle \left| F(t) - \tilde{F}(t) \right|^2 \right\rangle = \min \tag{5.21}$$

The solution of the problem (5.21) can be presented as the multiplication of the simple inverse filter with some regularisation filter $W(\lambda_j)$:

$$\tilde{H}^{-1}_{opt}(\lambda_j) = \frac{W(\lambda_j)}{\lambda_j} \tag{5.22}$$

Then the problem (5.21) leads to the construction of the filter $W(\lambda_j)$, which optimally recovers the signal f_j from the noisy invert signal ν_j (5.14):

$$\tilde{f}(z) = \sum_j \left(W(\lambda_j)\nu_j\right)\phi_j(z) = \sum_j \left(W(\lambda_j)f_j + W(\lambda_j)\frac{\eta_j}{\lambda_j}\right)\phi_j(z) \tag{5.23}$$

According to (5.10), (5.21), (5.23) the root-mean-square error:

$$\sigma^2(E) = \sum_{j,k} \phi_j(z)\phi_k(z) \left(\langle f_j f_k \rangle \left(1 - W(\lambda_j)\right)\left(1 - W(\lambda_k)\right) + \frac{\langle \eta_j \eta_j \rangle}{\lambda_j \lambda_k} W(\lambda_j) W(\lambda_k) \right) \tag{5.24}$$

It is known that the minimum root-mean-square error of signal by the use of a linear filter is equal to the difference between signal dispersions and estimation [Levin, 1989].

$$\sigma^2_{min}(z) = \left\langle F^2(z) \right\rangle - \left\langle \tilde{F}^2(z) \right\rangle \tag{5.25}$$

Using (5.10), (5.23) the equation (5.24) leads to:

$$\sigma^2_{min}(z) = \sum_{j,k} \phi_j(z)\phi_k(z) \left(\langle f_j f_k \rangle \left(1 - W(\lambda_j)W(\lambda_k)\right) - W(\lambda_j)W(\lambda_k) \frac{\langle \eta_j \eta_k \rangle}{\lambda_j \lambda_k} \right) \tag{5.26}$$

The derivation of Eqs. (5.23), (5.25) implies the noncorrelatedness between signal and noise.

For the determination of $W(\lambda_j)$, the results of integration (taking into account the orthonormalisation of the basis $\{\phi_j(z)\}$) of the Eqs. (5.23), (5.25) should be compared. After the transformation of the result of integration and taken into account arbitrary of $\langle f_j f_k \rangle$, $\langle \eta_j \eta_k \rangle$, the $W(\lambda_j)$ can be described as the generalized Wiener filter:

$$W(\lambda_j) = \frac{\left\langle f_j^2 \right\rangle}{\left\langle f_j^2 \right\rangle + \dfrac{\left\langle \eta_j^2 \right\rangle}{\lambda_j^2}} \tag{5.27}$$

Then optimal inverse filter is defined as:

$$\tilde{H}^{-1}_{opt}(\lambda_j) = \frac{W(\lambda_j)}{\lambda_j} = \frac{\lambda_j}{\lambda_j^2 + \dfrac{\left\langle \eta_j^2 \right\rangle}{\left\langle f_j^2 \right\rangle}} \tag{5.28}$$

The relation $\left\langle \eta_j^2 \right\rangle / \left\langle f_j^2 \right\rangle$ contain the parameters of additive noise in the output of the system and in the input of the signal and, therefore, is not suitable for the practical application. Thus, it can be replaced by some constant χ, which on the assumption

of (5.2) can be seen as rough estimate of the noise/signal ratio in the output of the system.

The optimization procedure for the inverse filter requires some additional remarks. First of all it is considered that $\{F_s(z)\}$ creates a random centre process, which is not veridical, because the profile $F(z)$ is a positive quantity. Thus, before the implementation of the Wiener filter it is necessary to perform the preprocessing of the experimental results in the way that they correspond to the 'signals' $F(z) - \langle F(z) \rangle$. The Wiener filter (5.28) minimises the root-mean-square error of the restoration signal. However, it is not a necessary criterion of the quality of experimental restoration problem. For creation of the optimal filter it is necessary to know the diagonal elements of the matrix of spectral distribution $\left\langle f_j^2 \right\rangle$ of the ensembles $\{F_s(z)\}$, which are not known exactly and are designed by using some general considerations about the signals. At the same time specific restoration signal may not be the typical representative of the model of the statistic ensemble and its restoration error strongly exceeds the ensemble-averaged one. Therefore, it is necessary to perform the comparative analysis of the restorations results received by applying of different methods and to chose only the method which gives the best results for the solution of the concrete problem.

In this thesis the effectiveness of superresolution methods for the problems of X-ray diffractometry are investigated by a numerical simulation of an instrumental-broadened profile. The simulation of experimental data was done as described in §4.6.

For superresolving reconstruction of signals the programme was written in Mathworks' MATLAB . For Singular Value Decomposition (SVD) the corresponding algorithm from Regularization Tools package [Hansen, 1994] for MATLAB was used.

The resolution function of the diffractometer in some range $[z_0 - \Delta z; z_0 + \Delta z]$ is

numerically characterised by the half-width of the instrumental function $\sigma_h(z_0)$:

$$\sigma_h^2(z_0) = \frac{\int (z-\bar{z})^2 \left|h(z_0,z)\right|^2 dz}{\int \left|h(z_0,z)\right|^2 dz} \tag{5.29}$$

$$\bar{z} = \frac{\int z \left|h(z_0,z)\right|^2 dz}{\int \left|h(z_0,z)\right|^2 dz} \tag{5.30}$$

The enhancement of the resolution using inverse filtration can be estimated by defining in the same way the half-width $\sigma_\delta(z_0)$ of the reconstructed profile $\tilde{F}_\delta(z_0,z)$:

$$\tilde{F}_\delta(z_0,z) = \tilde{H}^{-1}\left\{G; \int \delta(z-z_0)h(t,z)dz\right\} \tag{5.31}$$

In Fig. 5.1 the reconstruction of a specimen profile (simulated by Eq. (3.19) with $m = 100nm$ and $w = 0.2$) using inverse rejection and optimal filters is shown. The parameters of the filters were selected in proportion to small noise level ($<3\%$). It is possible to achieve approximately the same improvement of resolution $\sigma_h(z_0)/\sigma_\delta(z_0) \approx 2.5$ with those filters. The profiles recovered using inverse rejection filter have side lobes related to the above mentioned 'break' in its transfer characteristics. The information about the resolution of the inverse filter is useful for the analysis of restoration results: signal features which correspond to the segments $\Delta z < \sigma_\delta$, should be interpreted as random ones. Besides, the rational approach of the restoration problem expects previous smoothing of the experimental data. The value σ_δ allows to estimate the minimal window of the smoothing filter what does not lead to the loss of useful information.

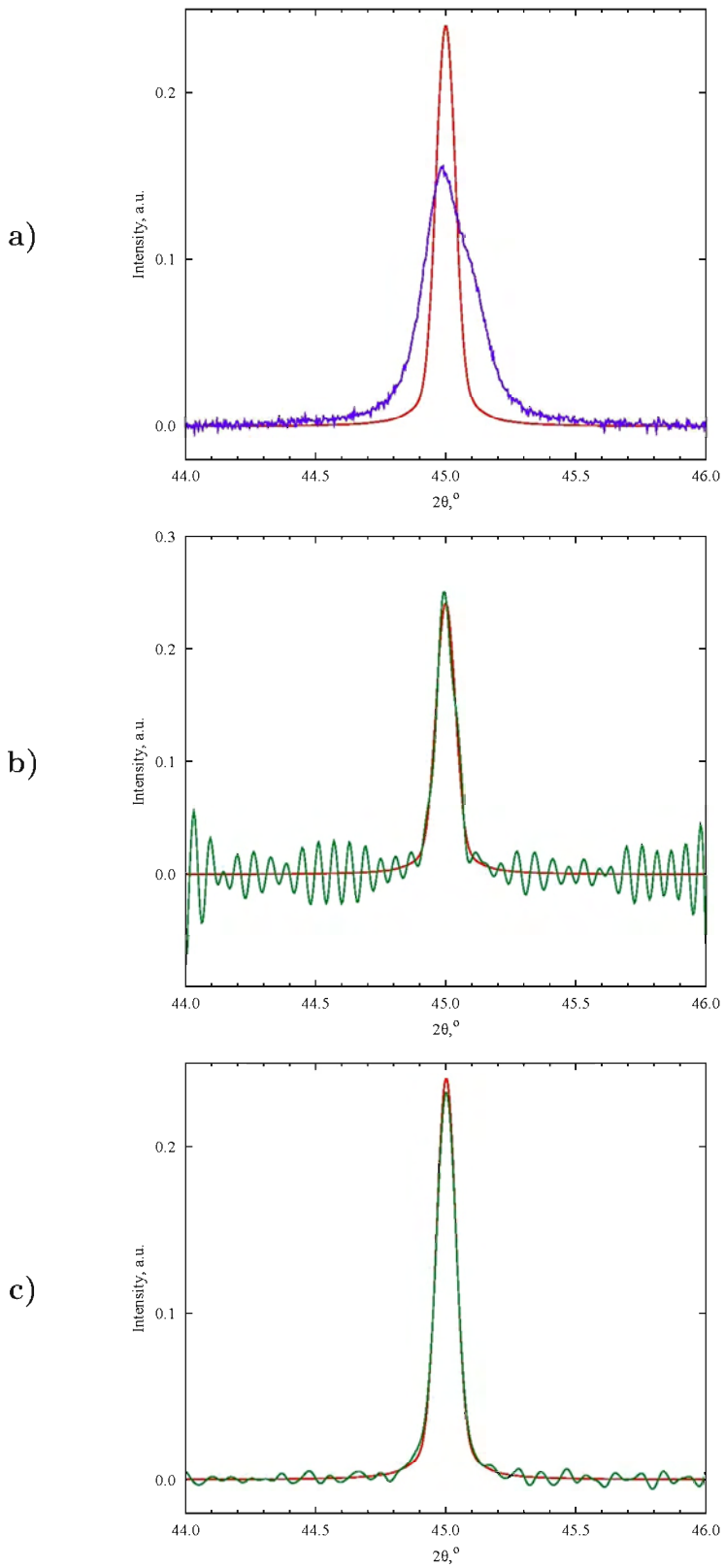

Figure 5.1: Reconstruction of specimen profile (green line) using inverse rejection filter (b) and optimal filter (c). a) - experimental signal (blue line), level of noise - 3%; red line is original specimen profile.

The stability of superresolving procudures was proved for the optimal filter on the simulated signal with the levels of additive noise of 3, 5, 10 and 20%. The double peak profile was simulated by Eq. (3.19) with $m = 100nm$ and $w = 0.2$. The distance between two peaks was approximately equal to average FWHM of both peaks. The results of specimen profile reconstruction are shown on Figs. 5.2, 5.3. The optimal filter shows high stability, however the overestimation of the noise level χ leads only to slight worsening of the restoration results (Fig. 5.3).

The implementation of superresolution procedures as regularised inverse filtration leads to the improvement of the level of profile resolution in the problems of X-ray diffraction as well as to the successfully removing of instrumental broadening form experimental profile. They show high stability in terms of large experimental noise.

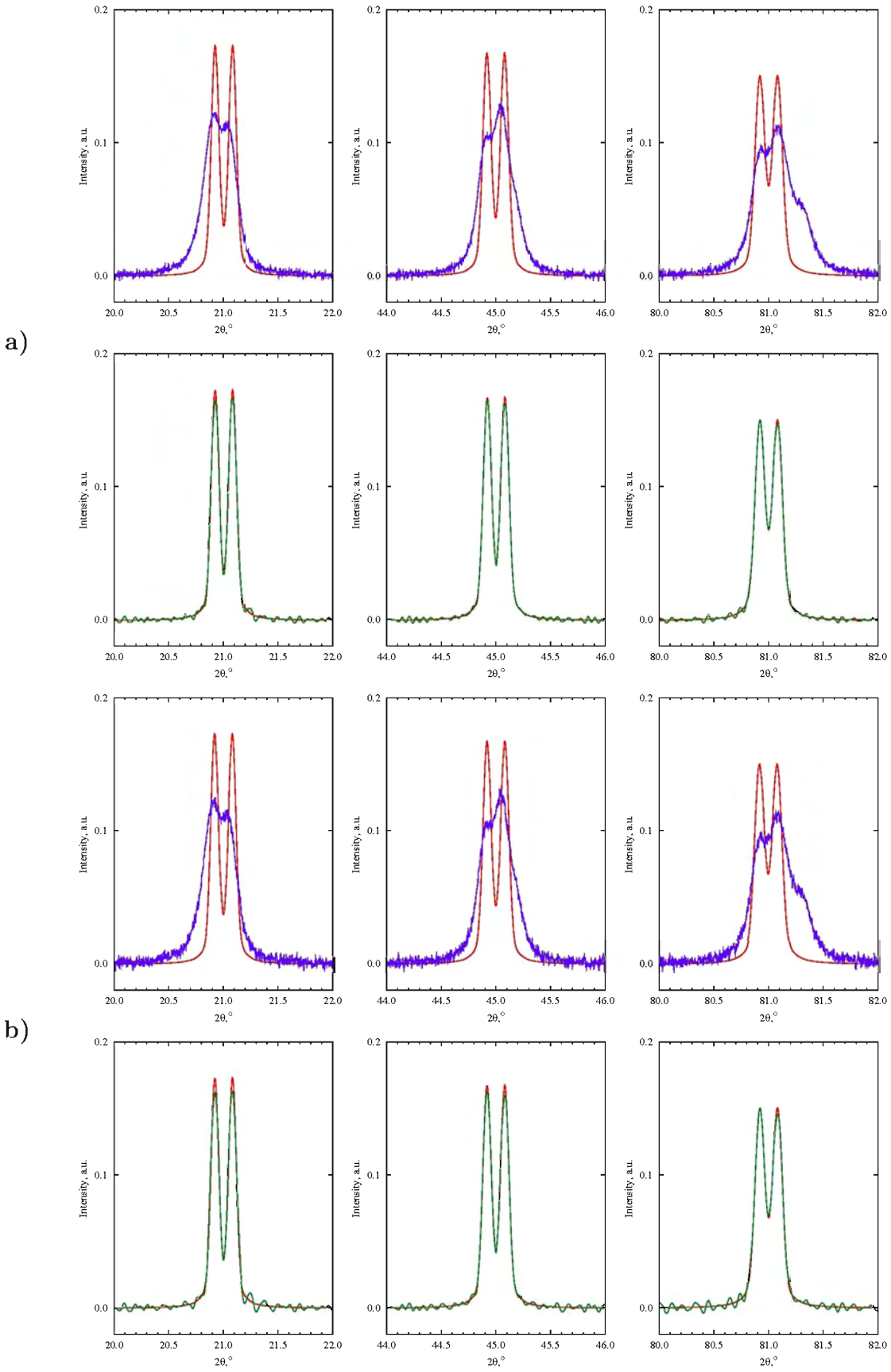

Figure 5.2: Reconstruction of specimen profile (green line) using optimal filter. Noise level: a) - 3%; b) - 5%. Original specimen profile - red line; Experimental profile - blue line.

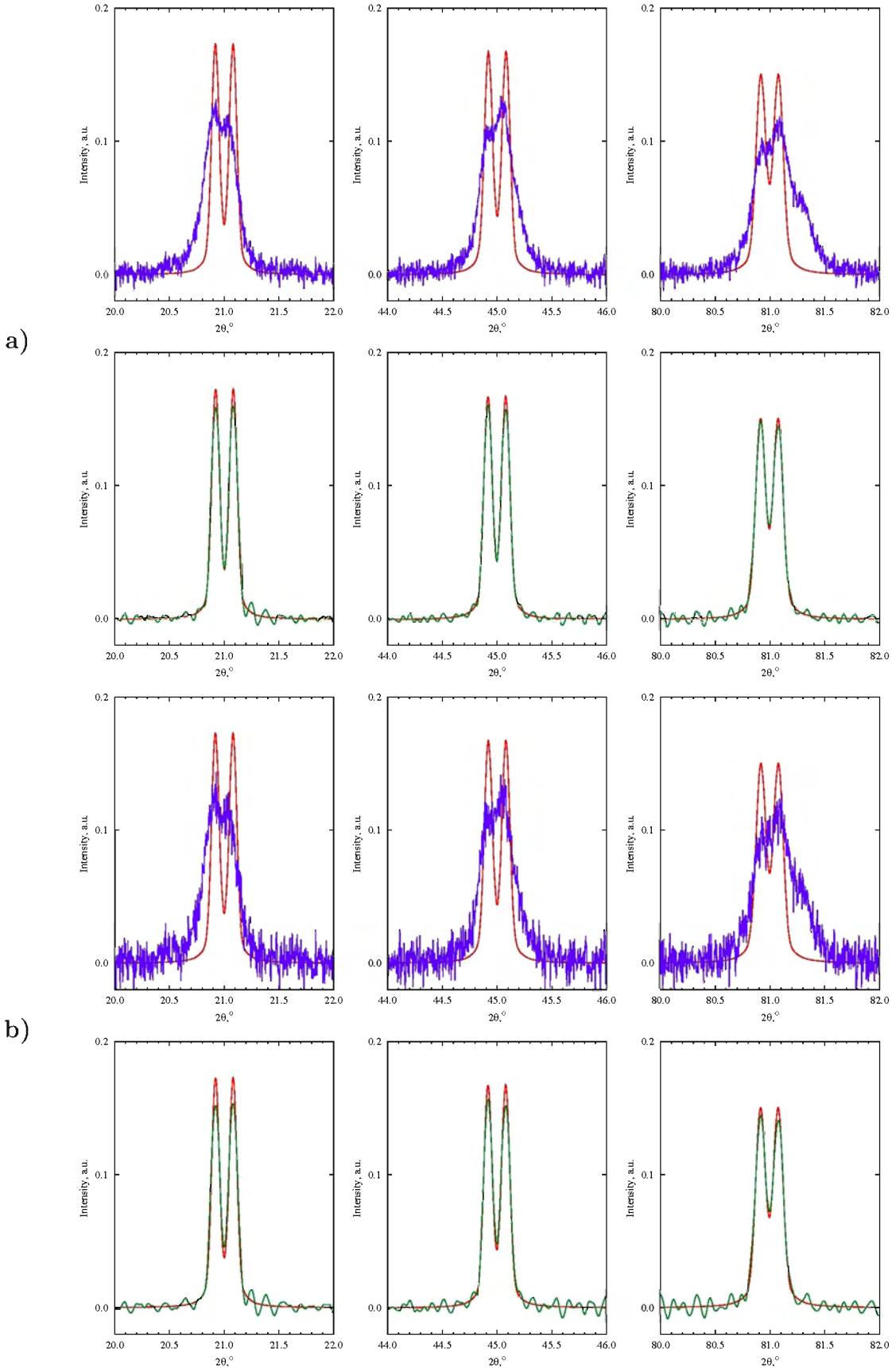

Figure 5.3: Reconstruction of specimen profile (green line) using optimal filter. Noise level: a) - 10%; b) - 20%. Original specimen profile - red line; Experimental profile - blue line.

5.1 Deconvolution of the instrumental aberrations from powder x-ray diffraction using regularisation technique

The simulation of an instrument-broadened X-ray profile, described in 4.6, was carried out to investigate the properties and stability of the superresolving method for the deconvolution of instrumental function proposed in the previous section. The simulated pattern for nanostructured gold with the median $m = 20nm$ and logarithmic standard deviation $\omega = 0.3$ according to Eg. (3.33) was used as the specimen profile. Both profiles were calculated over the interval of $30.0^o - 90.0^o$. The low constant background was added to simulate the effect of the misfitting error on the background level. Additionally Gaussian noise, calculated by standard technique was added to the convoluted results (its negative value was not restricted as they can arise after the background removing procedure). The normalised specimen and instrumental profiles, as well as the simulated profile for different noise levels are given in Figs. 5.4 - 5.7 (Top).

For superresolving reconstruction of signals programmes in Mathworks' MATLAB were written. For the Singular Value Decomposition (SVD) a corresponding algorithm from Regularization Tools package for MATLAB was used. The optimal regularisation parameter was choosen according to the algorithm proposed by [Kojdecki, 2004].

The results of the nanostructured gold profile reconstruction are shown in Figs. 5.4 - 5.7. The calculated lognormal distribution parameters from recovered gold profile is presented in Tab.5.1. It is easy to see that the recovered parameters are in discrepancy to original parameters within experimental error.

It is easy to see (Figs. 5.4-5.7) in comparison with results received by Fourier deconvolution (Figs. 4.15-4.16) that the optimal filter shows high stability, however the overestimation of the noise level χ leads only to slight worsening of the restoration results (Fig. 5.7), whereas, with Fourier deconvolution even lower noise level destroys

Table 5.1: Calculated lognormal distribution parameters from simulated data for nanostructured Au ($m = 20$ nm, $w = 0.3$) with different noise levels.

Noise, %	m,nm	w
1	20.3 ± 0.4	0.29 ± 0.01
3	20.8 ± 0.6	0.28 ± 0.02
5	21.2 ± 0.9	0.26 ± 0.02
10	24.1 ± 2.5	0.26 ± 0.04
20	27.1 ± 3.1	0.22 ± 0.08
30	29.4 ± 4.5	0.25 ± 0.10

the solution completely (Fig. 4.16). An additional advantage of the above described regularisation technique is its independence on the concrete analytical form of the approximation of the instrumental function. Hence, the introduction of additional effects to describe the instrumental function, or completely changing the model for describing the instrumental function will just change the form of the kernel $h(t, z)$, however, the algorithm for recovering of the specimen profile will stay valid without any change.

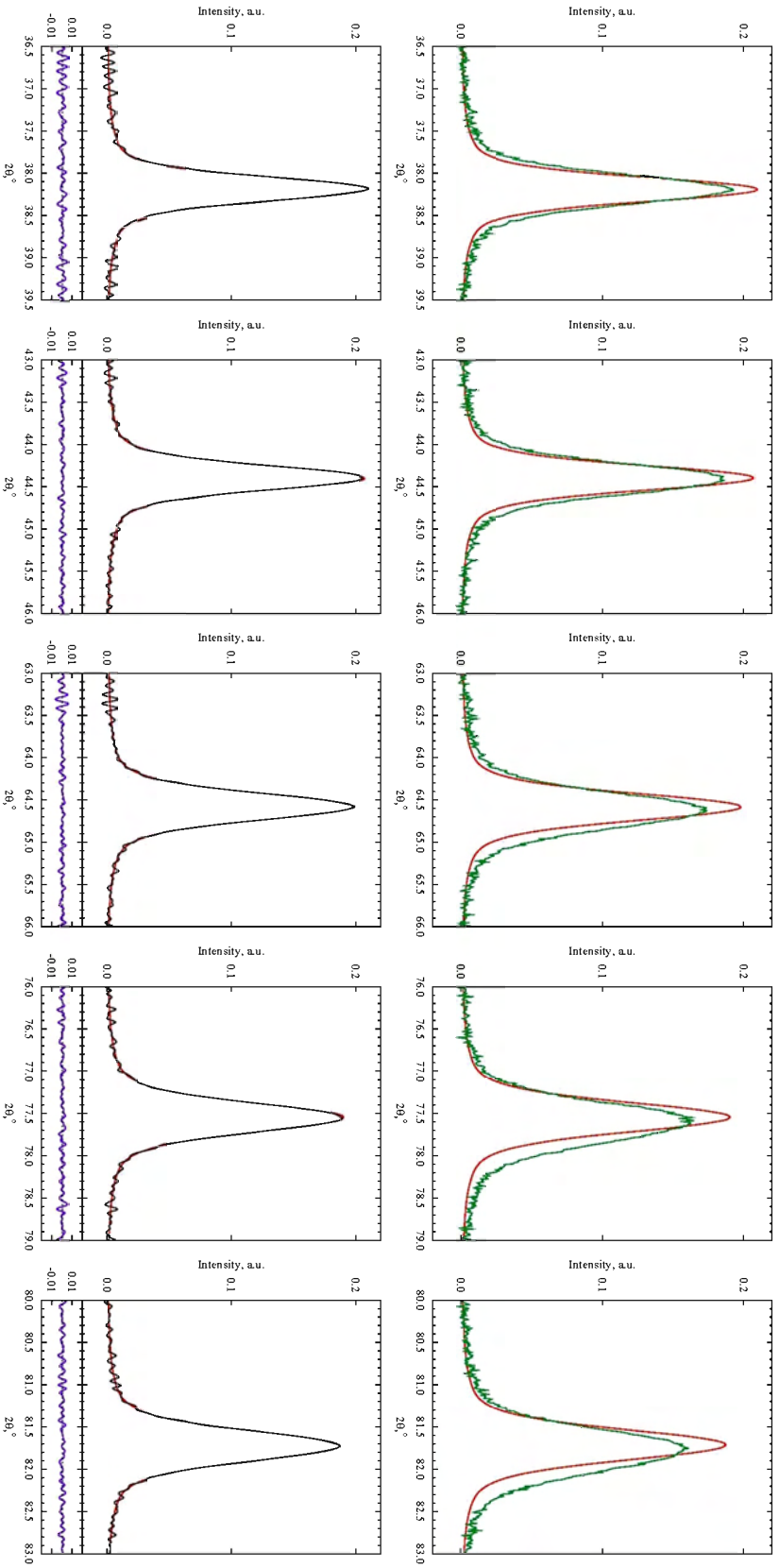

Figure 5.4: Top - simulated powder diffraction pattern for Au (111, 200, 220, 311 and 222 reflections) with $m = 20mm$ and $w = 0.3$ (red line) convoluted with the experimentally defined instrumental function and superimposed with 3% random noise and background signals (green line). Bottom - the deconvoluted (black line) and original (red line) patterns.

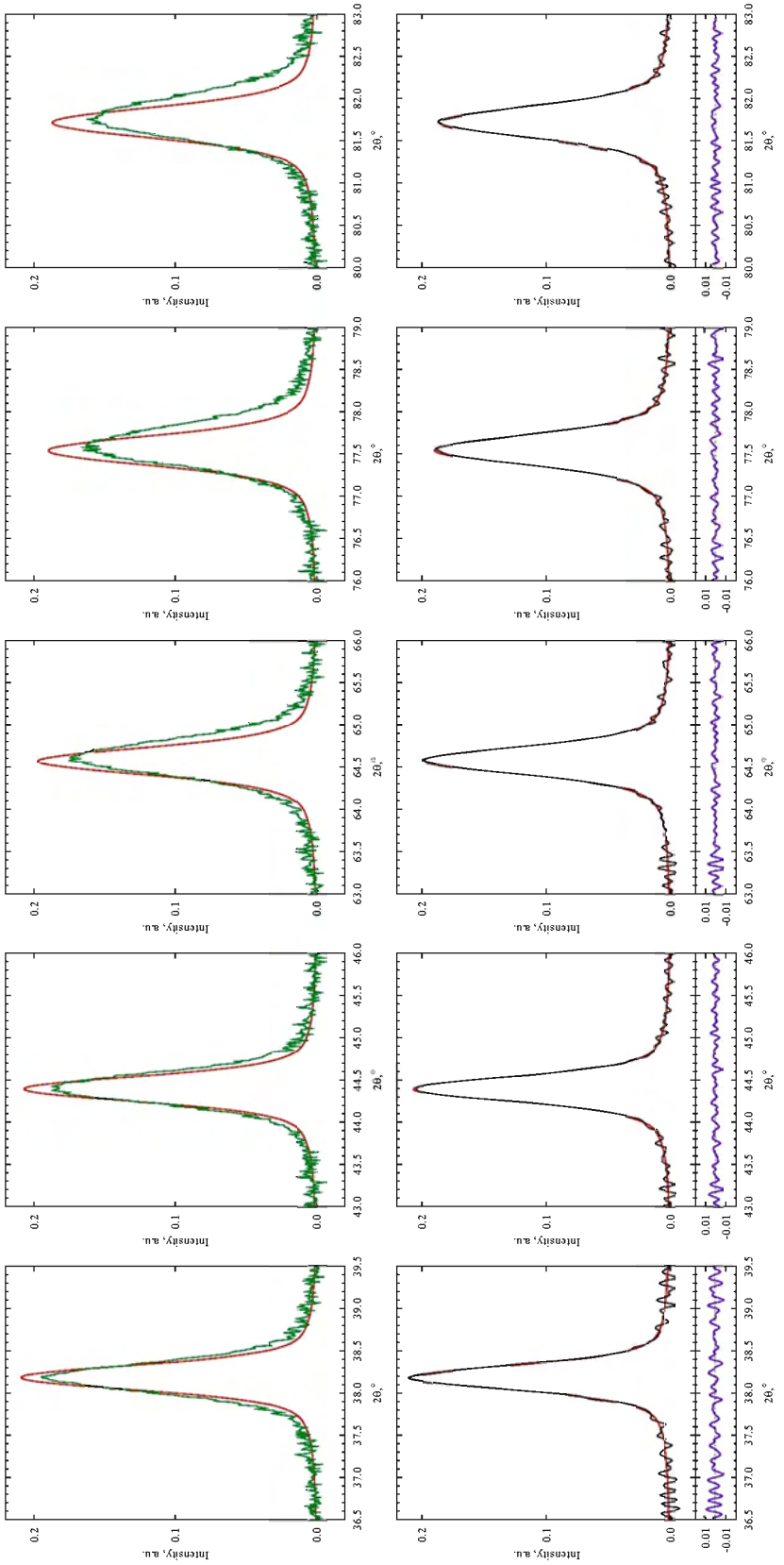

Figure 5.5: Top - simulated powder diffraction pattern for Au (111, 200, 220, 311 and 222 reflections) with $m = 20nm$ and $w = 0.3$ (red line) convoluted with the experimentally defined instrumental function and superimposed with 5% random noise and background signals (green line). Bottom - the deconvoluted (black line) and original (red line) patterns.

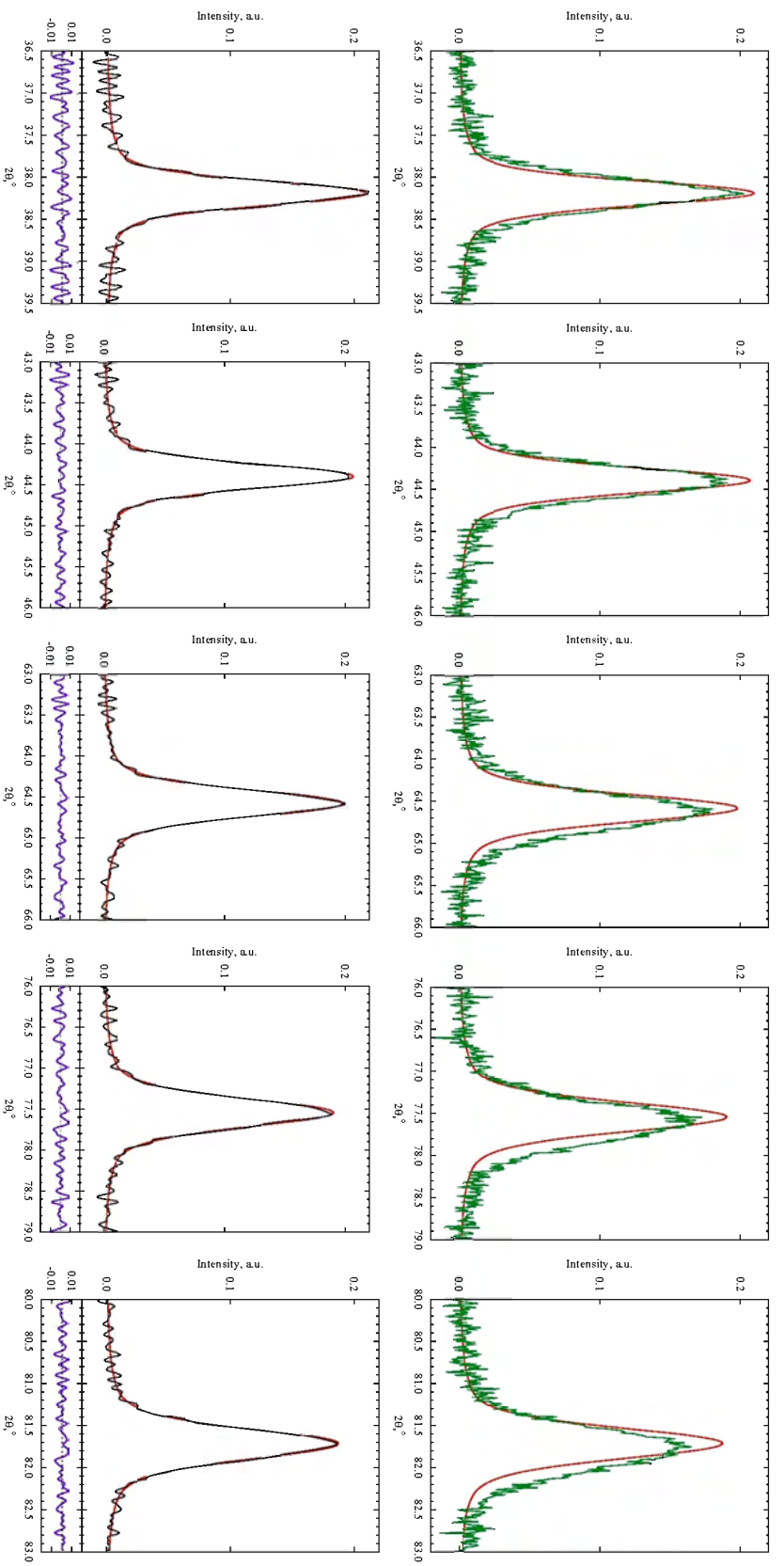

Figure 5.6: Top - simulated powder diffraction pattern for Au (111, 200, 220, 311 and 222 reflections) with $m \quad 20nm$ and $w = 0.3$ (red line) convoluted with the experimentally defined instrumental function and superimposed with 10% random noise and background signals (green line). Bottom - the deconvoluted (black line) and original (red line) patterns.

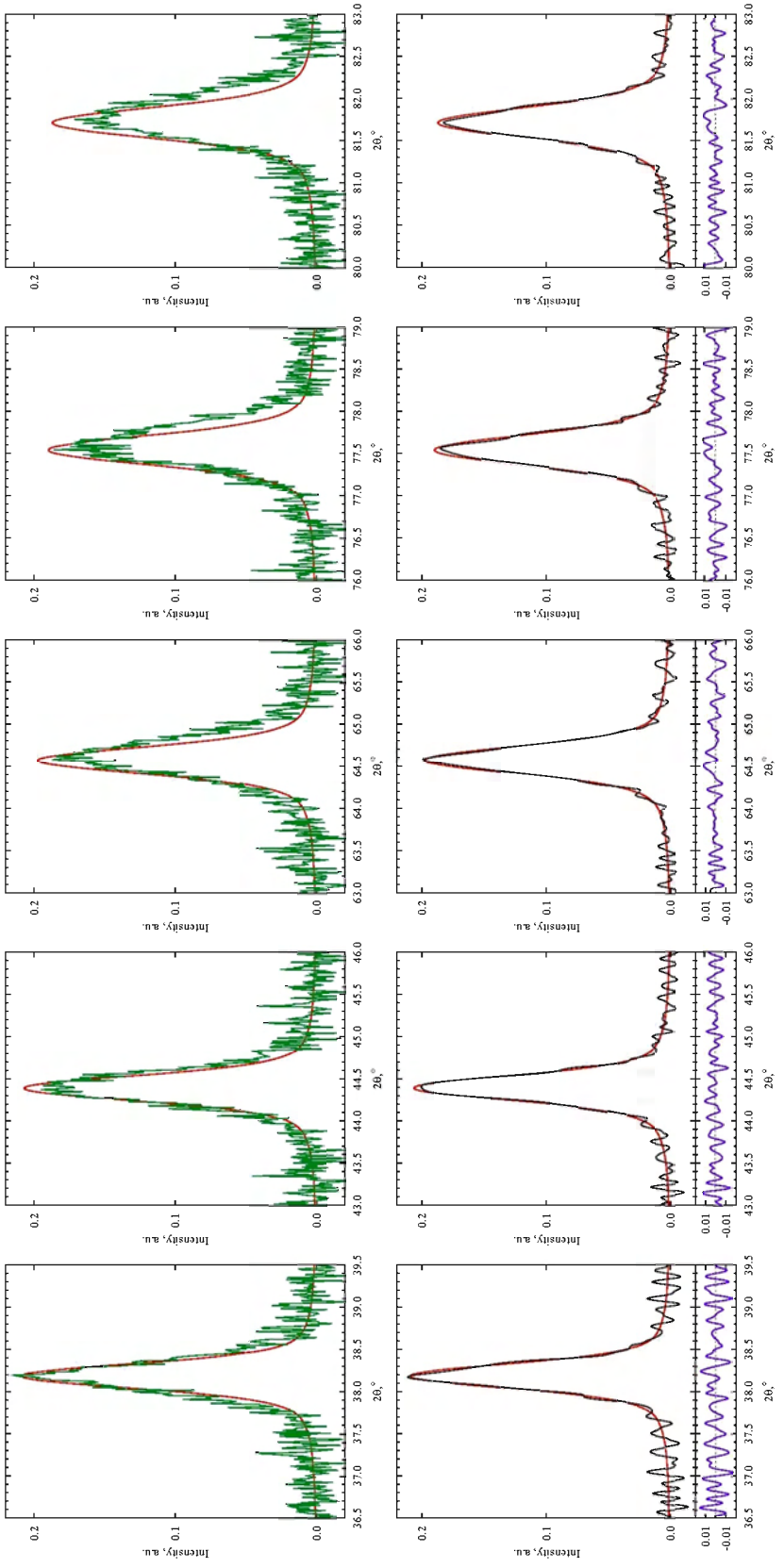

Figure 5.7: Top - simulated powder diffraction pattern for Au (111, 200, 220, 311 and 222 reflections) with $m = 20nm$ and $w = 0.3$ (red line) convoluted with the experimentally defined instrumental function and superimposed with 20% random noise and background signals (green line). Bottom - the deconvoluted (black line) and original (red line) patterns.

Chapter 6

Application of the developed technique

6.1 Application of the convolution model for strain-size assessments using CeO_2

This chapter reports the application of the convolution model (see Chapter 3 for the description of the model) for assessing the size and strain parameters of CeO_2. The NIST SRM 660a LaB_6 standard and Al_2O_3 were used for the definition of XRD instrument broadening function according to Chapter 4. A comparison of the convolution size and strain values was made with those for the Voigt integral breadth analysis. The size values are then compared to TEM results.

Nanocrystalline cerium oxide powder prepared by aging a cerium(III) nitrate solution in the presence of hexamethylenetetramine [Chen and Chen, 1993] was used for checking the X-ray diffraction data treating algorithm proposed in this work .

In Fig. 6.1, the TEM images of the cerium oxide powder are shown, whereas in Fig. 6.3, the experimental diffraction profile of the same sample and the reconstructed 'pure' specimen profile of cerium oxide using the regularisation technique (see Chapter 5) are presented. It can be seen that the instrumental aberration is successfully removed without increasing the noise in the reconstructed profile. It should be admitted that the use of Fourier based deconvolution techniques (see §4.6),however, leads to unacceptable results.

In Fig. 6.3 (Bottom) the fit of a 'pure' specimen profile with the proposed convolution model (see Chapter 3) is shown. The parameters obtained for measured CeO_2 are: median size $m = 4.9$ nm, logarithmic standard deviation $\omega = 0.41$ (geometric

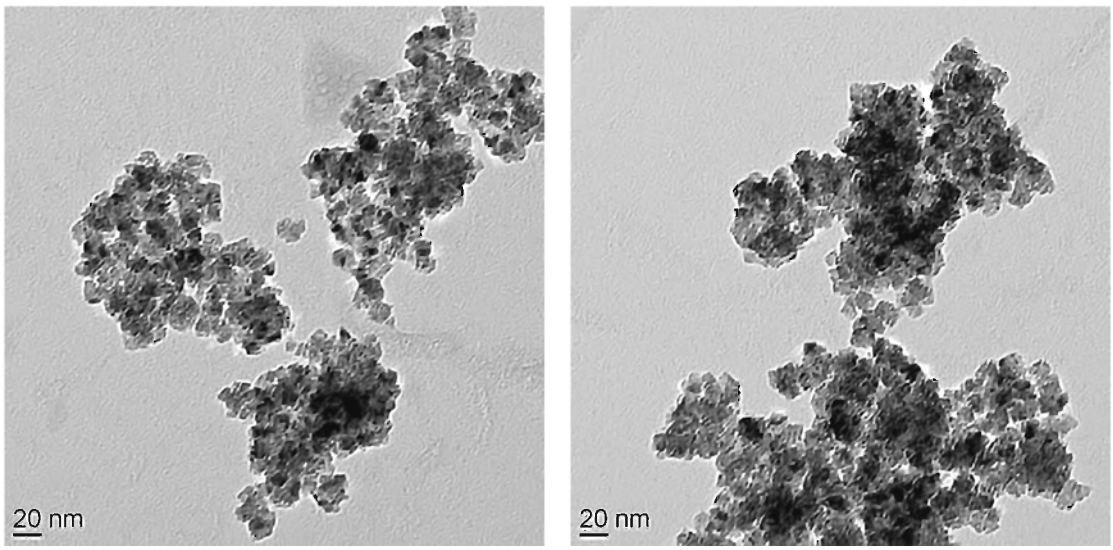

a) b)

Figure 6.1: TEM of the CeO_2 sample. Homogeneous crystallite size distribution (see Fig. 6.4) can be observed on different parts (a,b) of the sample.

standard deviation $\sigma = 1.51$) and strain $e = 0.18$.

In Fig. 6.2, CeO_2 experimental profile and its fit to the Double-Voigt Approach using TOPAS v 2.1 [BrukerAXS, 2003] are shown. The parameters obtained from this fit are: volume weighted column length $L_{vol} = 7.85 \pm 4.4$ nm and strain $e_0 = 0.23 \pm 0.05$.

In Fig. 6.4, the comparison of the results received with different techniques are shown. The data are in a good agreement. Fit of TEM data with lognormal distribution gives median size $m = 6.07$ nm and a logarithmic standard deviation $\omega = 0.38$

From the XRD and TEM results it can be seen that the distribution curves of relative frequency by length (diameter) of grains for the CeO_2 obtained by both techniques are very similar. The difference between the data for crystallite size obtained from TEM lognormal distribution analysis and applying of the convolution model for X-ray diffraction does not exceed 1-2 nm. It is suggested that the coherently diffracting domain is smaller than the apparent particle size. Also the data obtained with

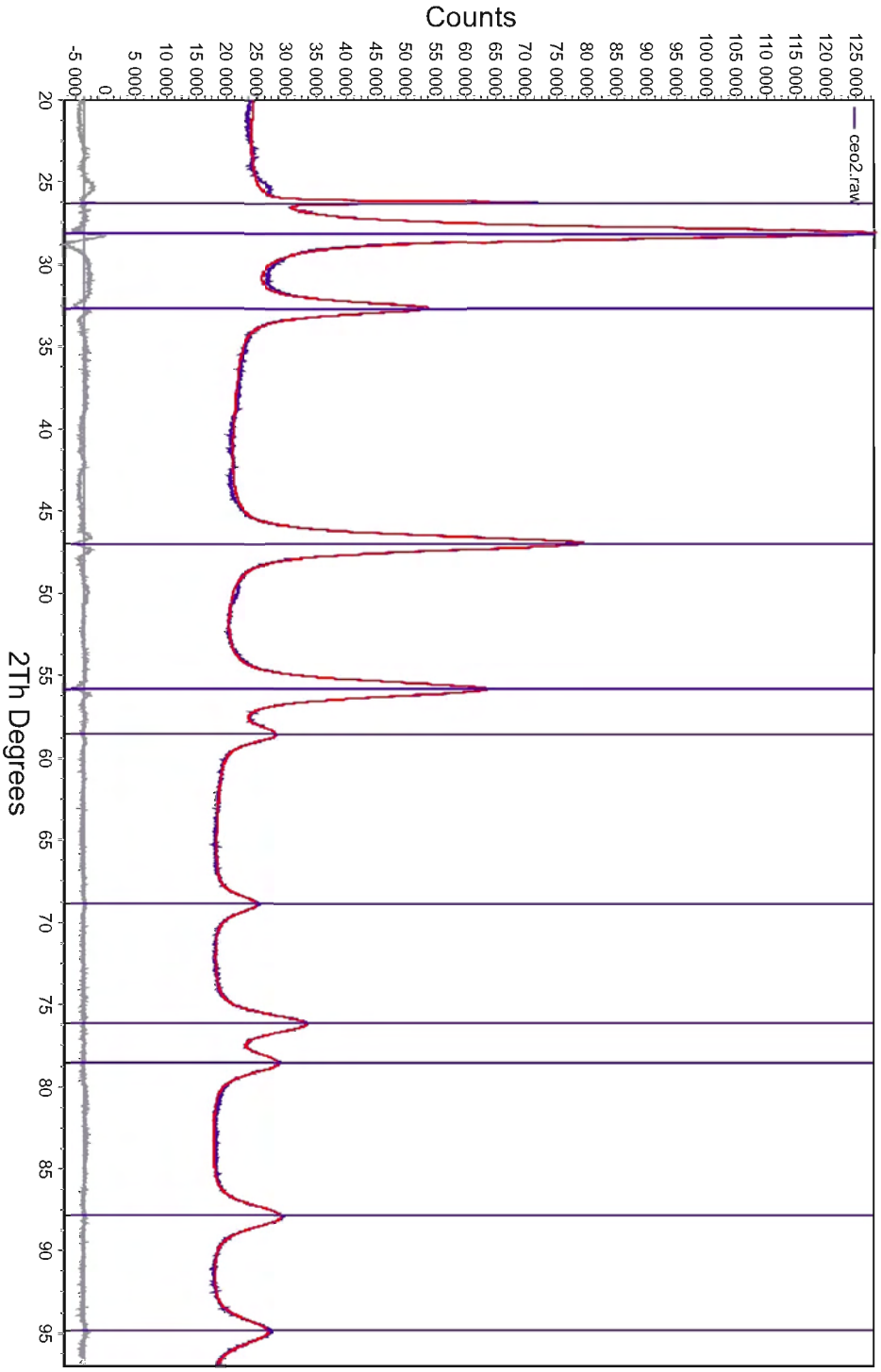

Figure 6.2: The measured profile (blue line) for CeO_2 and the fit (red line) using TOPAS. $R_{wp} = 1.7$.

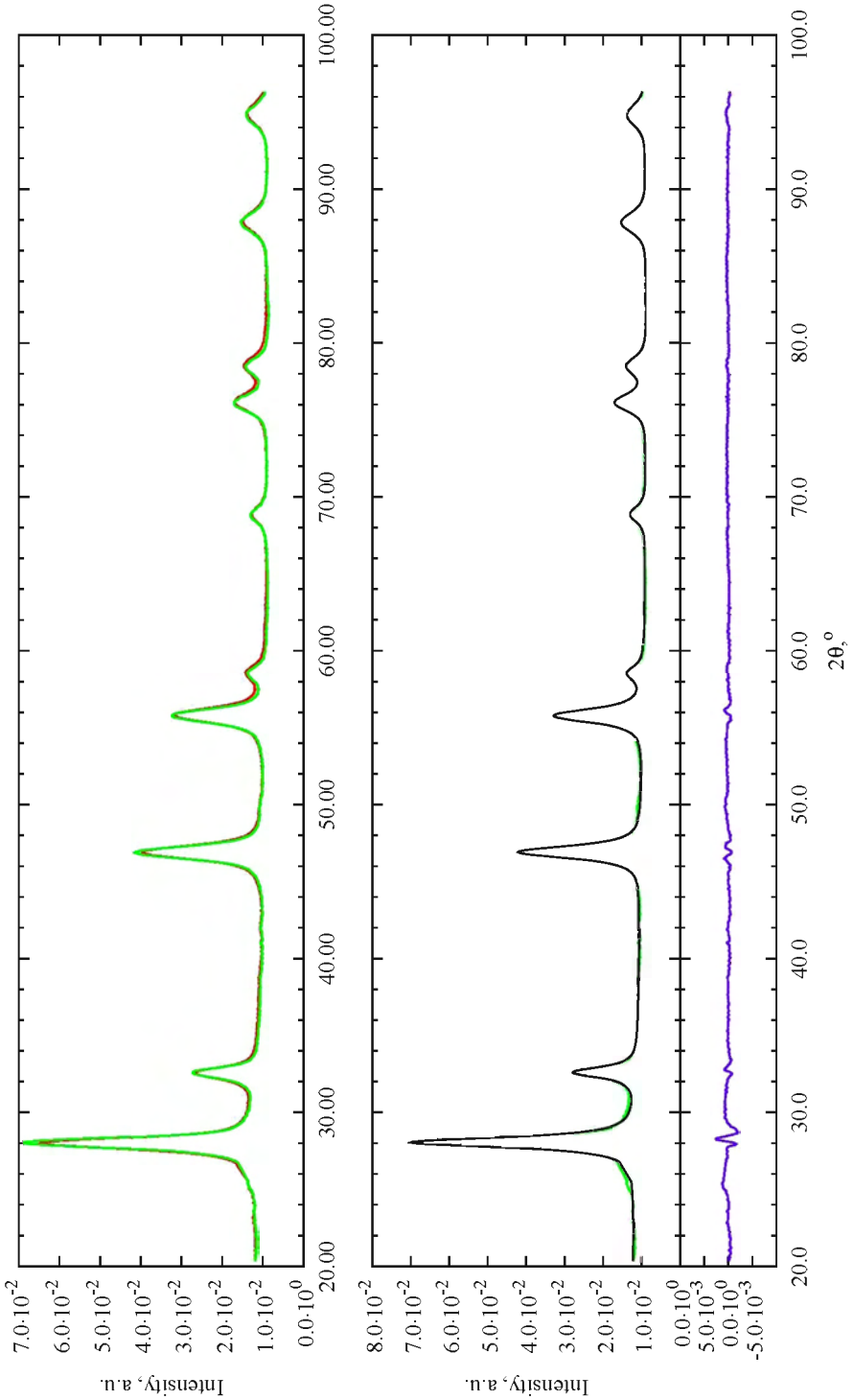

Figure 6.3: The measured profile (red line) for CeO_2; reconstructed 'pure' specimen profile (green line) and its fit (black line). $R_{wp} = 2.2$.

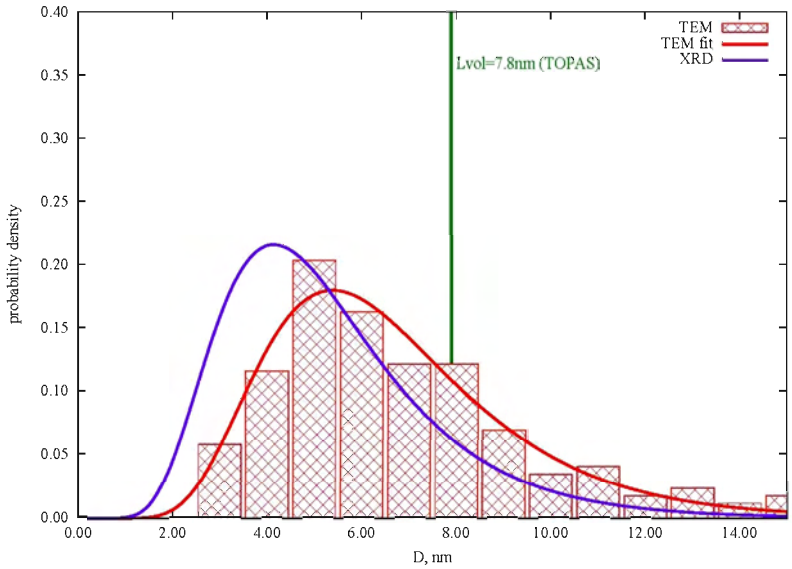

Figure 6.4: Particle size distributions of CeO_2. The histogram represents normalised data from TEM images obtained by counting of about 500 particles; red line is the fit of TEM data with lognormal distribution function; blue line represents distribution calculated by proposed convolution model using X-ray diffraction. Green line - the volume weighted column length received with TOPAS V2.1 [BrukerAXS, 2003].

TOPAS are in good agreement with the developed convolution model. By using of Eg. (3.14) the volume-weighted mean value for lognormal distribution received with convolution model is $\langle D \rangle_V = 8.8nm$. Therefore, it can be concluded that the results for the volume weighted column length obtained by the use of TOPAS software and the convolution based technique are consistent within the experimental accuracy.

6.2 Application of the convolution model for strain-size assessments using in-situ high temperature X-ray diffraction.

This chapter reports the application of the convolution model (see Chapter 3 for description of the model) for the estimation of the size and strain parameters in gold, gold-silver and gold-palladium alloys using TEM and XRD data. Again, NIST SRM 660a LaB_6 standard and Al_2O_3 were used for the definition of the XRD instrumental broadening function described in Chapter 4. The 'convolution' size and strain values are compared with those obtained from TEM analysis and the results of the commercial software TOPAS.

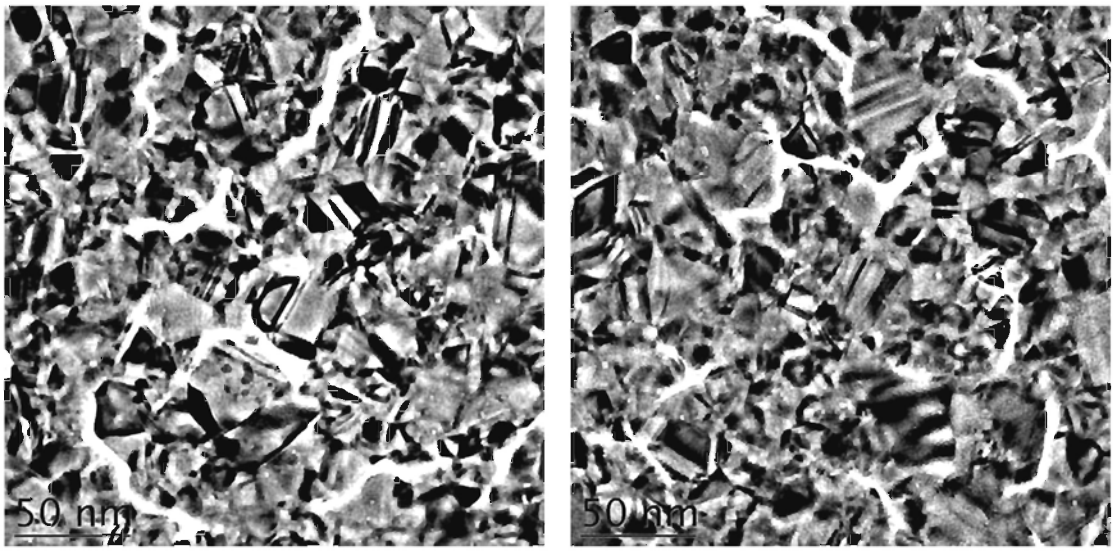

a) b)

Figure 6.5: TEM of the nanocrystallite gold sample. Crystallite size on different places of the investigated sample (a,b) can be determined.

TEM analysis of the nanocrystalline gold sample gives the mean crystallite size of approximately 20 nm. The parameters for lognormal crystallite size distribution calculated from X-ray diffraction data using convolution model are: median size m = 7.5nm and logarithmic standard deviation ω = 0.61. The crystallite size of the

investigated gold samples calculated with the TOPAS software is 25±6 nm. However, it should be noted, that TOPAS evaluate the volume weighted column length, which in case of using convolution model is $\langle D \rangle_V = 7.5 * \exp(3.5 * 0.61^2) = 27.6nm$. It can be concluded that the application of developed in this work model leads to the results comparable with those obtained by TEM and commercial software techniques (taking into account that TOPAS provides volume weighted average size values). The TEM-derived grain sizes, however, are larger then those received with by means of the convolution techniques. It is known that stacking faults and twin boundaries reduce the apparent grain size calculated from diffraction peak broadening. Such defects decrease the spatial extent of the columns contributing to the coherent scattering of X-rays; that is, the size of the resulting 'coherent scattering region' bounded by the defects (and grain boundaries) is smaller than that of the crystallite containing the defect(s). Since stacking faults or twins are nearly always present to some extent in real materials (and in special in fcc metals), the size distribution values calculated from such materials using X-ray diffraction are always smaller than those evaluated with TEM analysis.

Nanocrystalline gold, gold-silver and gold-palladium alloys were electrodeposited by pulsed techniques as reported in Yevtushenko et al. [2007]. The thermal stability of nanocrystalline materials is important from both, fundamental and practical viewpoints. In the design of micro-/nanodevices, mechanical properties are essential since most of them are known to exhibit a dependence on grain size. To improve the mechanical properties (hardness etc.) of coatings and bulk materials nanoscaling in crystallite size should be achieved. But the problem of hardness decrease during the production/utilization process at elevated temperatures causes a decrease of the life time of the material. Therefore, investigations of the thermal stability of nanostructured samples are of high interest. The simultaneous observation of the dependence

of the crystallite size on the annealing temperature is possible by using of in-situ high temperature X-ray diffraction; however, the solution of the next problem should be achieved. During the measurements it is necessary to obtain a big number of measurements within a short period of time at a constant temperature. However, the noise level of the measured signal increases by decrease of the time of data acquition. For these reasons an effective and stable algorithm is required for the deconvolution of the instrumental function. During the heating of samples the values for crystal size as well as for microstrain will change. Therefore, a correct and robust algorithm for the deconvolution with the following size-strain separation is required.

The stability of the electrodeposited nanocrystalline materials at high temperature conditions is investigated with X-ray diffraction using a position sensitive detector (Braun Inc., Germany). In the angular range covered by the detector we observe the gold 111, 200, 220, 311 and 222 Bragg reflections.

In the Figs. 6.6 and 6.7, a comparison of Fourier based and regularisation technique is shown. It is possible to see that the proposed regularisation technique deconvolutes the signal without increasing the noise level in the deconvoluted profile. As a result, all the peak profiles obtained by the removing of instrumental function using regularisation technique form high temperature gold diffraction patterns with a narrow and symmetrical single peak profile. Whereas applying standard Fourier based deconvolution technique causes a dramatice increase of the noise level: the peaks with low intensity completely vanish from the deconvoluted results.

In Fig. 6.8 (Top), the experimental diffraction profile for gold at different temperatures, the reconstructed 'pure' specimen profile and its fit with the proposed convolution model (see Chapter 3) are shown.

The change of the size distribution with increasing temperature for gold is shown in Fig. 6.10.

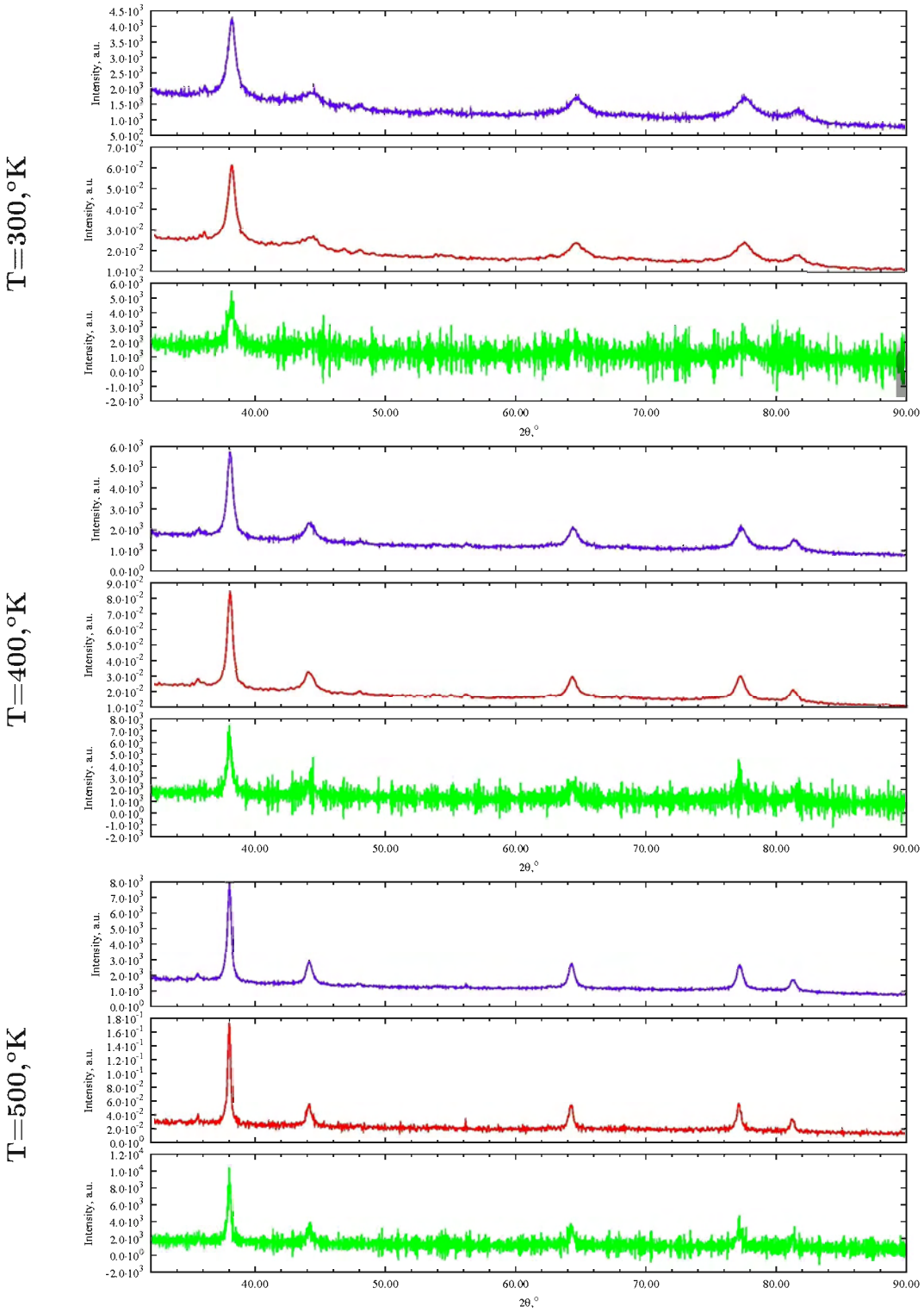

Figure 6.6: Comparison of Fourier based (green lines) and regularisation (red lines) techniques. The measured at different temperatures profiles for Au (111, 200, 220, 311 and 222 reflections) are represented as blue lines.

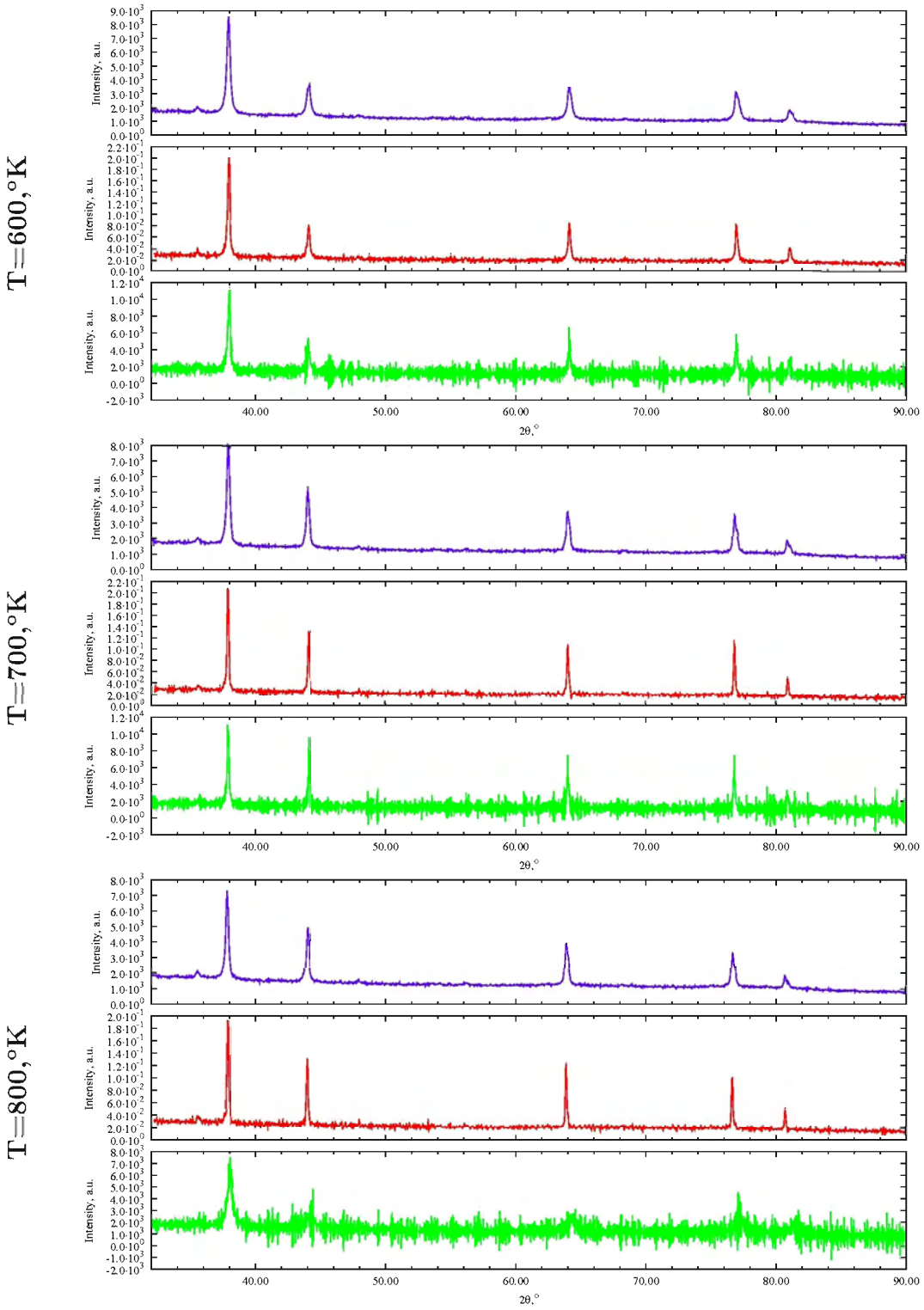

Figure 6.7: Comparison of Fourier based (green lines) and regularisation (red lines) techniques. The measured at different temperatures profiles for Au (111, 200, 220, 311 and 222 reflections) are represented as blue lines.

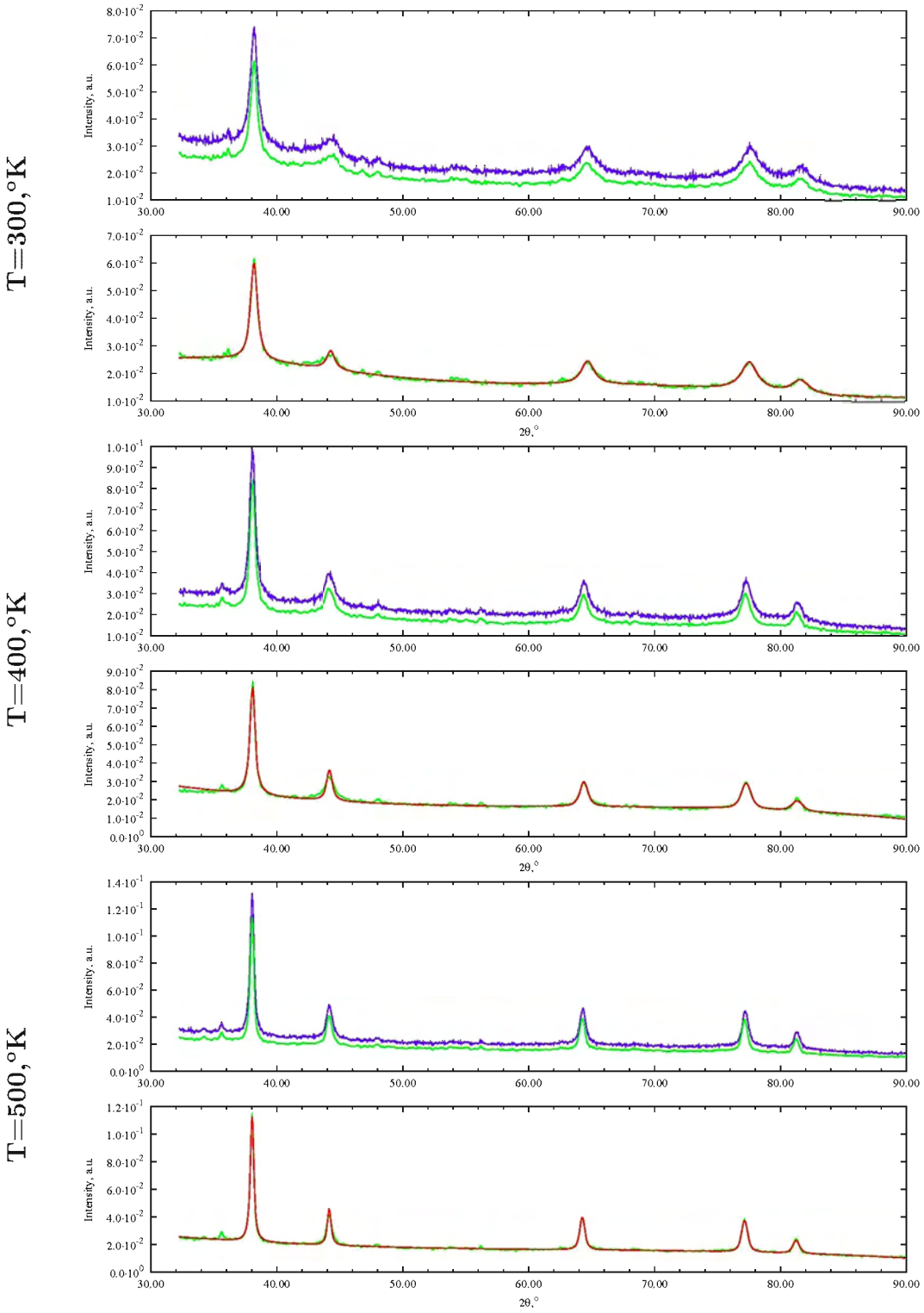

Figure 6.8: The measured profile at different temperatures (black line) for AuAg alloy (111, 200, 220, 311 and 222 reflections); reconstructed 'pure' specimen profile (blue line) and its fit (green line).

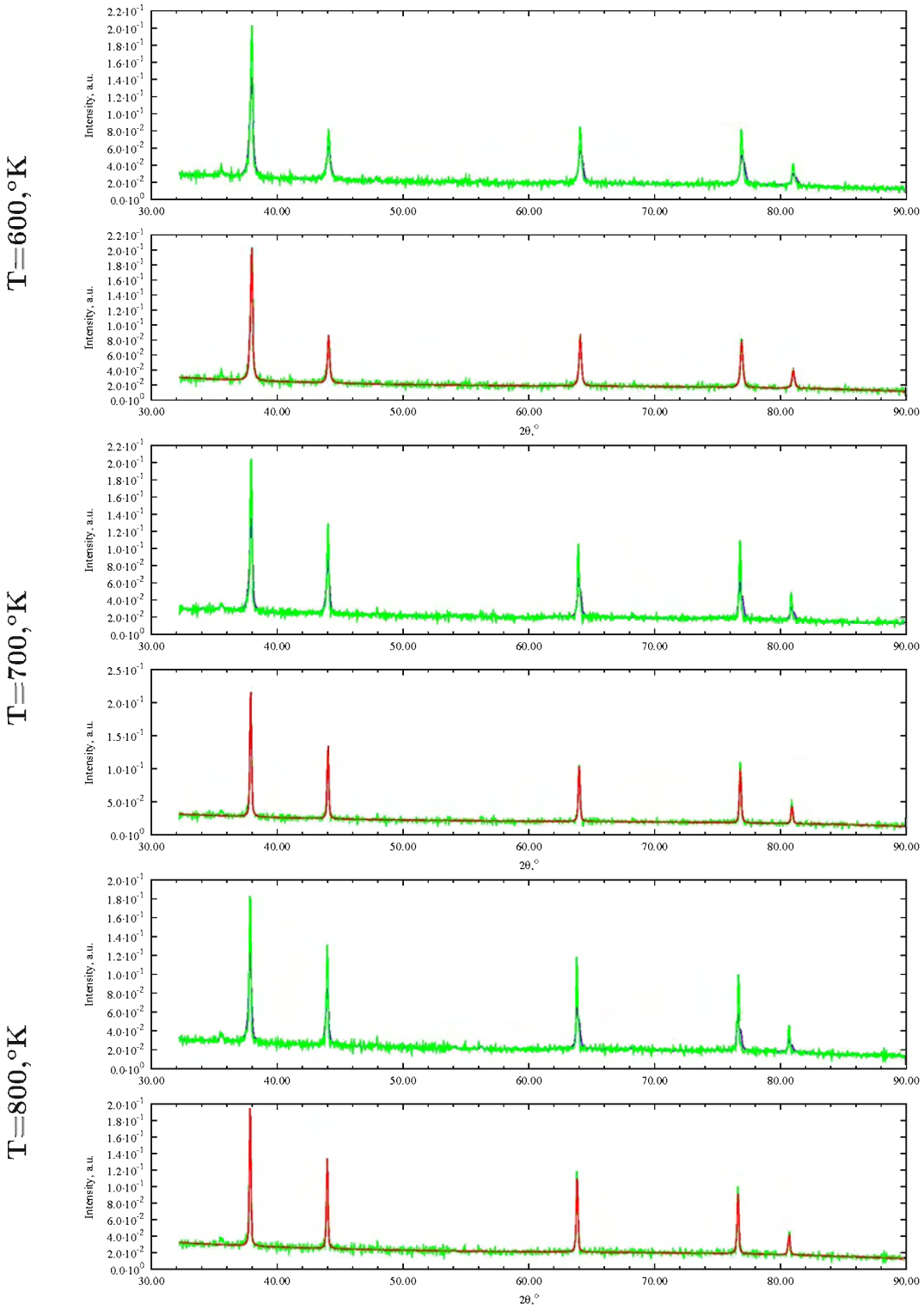

Figure 6.9: The measured profile at different temperatures (black line) for AuAg alloy (111, 200, 220, 311 and 222 reflections); reconstructed 'pure' specimen profile (blue line) and its fit (green line).

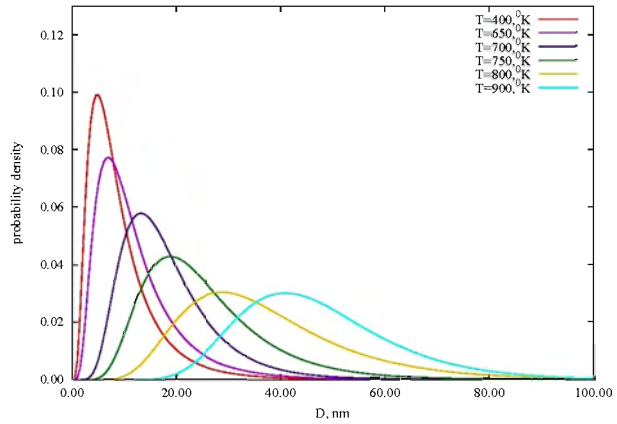

Figure 6.10: Temperature dependence of the crystallite size distribution of Au.

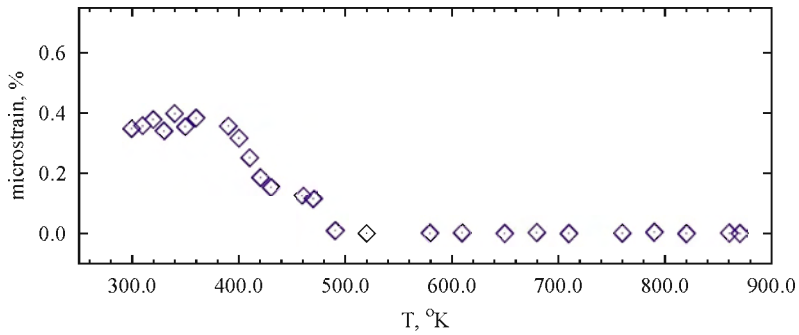

Figure 6.11: Temperature dependence of the strain of Au.

In the same way changes of the size distribution with temperature for gold-silver and gold-palladium alloys are presented in Figs. 6.12 and 6.14, respectively.

The gold, the gold-silver and the gold-palladium samples were heated from room temperature up to 873 K with a rate of 2 K min^{-1}. In the as prepared state, gold has a microstrain of 0.38% (Fig. 6.11). After heating nano-gold up to 873K this parameter decreases to 0.001%.

The gold-silver sample showed thermal stability up to approximately 600 K (Fig. 6.12). The microstrain decreases during the heating from the value of 0.45% ((Fig. 6.11)), corresponding to the sample measured at room temperature, down to 0.001%

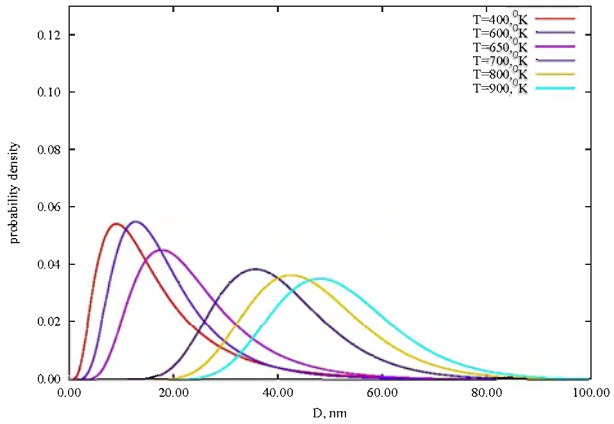

Figure 6.12: Temperature dependence of the crystallite size distribution of AuAg alloy.

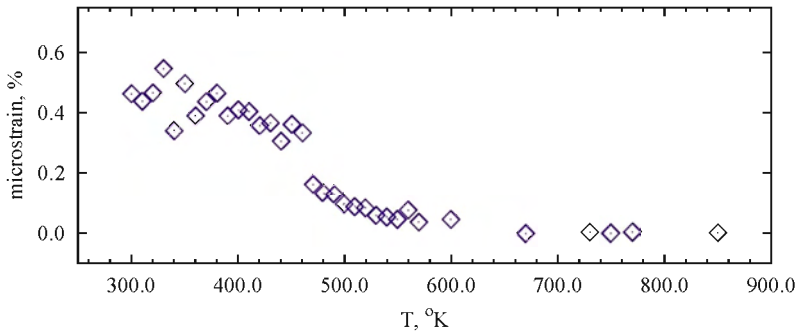

Figure 6.13: Temperature dependence of the strain of AuAg alloy.

and after that the crystallite growth sets in. The gold-palladium sample a similar behavior like the other samples: the microstrain decreases from 0.65 % down to 0.001% (see Fig. 6.15) and after that the crystallites start to grow.

In the Figs. 6.16, 6.17 and 6.18 the change of the mean crystallite size and strain with temperature calculated with TOPAS v2.1 [BrukerAXS, 2003] is represented. It is easy to see that this dependences are similar with those calculated by convolution model.

Therefore, it can be concluded that the method proposed in this work can be successfully applied to experimental data.

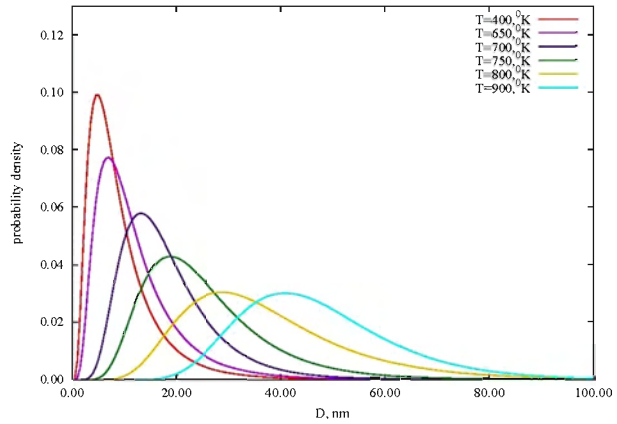

Figure 6.14: Temperature dependence of the crystallite size distribution of AuPd alloy.

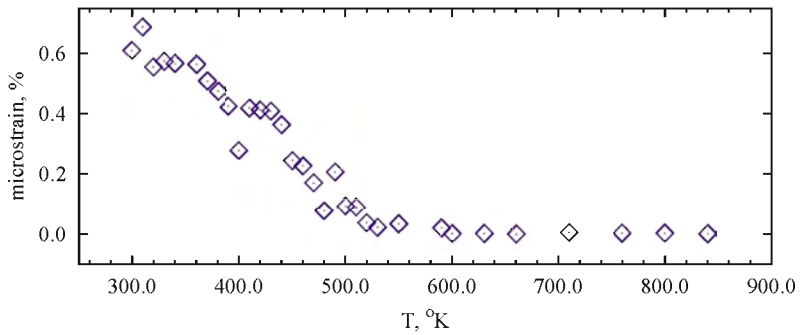

Figure 6.15: Temperature dependence of the strain of AuPd alloy.

The kinetics of high temperature crystallite growth is described by several authors Natter et al. [1997, 2000]. As shown in Yevtushenko [2007] the growth of the crystallites (obtained by the technique proposed in this work) can be well described by the model from the literature.

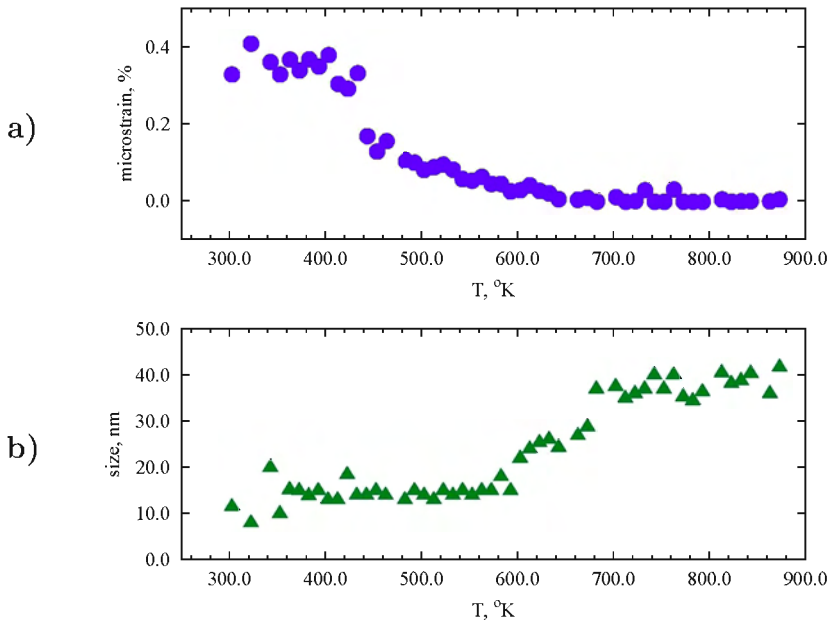

Figure 6.16: Dependence of the mean crystallite size (b) and strain (a) on the temperature for Au calculated by TOPAS v2.1.

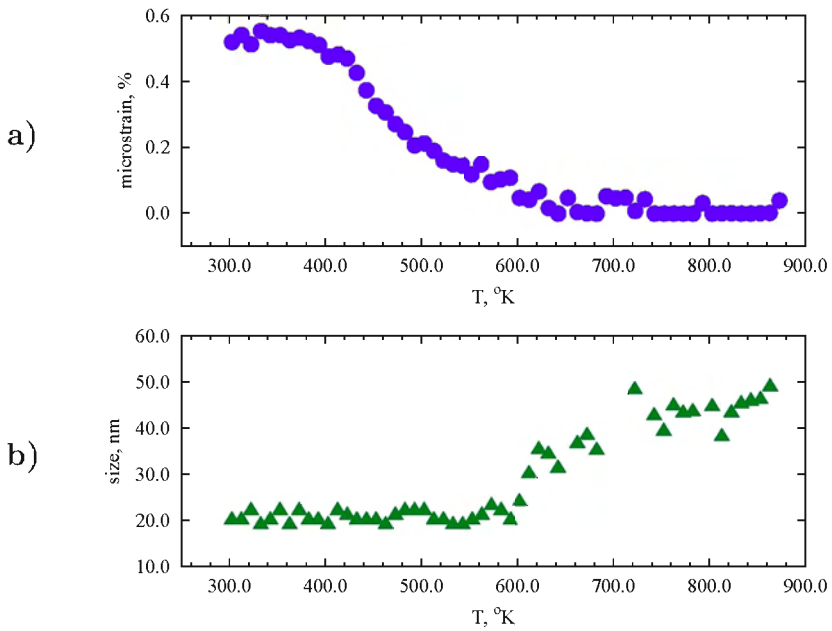

Figure 6.17: Dependence of the mean crystallite size (b) and strain (a) on the temperature for AuAg alloy calculated by TOPAS v2.1.

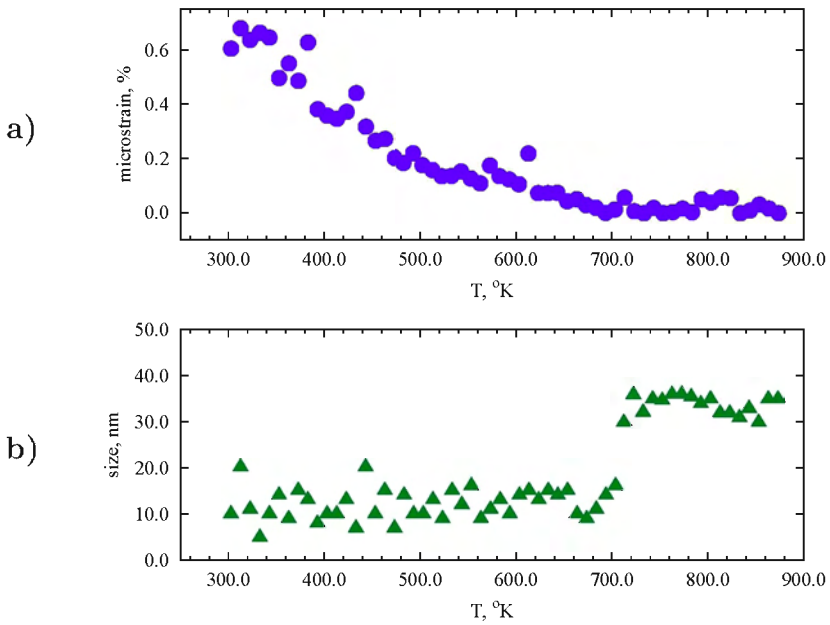

Figure 6.18: Dependence of the mean crystallite size (b) and strain (a) on the temperature for AuPd alloy calculated by TOPAS v2.1.

Chapter 7

Conclusion and outlook

The convolution model, which uses a physically reasonable size profile and a Gaussian-strain profile for the line profile fitting and accommodates the modal size, size distribution and strain parameters has been successfully developed, validated and, finally, applied to the experimental diffraction data for CeO_2 and nanostructured gold, gold-silve and gold-palladium alloys. It is shown that the convolution model gives access to the size distribution and the strain information from the diffraction data. By this method, consistent crystallite sizes are obtained and a good agreement between strain values is achieved. The 'convolution' size distribution results agree satisfactorily with those obtained from transmission electron microscopy (TEM). The TEM-derived grain sizes, however, are larger than the 'convolution' crystallite sizes indicating that the apparent grains contain clusters of crystallites.

The use of the Voigt function for size and strain analysis by fitting of diffraction data is popular because it favours the deconvolution procedures as well as the separation of size and strain effects in the analysis. This approach gives adequate information about size and strain values, however, it has three deficiencies: it uses the physically unjustified Lorentzian-size and Gaussian-strain assumptions, it does not take into account the size distribution information and it cannot deal with 'super-Lorentzian' profiles. These deficiencies are confirmed in this study by fitting simulated physically-derived size profiles with a Voigt function based model.

It has been well recognised that experimental X-ray diffraction profiles are the convolutions of various instrumental aberrations and the intrinsic diffraction patterns

of the sample. Therefore, the knowledge of the instrumental function is very important in X-ray diffraction as it influences the accuracy of the retrieved information about size and strain. The commonly used empirical model based on split Voigt or Pearson VII functions fit the instrumental function profile defined by some standard reference materials pretty well. Otherwise, due to a big number of refinable parameters and the dependence between them the data defined by different standard samples can vary considerably. Therefore, the model for instrumental function based on physical properties of the diffractometer is more preferable. Such a model is proposed in this work. It is shown that this model can fit the instrumental function very well. Hereby, the number of parameters which are necessary for a successfull description of the instrumental function dramatically decreases (from 18 in the case of split Pearson VII function (see §2.1) down to 4 parameters) which makes the fitting routine more stable and the instrumental function more reproducible from sample to sample.

The determination of the instrumental function requires, however, the development of a stable algorithm for its deconvolution. No significant improvement is achieved in methods for elimination of instrumental aberration from experimental peak profiles proposed in literature.

It has been shown that commonly used Fourier based deconvolution methods cause a dramatical increase of noise in the deconvoluted profile: this method is very sensitive to the noise in the experimental signal. Moreover, its application leads to the increase of the noise level in the deconvoluted signal. Even with relative low instrumental noise ($\sim 10\%$) this technique is absolutely not stable

Therefore, a new deconvolution technique which is fast, independent of a concrete model for the instrumental function and more reliable in terms of stability, especially in the case of large non neglectable experimental noise, is developed.

The superresolving reconstruction of signals in X-ray diffractometry shows high

stability and the overestimation of the noise level leads only to a slight worsening of the restoration results. Whereas, by using Fourier based deconvolution models, even lower noise levels completely destroy the solution. An additional advantage of the proposed regularisation technique is its independence on the concrete analytical form of the approximation of the instrumental function. Hence, the introduction of additional effects to describe the instrumental function, or completely changing the model for describing the instrumental function just change the form of the kernel $h(t, z)$, however, the algorithm for recovering of the specimen profile can further be used.

The proposed method is successfully applied to the experimental X-ray diffraction data for nanostructured CeO_2, gold and gold alloys. Estimated results for crystallite sizes and microstains are compared with those obtained from TEM analyses and from commercially available software TOPAS [BrukerAXS, 2003] and are in a good agreement with them. It has to be noted that, opposite to TOPAS, the proposed method gives not just information about mean crystallite size but also about crystallite size distribution. Moreover, the proposed method shows a high stability to the experimental noise level in the X-ray measurements and, therefore, leads to the determination of realistic results with high efficiency. This new algorithm will especially advance the evaluation of real-time experiments.

It can be concluded that proposed superresolving reconstruction of signals in X-ray diffractometry is universal. It has no limitation due to the form of the instrumental functions. It simultaneously can be applied to a whole X-ray diffraction profile and leads to the reconstruction of 'pure' specimen profiles, which can be used for the subsequent profile analysis such as Rietveld using different available contemporary software packages. In addition, the use of the proposed method increases the efficiency of the phase analysis because the shifts and overlaps of the peaks caused by different instrumental aberrations are removed from the investigated signal.

Appendix A

Investigation of structure and dynamics of binary mixtures consisting of charged colloids by means of Brownian dynamics simulation.

Structure and dynamics of binary mixtures consisting of charged colloids are investigated using Brownian dynamics simulations. For the description of the structure three partial correlation functions g_{AA}, g_{BB} and g_{AB} are calculated for different ratios of particle sizes and number of charges. The time dependent dynamic properties with non-Gaussian diffusion are investigated both in terms of self diffusion and collective diffusion. In intermediate time scale a subdiffusive process indicates memory effects resulting from the caging of neighbouring particles. For long times, again, a diffusive process is observed with the long-time self diffusion coefficient which depends on the strength of the interparticle interactions.

Simulation method

Let us consider a binary mixture of charged spherical polyballs of N_1 and N_2 particles with diameters σ_1 and $\sigma_2(> \sigma_1)$, respectively. The interaction between all the pairs (i, j) of particles separated by a center-to-center distance $r = |\vec{r}_i - \vec{r}_j|$ can be modelled via the purely repulsive size-corrected DLVO potential [Wagner et al., 2001]

$$U_{ij}(r) = \frac{Z_i Z_j e^2}{\epsilon} \left(\frac{e^{k\sigma_i}}{1 + k\sigma_i} \right) \left(\frac{e^{k\sigma_j}}{1 + k\sigma_j} \right) \frac{e^{-kr}}{r}, \tag{A.1}$$

where Z_i, Z_j are the effective numbers of charges on species i and j, respectively, and ϵ is the dielectric constant. The inclusion of the geometrical factor $\exp[k(\sigma_i+\sigma_j)]/(1+k\sigma_i)(1+k\sigma_j)$ is like incorporating the hard-core repulsion [Rosenberg and Thirumalai,

1987]. For a binary suspension, the inverse Debye-Hückel screening length κ is given by

$$k^2 = \frac{4\pi e^2}{\epsilon k_B T}\left(n_p \overline{Z} + \sum_i n_i z_i^2\right) \tag{A.2}$$

where n_p and n_i are the total number densities of the particles and the monovalent impurity ions (i.e., $z_i = 1$), respectively. Here $\overline{Z} = xZ_1 + (1-x)Z_2$, $x = N_1/(N_1+N_2)$ and k_B is the Boltzmann constant.

Following Errnak and Yeh [1974]; Errnak [1975a,b], the finite difference Brownian dynamic (BD) algorithm is used. In this algorithm the stochastic Langevin equations of motion are integrated in a finite time interval Δt to update the particle positions $\{\mathbf{r}_i(t)\}$:

$$\mathbf{r}_i(t+\Delta t) = \mathbf{r}_i(t) + \beta \sum_{j=1}^{N} (\mathbf{D}_{ij} \cdot \mathbf{f}_j(t) \cdot \Delta t) + \sum_{j=1}^{N} (\nabla_{r_j} \cdot \mathbf{D}_{ij} \cdot \Delta t) + \mathbf{R}_i + \mathcal{O}_i(t^2). \tag{A.3}$$

Here, β denotes $1/(k_B T)$, $\mathbf{D}_{ij}$ is the diffusion tensor, $N = N_1 + N_2$ and $\mathbf{f}_j(t)$ the instantaneous force on particle j arising from direct interactions from the other $N-1$ particles. The force $\mathbf{f}_j$ can be obtained by the gradient of the interaction potential U_{ij}

$$\mathbf{f}_j = -\sum_{j=1}^{N} \nabla_i U_{ij}(1 - \delta_{ij}). \tag{A.4}$$

The random displacements $\mathbf{R}_i$ are sampled from a Gaussian distribution with zero mean and variance $\langle \mathbf{R}_i \mathbf{R}_j \rangle = 2\mathbf{D}_{ij}\Delta t$.

If hydrodynamic interaction can be neglected, the diffusion tensor $\mathbf{D}_{ij}$ simplifies to $D_0 = k_B T/\xi = k_B T/(3\pi\eta\sigma_p)$, where ξ is the macroscopic friction coefficient, η is the viscosity of solvent and σ_p is the hydrodynamic diameters of the particle. The choice of Δt should provide a reasonable stability of the trajectory. The step Δt is chosen to be much smaller than the density relaxation time $\tau_d (\simeq \sigma^2/D_0 \sim 10^{-3}\,\mathrm{sec})$

but much larger than the velocity relaxation time $\tau_v = \frac{M}{\epsilon}(\sim 10^{-8}\,\mathrm{sec})$, where M is the particle mass. The value $\Delta t \simeq 10^{-6}\,\mathrm{sec}$ was found to be a satisfactory choice to ensure a reasonable stability of the trajectories.

In computer simulations commonly reduced units are used, where the physical parameters are referred to system immanent parameters like the particle diameter. In this work reduced units as in [Wagner et al., 2001] are used and are marked by an asterisks.

Observables

Upon knowledge of the trajectories of all particles and the interaction potential, in principle all physical properties of the system can be calculated. In this work we focus on the pair correlation function $g(r)$ and the mean square displacement $\langle \Delta r^2 \rangle$, which is related to the self-diffusion coefficient by the Einstein-Smoluchowsky relation $\langle \Delta r^2 \rangle = 2\alpha D_S(t)t$, where α denotes the dimensionality of the system and $D_S(t)$ the time-dependent self-diffusion coefficient [Wagner et al., 2001].

The generalized pair correlation function is given by

$$g(\mathbf{r}) = \frac{1}{\rho^2} \left\langle \sum_i \sum_{j \neq i} \delta(\mathbf{r}_i)\delta(\mathbf{r}_j - \mathbf{r}) \right\rangle \tag{A.5}$$

The static structure factor $S(\mathbf{Q})$ can be calculated as Fourier transformation of $g(\mathbf{r})$. Taking into account that liquidlike structures are isotropic, pair correlation functions and structure factors are functions only of the moduli $r = |\mathbf{r}|$ and $Q = |\mathbf{Q}|$, respectively. The static structure factor $S(Q)$ takes a form

$$S(Q) = 1 + 4\pi\rho \int r^2 g(r) \frac{\sin(Qr)}{Qr} dr. \tag{A.6}$$

The mean square displacement $\langle \Delta r^2 \rangle(t)$ is

$$\langle \Delta r^2 \rangle(t) = \langle [\mathrm{r}_l(t) - \mathrm{r}_l(0)]^2 \rangle = 6w(t), \tag{A.7}$$

and the time dependent self-diffusion coefficient $D_S(t)$ can be expressed as

$$D_S(t) = \frac{1}{6} \cdot \frac{d\left(\langle \Delta r^2 \rangle(t)\right)}{dt}. \tag{A.8}$$

Results and discussion

The bulk of simulations was carried out with $N = N_1 + N_2 = 1024$ particles confined to a cubic box (of volume V), whose dimensions are adjusted to get the appropriate number density $n_p = N/V$. The cubic periodic boundary conditions and its natural consequence the minimum image convention [Allen and Tildesley, 1987], to minimise the surface effect were used in the simulation. Up to $1 \cdot 10^6$ steps corresponding to one second in real time after equilibration of the system were performed. The simulation starting from bcc lattices is made. The system considered to be in equilibrium if the pair correlation function does not changed in subsequences runs (see Fig. A.1).

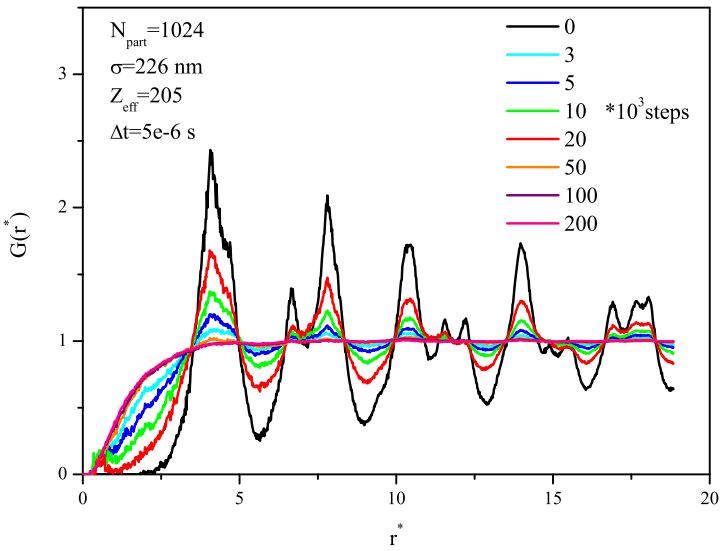

Figure A.1: The pair-correlation functions resulting from BD simulations start from bcc lattices.

The pair-correlation functions and the static structure factor resulting from BD

simulations for different concentration ratios (ρ_1/ρ_2) of species are shown in Figs. A.2 and A.3. The other parameters of the model system are $N_{particles} = 1024$, $\rho = 5 \cdot 10^{-3} m^{-3}$, $T = 298.0K$, $\Delta t = 1ms$, $\sigma_1 = 100nm$, $\sigma_2 = 200nm$, $Z_1 = 105$, $Z_2 = 405$.

In Fig. A.4 the reduced mean square displacement $w(t) = \langle \Delta r^2 \rangle (t)$ is displayed. In this figure, three regimes are visible: for short times, we see a diffusive process characterized by the linear increase of the mean square displacement; the subsequent nonlinear regime is a subdiffusive process caused by the cage-effect of the surrounding particles; for long times, we find again a linear regime indicating a diffusive process. In both diffusive regimes, the self-diffusion coefficient corresponds to the slope of $w(t)$ indicated by the dotted lines. The time-dependent relative self-diffusion coefficients are displayed in Fig. A.5 for different concentration ratios of species.

By using of simulated data it is possible to reproduce the movement of each particle in the colloidal binary mixtures. In the Fig. A.6 the screenshots of movie which shows the moving dynamics of the colloidal binary mixtures are represented.

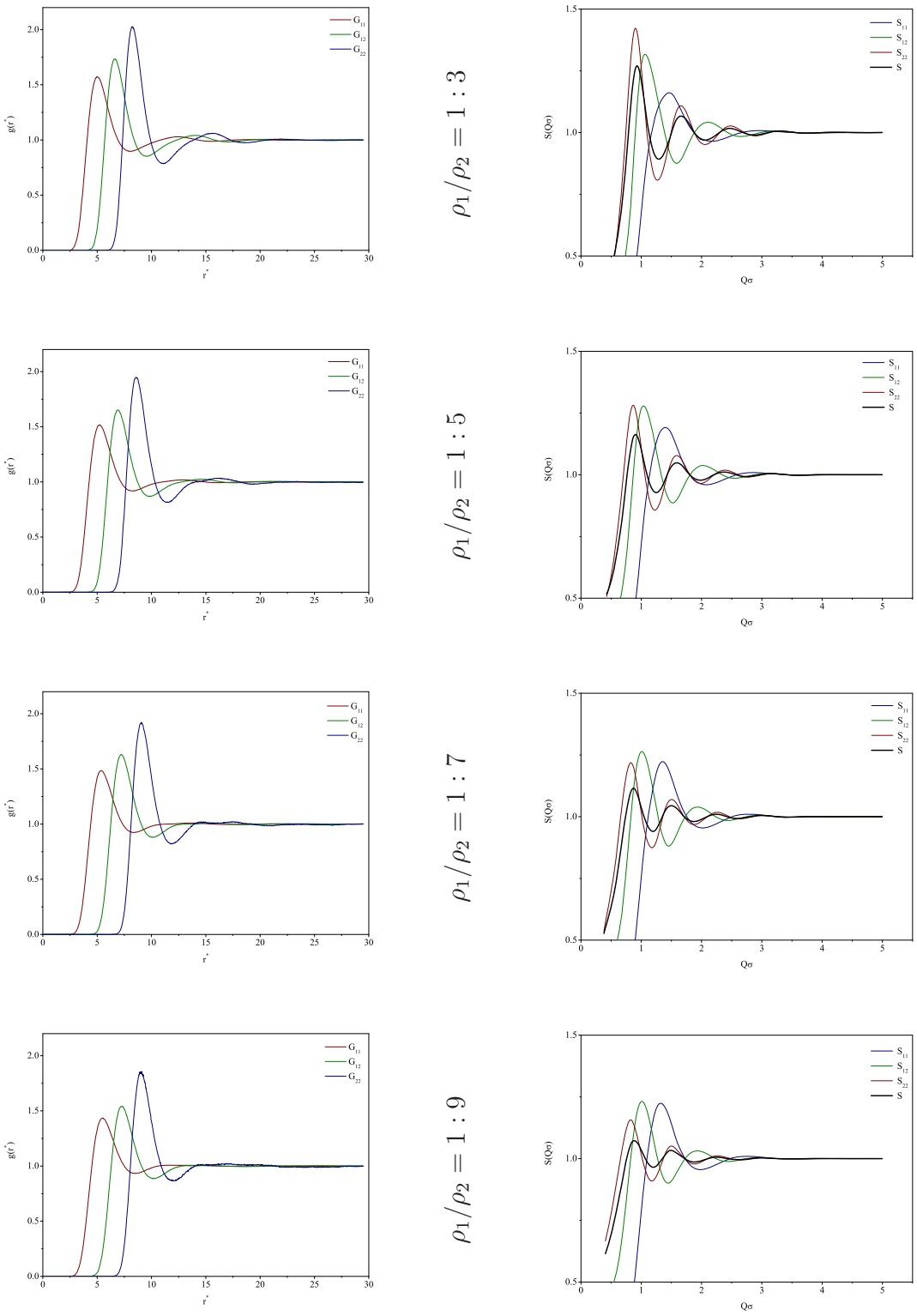

Figure A.2: The pair-correlation functions (left) and the static structure factor (right) resulting from BD simulations for different concentration ratios (ρ_1/ρ_2) of species. $N_{particles} = 1024$, $\rho = 5 \cdot 10^{-3} m^{-3}$, $T = 298.0K$, $\Delta t = 1ms$, $\sigma_1 = 100nm$, $\sigma_2 = 200nm$, $Z_1 = 105$, $Z_2 = 405$.

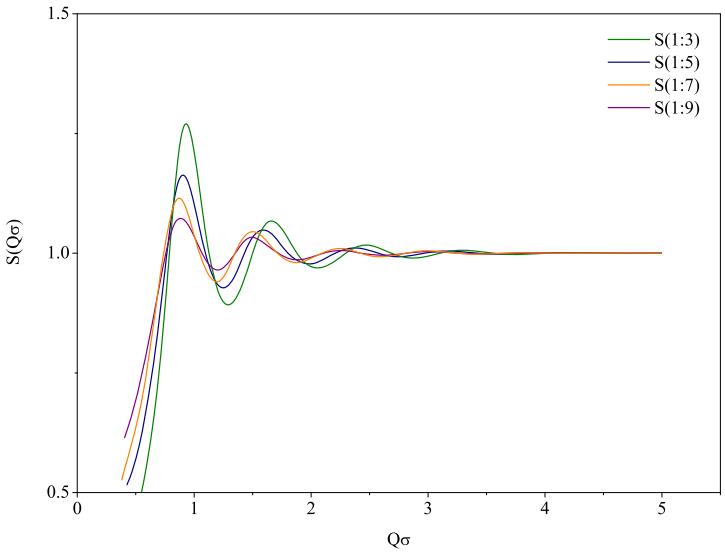

Figure A.3: The static structure factor resulting from BD simulations for different concentration ratios of species. Simulation parameters are the same as in Fig. A.2.

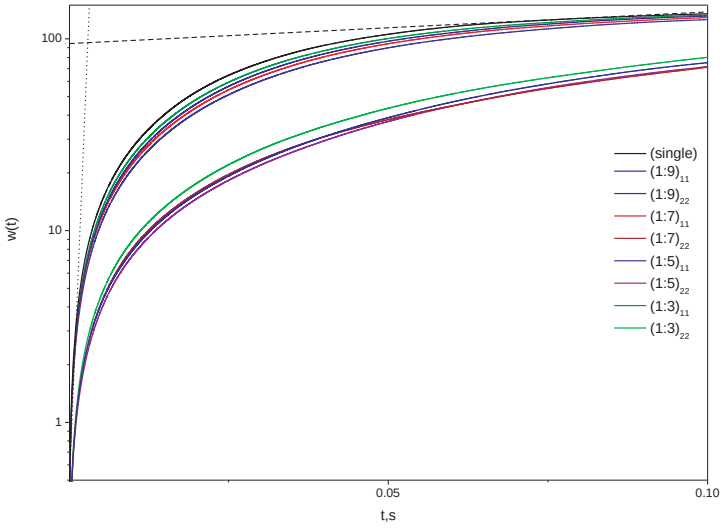

Figure A.4: The mean square displacement. The dotted and dashed lines indicate the slope equivalent to the short and long time self-diffusion coefficient, respectively.

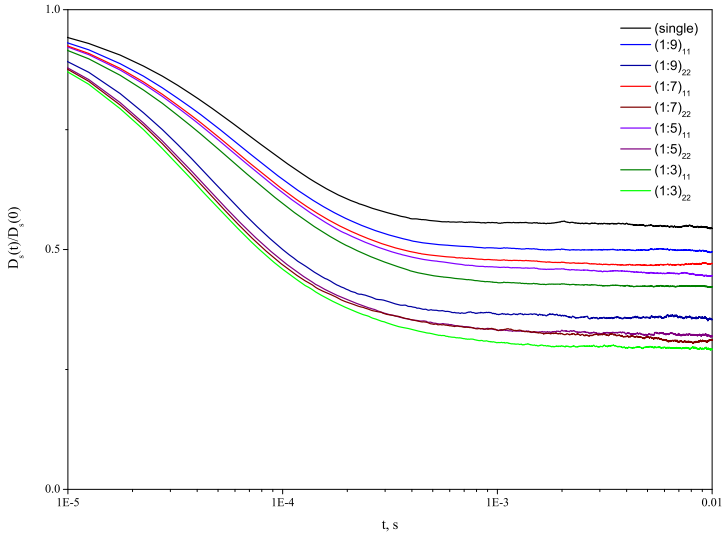

Figure A.5: The time dependence of the self-diffusion coefficient.

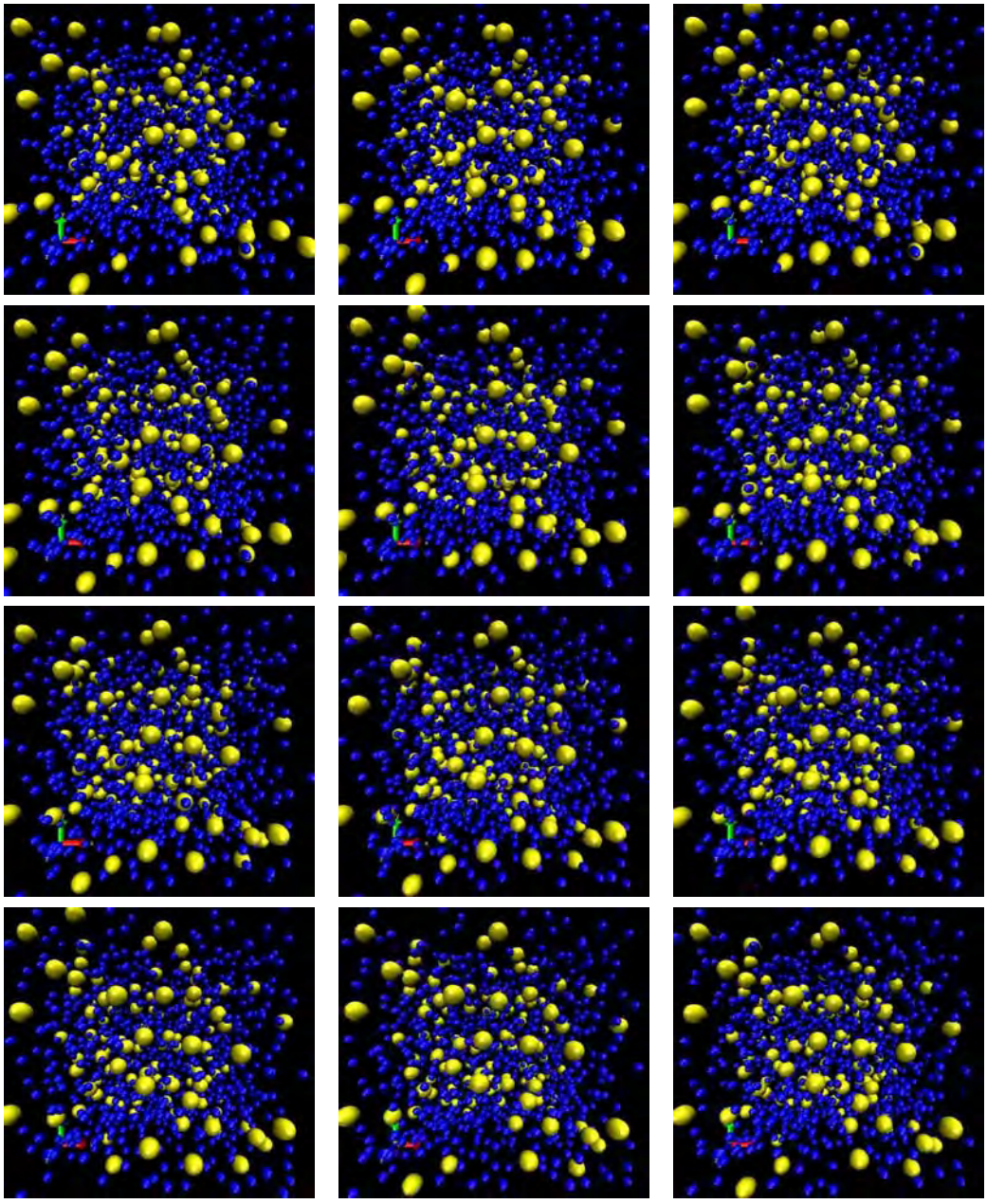

Figure A.6: The screenshots of BD simulations movie.

Appendix B

Publications and conference presentations

Conference presentations

Piskarov, V., Wagner, J., and Hempelmann, R. "Deconvolution of X-Ray Diffraction Profile by Using the Regularization Technique", XX Congress of the International Union of Crystallography, 23-31 August 2005, Florence, Italy.

Piskarov, V., Wagner, J., and Hempelmann, R. "Grain size determination for nanomaterials by XRD profile analysis", 10th European Powder Diffraction Conference (EPDIC), 1-4 September 2006, Geneva, Switzerland.

Piskarov, V., Wagner, J., and Hempelmann, R., "Investigation of structure and dynamics of binary mixtures consisting of charged colloids by means of Brownian dynamics simulation", Hauptversammlung 2006 der Deutschen Bunsengesellschaft, 25-27 May 2006, Erlangen, Germany.

Publications

Piskarov, V., Wagner, J., and Hempelmann, R. "Deconvolution of X-Ray Diffraction Profile by Using the Regularization Technique" Acta Cryst. A61, (2005), C163.

Piskarov, V., Wagner, J., and Hempelmann, R. "Grain size determination for nanomaterials by XRD profile analysis" - to be published.

Yevtushenko, O., Piskarov, V., Natter, H., Hempelmann, R. "Electrochemical nucleation and growth kinetics of nanostructured gold" - to be published.

Piskarov, V., Yevtushenko, O., Hempelmann, R. "Investigation of crystallite size distribution in nanostructured materials by means of high temperature X-ray diffraction" - to be published.

Appendix C

Acknowledgements

First of all, I would like to express my sincere thanks to Prof. Dr. Rolf Hempelmann for giving me the opportunity to do my PhD thesis within his group. This gave me the possibility of entering the exciting scientific fields. Due to his continuous support, his kind, helpful advice and to the interesting discussions, I was able to stay focused and not stray away from the essence of my work. His commitment and encouragement allowed me to present our work at national and international conferences,where I became acquainted with the latest research and met many prestigious scientists.
I sincerely want to thank PD Dr. Joachim Wagner for having always an open ear to discussion, for his contagious curiosity and his constant practical advice in the last three years of my studies.
Especial thanks to Dr. Harald Natter for providing the information about X-ray devices and interesting and fruitful discussions.
I thank Sylvia Kuhn for fast high-quality TEM measurements.
I thank Andreas Tschöpe for nice CeO_2 samples.
I also thank Trieu Vinh for translation of some parts of my thesis in German language.
All my coworkers I thank for friendly atmosphere.
I sincerely acknowledge Dr. Lothar Heinrich for his support and friendly advices.
I also thank Prof. Dr. Kurashov Vitaliy Naumovych for long time collaboration and introduction into Ill-posed problems.
Many thanks to my patient and loving wife, who has been a great source of strength all through this work and without her support this thesis would never have started much less finished.
To everybody else who accompanied me in this PhD journey:

THANK YOU!

Bibliography

Agarwal, B. K. [1979], *X-Ray Spectroscopy*. SpringerVerlag, Berlin, Heidelberg, New York.

Alexander, L. [1954], *J. Appl. Phys.*, 25(2), 155–161.

Allen, M. P. and Tildesley, D. J. [1987], *Computer Simulation of Liquids*. Oxford University Press, London.

Audebrand, N., Magnenet, C., Auffredic, J. P. and Louer, D. [2000a], *Mater. Sci. Forum*, 321(2), 1034 – 1039.

Audebrand, N., Magnenet, C., Auffredic, J. P. and Louer, D. [2000b], *Chem. Mat.*, 12, 1791 – 1799.

Auffredic, J., Boultif, A., Langford, J. I. and Louer, D. [1995], *J. Am. Ceram. Soc.*, 78(2), 323 – 328.

Balasingh, C., Abuhasan, A. and Predecki, P. K. [1991], *Powd. Diff.*, 6(1), 16 – 19.

Balzar, D. [1992], *J. Appl. Cryst.*, 25, 559 – 570.

Balzar, D. *Voigt function model in diffraction-line broadening analysis*, pages 94 – 126. IUCr/Oxford University Press, Oxford, [1999].

Balzar, D. and Ledbetter, H. [1995], *Adv. X-ray Analysis*, 38, 397 – 404.

Balzar, D. and Popa, N. C. [2005], *The Rigaku Journal*, 22(1), 16 – 25.

Bearden, J. A. [1967], *Rev. Mod. Phys.*, 39, 78.

Bergmann, J., Friedel, P. and Kleeberg, R. [1998], *CPD Newsl.*, 20, 5 – 8.

Berkum, J. G. M. V., Sprong, G. J. M., de Keijser, T. H. and Delhez, R. [1995], *Powd. Diff.*, 10(2), 129 – 139.

Berkum, J. G. M. V., Delhez, R., de Keijser, T. H. and Mittemeijer, E. J. *Defect and Microstructure Analysis by Diffraction*, chapter Diffraction-line broadening analysis of strain fields in crystalline solids, pages 214 – 233. IUCr/Oxford University Press, Oxford, [1999].

Beyts, R. and Mak-Donnell, M. [1989], *Vosstanovlenie i rekonstrukciya izobrajeniy (in Russian)*. M.: Mir.

Bremer, J. and Serum, H. [1979], *Phys. Lett.*, A75, 47.

Bremer, J., Johnsen, T. and Serum, H. [1982], *X-Ray Spectrom.*, 11, 149.

BrukerAXS. *TOPAS V2.1: General profile and structure analysis software for powder diffraction data.* Bruker AXS, Karlsruhe, Germany, [2003].

Cheary, R. W. and Coelho, A. [1992], *J. Appl. Cryst.*, 25, 109–121.

Cheary, R. W. and Coelho, A. [1998], *J. Appl. Cryst.*, 31, 851 – 861.

Cheary, R. W., Coelho, A. A. and Cline, J. P. [2004], *Journal of Research of the National Institute of Standards and Technology*, 109(1), 1–25.

Chen, P.-L. and Chen, I.-W. [1993], *J. Am. Ceram. Soc.*, 76(6), 1577 – 1583.

Cullity, B. D. [1978], *Elements of x-ray diffraction.* Addison-Wesley Pub. Co.

David, W. I. F. [1986], *J. Appl. Cryst.*, 19, 63 – 64.

de Keijser, T. H., Langford, J. I., Mittemeijer, E. J. and Vogels, A. B. P. [1982], *J. Appl. Cryst.*, 15, 308 – 314.

de Keijser, T. H., Mittemeijer, E. J. and Rozendaal, H. C. F. [1983], *J. Appl. Cryst.*, 16, 309 – 316.

Delhez, R. and de Keijser E. J. Mittemeijer, T. H. *Accuracy of crystallite size and strain values from x-ray diffraction line profiles using Fourier series*, pages 213 – 253. National Bureau of Standards, Washington D.C., [1980].

Delhez, R., de Keijser, T. and Mittemeijer, E. J. [1982], *Fres. Z. Anal. Chem.*, 312, 1 – 16.

Delhez, R., Keijser, T. H. D., Langford, J. I., Louer, D., Mittemeijer, E. J. and Sonneveld, E. J. *Crystal imperfection broadening and peak shape in the Rietveld method*, pages 132 – 166. IUCr/Oxford University Press, [1993].

Enzo, D. and Schiffini, L. *Profile fitting and analytical functions*, pages 29 – 40. IUCr/Oxford University Press, Oxford, [1999].

Enzo, S., Fagherazzi, G., Benedetti, A. and Polizzi, S. [1988], *J. Appl. Cryst.*, 21(5), 536–542.

Ergun, S. [1968], *J. Appl. Cryst.*, 1, 19 – 23.

Errnak, D. L. [1975a], *J. Chem. Phys.*, 62(1975), 4189.

Errnak, D. L. [1975b], *J. Chem. Phys.*, 62(1975), 4197.

Errnak, D. L. and Yeh, Y. [1974], *Chem. Phys. Lett.*, 24, 243.

Finger, L. W., Cox, D. E. and Jephcoat, A. P. [1994], *J. Appl. Cryst.*, 27, 892.

Finster, J., Leonhardt, G. and Meisel, A. [1971], *J. Phys. (Paris)*, C4(32), 218.

Freiman, S. W. and Trahey, N. M. [2000], *Standard Reference Material 660a. Lanthanum Hexaboride Powder - Line Position and Line Shape Standard for Powder Diffraction.* NIST, Gaithersburg, MD. USA.

Greaves, C. [1985], *J. Appl. Cryst.*, 18, 48 – 50.

Groma, I., Ungar, T. and Wilkens, M. [1988], *J. Appl Cryst.*, 21, 47.

Guillou, N., Auffredic, J. P. and Louer, D. [1995], *Powd. Diff.*, 10(4), 236 – 240.

Guinier, A. [1963], *X-ray diffraction in crystals, imperfect crystals and amorphous bodies.* San Francisco.

Hall, M. M., Veeraraghavan, V. G., Rubin, H. and Winchell, P. G. [1977], *J. Appl. Cryst.*, 10, 66 – 68.

Hansen, P. C. [1994], *Num. Alg.*, 6, 1 – 35.

Honkimaki, V. [1996], *J. Appl. Cryst*, 29, 617 – 624.

Howard, S. A. and Snyder, R. L. [1989], *J. Appl. Cryst.*, 22, 238 – 243.

Huang, T. C. and Parrish, W. [1975], *App. Phys. Lett.*, 27(3), 123 – 124.

Ida, T. [1998a], *Rev. Sci. Instrum.*, 69(6), 2268–2272.

Ida, T. [1998b], *Rev. Sci. Instrum.*, 69(11), 3837–3839.

Ida, T. and Kimura, K. [1999a], *J. Appl. Cryst.*, 32, 634–640.

Ida, T. and Kimura, K. [1999b], *J. Appl. Cryst.*, 32, 982–991.

Ida, T. and Toraya, H. [2002], *J. Appl. Cryst.*, 35, 58–68.

Ida, T., Shimazaki, S., Hibino, H. and Toraya, H. [2003], *J. Appl. Cryst.*, 36, 1107–1115.

James, R. W. [1965], *The optical principles of the diffraction of x-rays.*

Klug, H. P. and Alexander, L. E. [1974], *X-ray diffraction procedures: for polycrystalline and amorphous materials.* Wiley, New York, 2 edition.

Kogan, V. A. and Kupriyanov, M. F. [1992], *J. Appl. Cryst.*, 25(16–25).

Kojdecki, M. A. [2004], *Mater. Sci. Forum*, 443–444, 107 – 110.

Krivoglaz, M. A. [1996], *X-ray and neutron diffraction in nonideal crystals*. Springer, Berlin.

Ladell, J., Parrish, W. and Taylor, J. [1959], *Acta Crystallogr.*, 12, 561.

Langford, J. I. [1978], *J. Appl. Cryst.*, 11, 10 – 14.

Langford, J. I. *The use of the Voigt function in determining microstructural properties from diffraction data by means of pattern decomposition*, pages 110 – 126. [1992].

Langford, J. I. *Defect and Microstructure Analysis by Diffraction*, chapter Use of pattern decomposition or simulation to study microstructure: theoretical consideration, pages 59 – 81. IUCr/Oxford University Press, Oxford, [1999].

Langford, J. I. and Louer, D. [1982], *J. Appl Cryst.*, 15, 20 – 26.

Langford, J. I. and Wilson, A. J. C. [1978], *J. Appl. Cryst.*, 11, 102 – 113.

Langford, J. I., Louer, D., Sonneveld, E. and Visser, J. [1986], *Powd. Diff.*, 1(3), 211 – 221.

Langford, J. I., Delhez, R., de Keijser, T. H. and Mittemeijer, E. J. [1988], *Aus. J. Phys.*, 41, 173 – 187.

Langford, J. I., Louer, D. and Scardi, P. [2000], *J. Appl. Cryst.*, 33, 964 – 974.

Larson, A. C. and von Dreele, R. B. [1987], *Los Alamos National Laboratory Report No. LA-UR-86-748*. Los Alamos National Laboratory, USA.

Leoni, M., Scardi, P. and Langford, J. I. [1998], *Powd. Diff.*, 13(4), 210 – 215.

Levin, B. R. [1989], *Teoreticheskie osnovy statisticheskoy radiotehniki (in Russian)*. M.: Radio i svyaz'.

Louer, D. *Use of pattern decomposition to study microstructure: practical aspects and applications*, pages 673 – 697. IUCr/Oxford University Press, Oxford, [1999].

Louer, D. and Langford, J. I. [1988], *J. Appl Cryst.*, 21, 430 – 437.

Louer, D., Bataille, T., Roisnel, T. and Rodriguez-Carvajal, J. [2002], *Powd. Diff.*, 17(4), 262 – 269.

Masson, O., Dooryhee, E. and Fitch, A. [2003], *J. Appl. Cryst*, 36, 286 – 294.

Nakamura, Y., Oguro, K., Uehara, I. and Akiba, E. [2000], *J. Alloys Compd.*, 298, 138 – 145.

Natter, H., Schmelzer, M. and Hempelmann, R. [1997], *Materials Res.*, 13(5), 1186.

Natter, H., Schmelzer, M., Loeffler, M.-S., Krill, C. E., Fitch, A. and Hempelmann, R. [2000], *Journal of Physical Chemistry*, 104, 2467.

Noyan, I. C. and Cohen, J. B. [1987], *Residual stress: measurement by diffraction and interpretation*. Springer-Verlag, New York.

Parratt, L. G. [1959], *Rev. Mod. Phys.*, 31, 616.

Piskarev, V. L., Kurashov, V. N. and Kurashov, A. V. [1997], *Proc. SPIE*, 3317, 36.

Plevert, J. and Louer, D. [1990], *J. Chim. Phys.*, 87, 1427 – 1440.

Popa, N. C. and Balzar, D. [2002], *J. Appl. Cryst.*, 35, 338 – 346.

Pratapa, S., O'Connor, B. H. and Hunter, B. [2002], *J. Appl. Cryst.*, 35, 155 – 162.

Press, W. H., Flannery, P, B., Teukolsky, A, S., Vetterling and T, W. [1986], *Numerical Recipes*. Cambridge University Press.

Rachinger, W. A. [1948], *J. Sci. Instrum.*, 26, 254 – 255.

Reefman, D. [1999], *Defect and Microstructure Analysis by Diffraction*. IUCr/Oxford University Press, Oxford.

Rietveld, H. M. [1967], *Acta Cryst.*, 22, 151 – 152.

Rietveld, H. M. [1969], *J. Appl. Cryst.*, 2, 65 – 71.

Rosenberg, R. O. and Thirumalai, D. [1987], *Phys. Rev.*, A 36(1987), 5690.

Sauder, W. C., Huddle, J. R., Wilson, J. D. and Lavilla, R. E. [1977], *Phys. Lett.*, A63, 313.

Scardi, P. *A new whole-powder pattern-fitting approach*, pages 570 – 596. IUCr/Oxford University Press, Oxford, [1999].

Scardi, P. and Leoni, M. [2001], *Acta Cryst.*, A58, 190 – 200.

Somashekar, R. and Somashekarappa, H. [1997], *J. Appl. Cryst.*, 30, 147 – 152.

Stephens, P. W. [1999], *J. Appl. Cryst.*, 32, 281 – 289.

Stokes, A. R. [1948], *Proceedings of the Physical Society (London)*, A61, 382 – 392.

Stokes, A. R. and Wilson, A. J. C. [1944], *Proc. Phys. Soc.*, 56, 174 – 181.

Thompson, P., Cox, D. E. and Hastings, J. B. [1987], *J. Appl. Cryst.*, 20, 79 – 83.

Timmers, J., Delhez, R., Tuinstra, F. and Peerdeman, F. *Accuracy in Powder Diffraction II*, volume 27, chapter X-ray tracing, a tool for improved Accuracy in Powder Diffraction, page 217. NIST Special Publication 846, [1992].

Toraya, H. [1986], *J. Appl. Cryst.*, 19, 440 – 447.

Tsutsumi, K. and Nakamori, H. [1973], *Proceedings of the International Symposium, X-Ray Spectra and Electronic Structure of Matter, edited by A. Faessler and G. Wiech*, 1, 100.

Ungar, T. *Defect and Microstructure Analysis by Diffraction*, chapter The dislocation-based model of strain broadening in x-ray line profile analysis, pages 165 – 199. IUCr/Oxford University Press, Oxford, [1999].

Ungar, T., Gubicza, J., Ribarik, G. and Borbely, A. [2001], *J. Appl. Cryst.*, 34, 298 – 310.

Vargas, R., Louer, D. and Langford, J. I. [1983], *J. Appl. Cryst.*, 16, 512 – 518.

Wagner, J., Hartl, W. and Walderhaug, H. [2001], *J. Chem. Phys.*, 114(2), 975 – 983.

Warren, B. E. and Averbach, B. L. [1950], *J. Appl. Phys.*, 21, 595 – 599.

Warren, B. E. and Averbach, B. L. [1952], *J. Appl. Phys.*, 23, 497.

Warren, B. [1969], *X-ray Diffraction*. Addison-Wesley.

Wertheim, G. K., Butler, M. A., West, K. W. and Buchanan, D. N. E. [1974], *Rev. Sci. Instrum.*, 45(11), 1369 – 1371.

Williamson, G. K. and Hall, W. H. [1953], *Acta Metal.*, 1, 22 – 31.

Wilson, A. J. C. [1962], *X-ray optics*. London, 2 edition.

Wilson, A. J. C. [1963], *Mathematical theory of x-ray powder diffractometry*. Philips Technical Library, Eindhoven.

Wilson, A. J. C. [1970], *Elements of x-ray crystallography*. Addison-Wesley, Reading, MA.

Wu, E., Gray, E. M. A. and Kisi, E. H. [1998a], *J Appl. Cryst.*, 31, 356 – 362.

Wu, E., Kisi, E. H. and Gray, E. M. A. [1998b], *J. Appl. Cryst.*, 31, 363 – 368.

Yevtushenko, O. PhD thesis, Saarbruecken, [2007].

Yevtushenko, O., Natter, H. and Hempelmann, R. [2007], *J. of Solid State Electrochem.*, 11, 138 – 143.

York, B. B. [1999], *Adv. X-Ray Anal.*, 41, 544 – 555.